Applied Catalysis B: Environmental 140–141 (2013) 559–587

Contents lists available at SciVerse ScienceDirect

Applied Catalysis B: Environmental

journal homepage: www.elsevier.com/locate/apcatb

Review

A review on non metal ion doped titania for the photocatalytic degradation of organic pollutants under UV/solar light: Role of photogenerated charge carrier dynamics in enhancing the activity

L. Gomathi Devi*, R. Kavitha

Department of Post Graduate Studies in Chemistry, Central College City Campus, Dr. Ambedkar Street, Bangalore University, Bangalore 560001, India

ARTICLE INFO

Article history:
Received 1 January 2013
Received in revised form 13 April 2013
Accepted 15 April 2013
Available online 25 April 2013

Keywords:
Titania
Non metal doping
Noble metal deposition
Codoping
Sensitization
Coupling with semiconductors
Reactive oxygen species
Interfacial charge transfer dynamics

ABSTRACT

The multifunctional and advanced semiconductor titania with superior physicochemical and opto-electronic properties is extensively investigated in wastewater purification mainly due to its non-toxicity, favorable band edge positions, water insolubility, multifaceted electronic properties, surface acid–base properties, super hydrophilicity and so on. However, large band gap and massive photogenerated charge carrier recombination hinders its wide application under natural solar light. Thus, altering the surface-bulk structure of titania is a major goal in the area of both materials and environmental chemistry for its better applications. The substitution of p block elements (B, C, N, F, S, P, and I) either at Ti^{4+} and O^{2-} sites is a promising approach to overcome the aforementioned drawbacks. This review focuses on the photocatalytic activity of non metal doped titania for a wide variety of pollutants degradation under UV/visible light, with special emphasis on nitrogen doped TiO_2. Further improvement in photoactivity of N–TiO_2 is achieved via depositing with noble metals, co-doping with foreign ions, sensitization, surface modifications and heterostructuring with other semiconductors. The mechanism governing the photocatalytic reactions is discussed in the light of charge carrier generation–separation–transfer–recombination dynamics together with pollutant adsorption and their reactions with reactive oxygenated species in liquid or gaseous regime. We are positive that this review article will further stimulate our research interest on this intriguing hot topic.

Contents

* Corresponding author. Tel.: +91 9845222867/08022961336.
E-mail address: gomatidevi_naik@yahoo.co.in (L.G. Devi).

0926-3373/$ – see front matter © 2013 Elsevier B.V. All rights reserved.
http://dx.doi.org/10.1016/j.apcatb.2013.04.035

1. Introduction

Semiconductors act as photocatalyst for the light induced photochemical reactions due to their unique electronic band structure comprising filled valence band (VB) and empty conduction band (CB). The excitation of semiconductor with photon energy $\geq E_g$ generates an electron in CB and holes in VB. The excited charge carriers (electrons and holes) are highly reactive radicals with robust reducing and oxidizing capacity respectively that may recombine or get trapped in metastable surface states, or reacts with suitable electron acceptors/donors preadsorbed on the catalyst surface. An armory of semiconductors like TiO_2, ZnO, Bi_2WO_6, $Bi_{20}Ti_{20}$, Fe_2O_3, Nb_2O_5, $BiTiO_3$, $SrTiO_3$, $ZnWO_4$, CuS/ZnS, WO_3, Ag_2CO_3, ZnS, α-sulfur crystals is used in pollutants degradation both in liquid and gaseous regime [1–15]. Since the landmark report on water splitting on TiO_2 electrodes by Fujishima and Honda [16], significant progress has been achieved in titania based photocatalysis because of its multifunctional properties like photochemical stability, highest light conversion efficiency, favorable band edge positions, cheap availability, low cost, non toxicity, bio compatabilty, their acid base–redox properties, suitable flat band potential and facile preparations with diverse morphologies [17–46]. Heterogeneous photocatalysis with TiO_2 is potentially advantageous as it proceeds at ambient conditions resulting in complete mineralization of organic pollutants to harmless products like CO_2, H_2O and mineral acids.

The band gap excitation of titania involves excitation, bulk diffusion and surface transfer of photoinduced charge carriers, where the carriers life time is vital in determining the photoactivity. The surface properties of TiO_2 intrinsically determines the surface separation and transfer of charge carriers by generating surface states where electrons and holes are spatially trapped and transferred for subsequent redox reactions [23]. The most fatal drawbacks of titania stems from its wide band gap which requires expensive UV light for activation thereby limiting its catalytic efficiency under visible portion of solar spectrum. In addition, undesired electron–hole recombination which dominates in the absence of electron acceptor or donor represents the major loss of energy results in very low quantum yield for any photocatalytic reactions. Thus, development of new approaches to modulate the electronic band gap structure of TiO_2 for visible light response with robust interfacial charge carrier transfer process would be of great interest from the stand point of its practical and widespread use. In order to utilize wide spectrum of incident photon energies, many strategies are developed to tailor the band gap absorption to visible region like metal/non metal ion doping [47–51], codoping with foreign ions [52–56], noble metal deposition [57–61] and sensitization by inorganic complexes or organic dyes [62–66], reduced TiOx [67], surface complexation [68,69] and self doping [70,71]. Among these several methods, incorporation of main group elements into titania matrix has drawn significant attention because of its ability to modify the surface-electronic properties that favors efficient photocatalysis [72]. Since TiO_2 alone does not absorb visible light, non metal incorporation helps to extend visible region absorption. To study the photodegradation reaction under visible light a word of caution is to avoid choosing textile dyes as model pollutants since many of these dye molecules can act as photosensitizers. Vinodgopal et al. explored the possibility of photosensitization through diffuse reflectance laser flash photolysis and confirmed charge injection from excited dye molecule into TiO_2 CB. Their research work reflects that photosensitization process occurs when certain dye molecules are chosen as model compounds, but however photosensitization is a minor reaction pathway. Complete mineralization of the dye molecule is never reported by photosensitization process [62c]. Yan et al. estimated the extent of photosensitization by the action spectrum analysis and suggested that the choice of dye molecule as a model compound is not appropriate. They strongly suggested the use of transparent substrates in the region of working wavelengths and showed that sulphur doped TiO_2 (S–TiO_2) is photoactive in visible region for acetic acid decomposition rather than Methylene Blue (MB) degradation [62b]. However, there are several requirements for photosensitization process to work effectively. First, the excited state of dye molecule needs to lie above the bottom of TiO_2 CB. Second, strong binding of the dye onto TiO_2 surface is desired for fast and efficient injection. Third, back electron transfer to dye cation following injection should be minimal. Fourth, dye molecule must have strong absorption in visible region of spectrum for solar energy conversion. The rates of electron injection and subsequent recombination or back electron transfer in dye sensitization are expected to depend on the nature of dye molecule and surface characteristics of the semiconductor particles [62d].

This review encompasses several advancements and exciting results of non metal doped titania, in particular nitrogen doping for the degradation of wide spectrum of organic pollutants. The mechanisms of charge carrier separation and high activity compared to undoped titania are explained by considering intrinsic and induced defects of catalyst as well as reaction of free radicals with pollutants.

2. Controversial reports on metal ion doped titania

Since the redox energy states of many transition metal ions lie within the band gap states of TiO_2, substitution of metal ions introduces an intraband state close to CB or VB edge, inducing visible light absorption at sub-band gap energies. The red shift in band gap absorption is attributed to charge transfer transition between the d electrons of dopant and CB (or VB) of TiO_2. In addition, metal ions alter the charge carrier equilibrium concentration by serving as electron–hole trap and enhance the degradation rate [73–85]. Although notable improvement in photocatalytic activity of metal ion doped TiO_2 is achieved, few research groups discussed on its detrimental effects. For instance, doping with Fe^{3+}, Mo^{5+}, Ru^{3+}, Os^{3+}, Re^{5+}, V^{4+} and Rh^{3+} in the concentration range of 0.1–0.5 atom% increased the rate of $CHCl_3$ oxidation and CCl_4 reduction, while Co^{3+} and Al^{3+} doping suppressed the reactivity [86]. Fe^{3+}–TiO_2 showed superior activity due to its unique half filled electronic configuration which serves as shallow traps, while dopants with closed shell electronic configuration (Li^+, Mg^{2+}, $A1^{3+}$, Zn^{2+}, Ga^{3+}, Zn^{2+}, Nb^{5+}, Sn^{4+}, Sb^{5+} and Ta^{5+}) had very little influence on photoactivity. Mn^{3+} which can trap both electron and hole showed poor photo reactivity which was attributed to the low driving force for electron detrapping from Mn^{2+} because of small energy difference between Mn^{2+} and Mn^{3+}. Based on these results, it was concluded that activity of metal ion doped TiO_2 appears to be complex function of dopant concentration, energy level of dopant within the lattice, their d electron configuration, distribution of dopants, electron donor density and incident light intensity [86]. Nagaveni et al. reported that detrimental effect of doping metal ions (W, V, Ce, Zr, Fe and Cu) into TiO_2 via solution combustion method for the degradation of 4-nitro phenol (4-NP) under UV/visible light irradiation and was supported by photoluminescence (PL) spectral studies [87]. The metal ion dopant can serve as trap states for electron and hole depending on its position below the CB edge or above the VB respectively (Fig. 1). The electron trapping occurs at a much faster process ($\tau = 30$ ps) compared to hole trapping ($\tau = 250$ ns):

$$TiO_2 + h\nu \rightarrow {h_{VB}}^+ + e^-_{CB}\tau = 10^{-15}\ \text{s} \quad (1)$$

$$e^-_{tr} + h^+_{tr} \rightarrow \text{heat}\tau = 10^{-9}\ \text{s} \quad (2)$$

$$e^-_{CB} \rightarrow e^-_{tr}(M^{n+} \quad \text{or} \quad O_2)\tau = 30\ \text{ps} \quad (3)$$

$$h^+_{VB} \rightarrow h^+_{tr}(OH^- \quad \text{or} \quad M^{n+1})\tau = 250\ \text{ns} \quad (4)$$

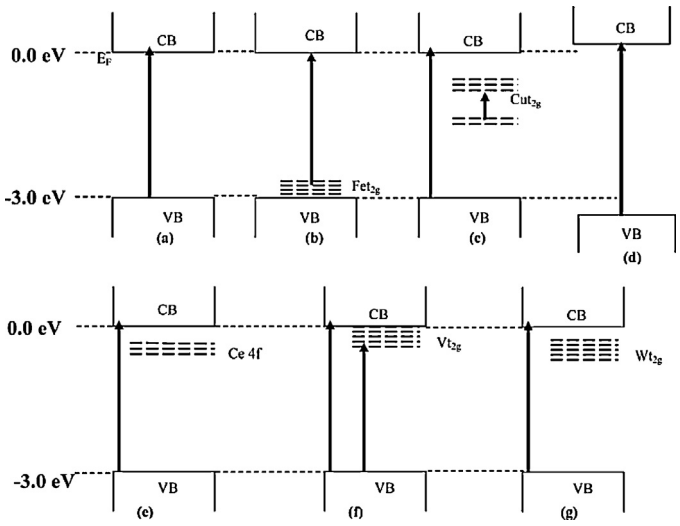

Fig. 1. Schematic representation of energy levels of metal ion dopant in TiO_2: (a) TiO_2; (b) Fe/TiO_2; (c) Cu/TiO_2; (d) Zr/TiO_2; (e) Ce/TiO_2; (f) V/TiO_2; and (g) W/TiO_2. Reprinted with permission from Ref. [87]. Copyright (2004) American Chemical Society.

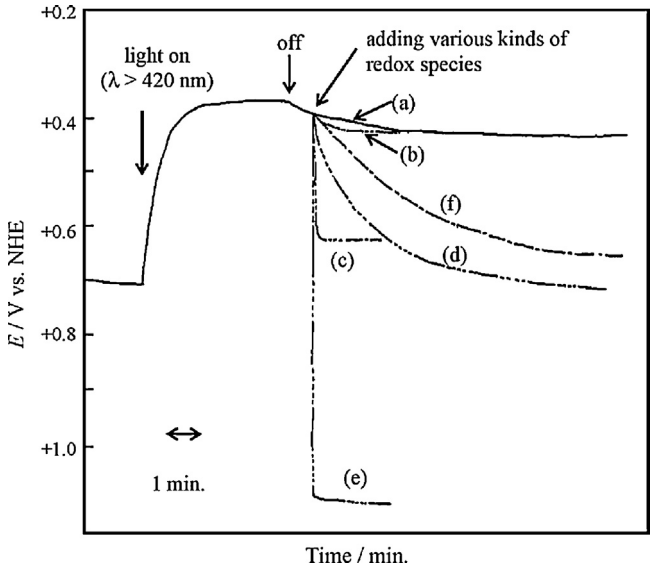

Fig. 2. Potential change on TiO_2 under photo-irradiation through (a) for N–TiO_2 through UV-35; (b) UV-35; (c) L-39; (d) Y-45 and their corresponding discharge processes. The measurements were performed in 0.25 M Na_2SO_4 involving 0.25 M acetic acid (pH 2.5).
Reprinted with the permission from Ref. [92]. Copyright (2009) Elsevier.

The metal ion dopants provide more trap sites for electrons and holes in addition to surface trap sites (adsorbed O_2 and $-OH^-$). Trapping either an electron or a hole alone is always ineffective for charge carrier separation because immobilized charge species rapidly recombines with its mobile counterparts [86]:

$$e^-_{tr} + h^+_{VB} \rightarrow TiO_2\,\tau = 30\,ns \quad (5)$$

$$e^-_{tr} + h^+_{tr} \rightarrow TiO_2\ slow \quad (6)$$

In another study, anatase TiO_2 was doped with several transition metal ions like V^{5+}, Mn^{2+}, Fe^{3+}, Ru^{3+}, Os^{3+}, Ni^{2+} and Zn^{2+} having vacant, half, partially and completely filled d orbital [88]. Mn^{2+}–TiO_2 showed enhanced activity for the degradation of indigo carmine (IC) and 4-nitro phenol (NP) under UV/solar light due to the synergistic effects of mixed anatase–rutile phase, optimum rutile content with high intimate contact between the phases, favorable surface structure with high lattice and surface energy and induced oxygen vacancies acting as reactive electron trapping site. The lowest activity of Ni^{2+}–TiO_2 was due to deleterious bulk recombination of charge carriers due to the dopant level acting as recombination centers and the induced localized states may not be optimal to facilitate photooxidation reactions. Another plausible reason was that the Ni^{2+} with partially filled electronic configuration might result in deep trap of charge carriers rather than shallow traps [88]. The sol–gel preparation of metal ion doped titania with an array of dopants like Ag^+, Rb^+, Ni^{2+}, Co^{2+}, Cu^{2+}, V^{3+}, Ru^{3+}, Fe^{3+}, Os^{3+}, Y^{3+}, La^{3+}, Pt^{4+}, Pt^{2+} and Cr^{3+} was positive to favor MB degradation, phenol and iodide oxidation under UV/visible light. In particular, Pt and Cr doped TiO_2 with high percentages of rutile showed enhanced reactivity irrespective of model reactions. Although, few dopants shifted the band gap absorption to visible range, but failed to induce redox reactions under visible light illumination [89]. Despite the extensive research, direct comparison and unifying conclusions are difficult to make correlation between photophysical measurements and photochemical reactivity of metal ion doped TiO_2. In addition, there exists no thumb rule for the choice of specific dopant to show high activity due to the complexities involved in multiple variables like preparation method of catalyst, pollutant chosen, irradiation intensity, excitation wavelength, and reactor geometry and so on.

3. Photocatalytic activity of nitrogen doped TiO_2 (N–TiO_2)

Nitrogen doping into TiO_2 matrix is more beneficial from the view point of its comparable atomic size with oxygen, small ionization energy, metastable center formation and stability [90]. The substitution of nitrogen alters both the electronic properties and surface structure of TiO_2, where the former determines the light response range and redox power of carriers, and latter controls the surface transfer of charge carriers [91].

N–TiO_2 prepared by hydrolysis of tetra-isopropyl titanate with 28–30 wt% of NH_3 was used to investigate the photoelectrochemical and optical properties under visible light irradiation [92]. PL measurements of N–TiO_2 and TiO_2 exhibited three kinds of intrinsic states: self trapped excitons, oxygen vacancies and/or surface states [93,94]. From the results of potential regions, it was confirmed that N–TiO_2 involves three types of sub band levels: α, β, and γ in the potential ranges of −0.35 to −0.10 eV, −0.10 to +0.35 eV, +0.35 to +0.65 eV vs NHE respectively (Fig. 2). These were attributed to self-trapping excitons for α, F center (oxygen vacancies trapped two electrons) for β and F^+ center (oxygen vacancies trapping one electron) and/or Ti^{3+} adjacent to oxygen vacancies for γ potential region. Under visible light irradiation, photo-induced holes can oxidize water and/or organic compounds. While the electrons accumulated at the sub band of γ were ineffective to reduce MV^{2+} (methyl viologen), H^+ and Cu^{2+} ions, but had potential to reduce O_2, Pt^{4+}, Ag^+ and Au^{3+} ions which were having more anodic potentials than the γ level [92]. It was demonstrated that the photoexcited N–TiO_2 under visible light irradiation works for reduction of redox species via sub-band of γ and not through the CB (Fig. 3). N–TiO_2 prepared by hydrolysis of $TiCl_3$ and NH_3 solution followed by calcination at 400 °C demonstrated strong photocurrent generation and degradation of 2-proponal under visible light compared to unmodified TiO_2 [95]. The analytical techniques like Fourier Transform Infrared (FTIR) and X-ray photoelectron spectroscopy (XPS) data revealed the presence of complex containing NH_4^+ and titanium on the surface, which decomposed into NH_4^+ facilitating the incorporation of nitrogen atom into TiO_2 lattice on calcination. Phase transformation kinetics of N–TiO_2 was faster due to the presence of nitrogen species compared to the TiO_2 crystallization

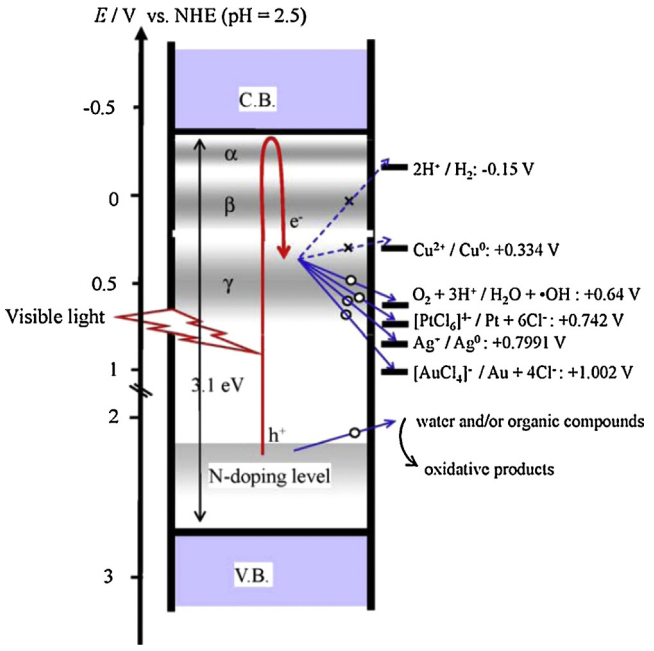

Fig. 3. Energy diagram of N–TiO_2 and photo-induced charge transfer into various kinds of redox species under visible light irradiation. The V.B. and C.B. stand for valence band and conduction band, respectively. The energy levels of sub-bands at the, β, γ potential regions, N-doping levels on the N–TiO_2; and potentials of various kinds of redox species are shown in vs NHE (pH 2.5). Signs of circle and cross stand for energetically favorable and unfavorable electron transfers, respectively.
Reprinted with permission from Ref. [92]. Copyright (2009) Elsevier.

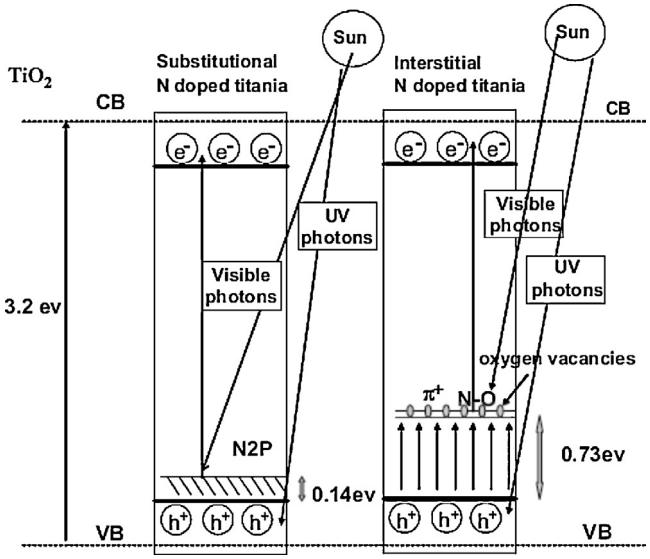

Fig. 4. Electronic band structure of substitutional and interstitial N–TiO_2. Reprinted with the permission from Ref. [98]. Copyright (2008) Elsevier.

prepared by sol–gel method [96]. N–TiO_2 nanocolloid forming titanium oxynitride nanostructures resulted from the nitridation of a porous TiO_2 nanocolloid solution at room temperature showed promising activity for MB decomposition under visible light irradiation compared to Degussa P-25 [97]. The analytical techniques like FTIR, UV–vis Diffuse Reflectance (UV-DRS), Raman scattering, X-ray Diffraction (XRD), XPS and Transmission electron microscopy (TEM) revealed the presence of oxynitride centers because of nitrogen doping into oxygen lattice sites [97]. N–TiO_2 with interstitial nitrogen prepared by microwave method (N–TiO_2–M) using urea showed higher photocatalytic activity for methyl orange (MO) and phenol degradation under visible light than N–TiO_2 with substitutional nitrogen (N–TiO_2–NH_3) prepared by annealing Degussa P25 under NH_3 flow [98]. For N–TiO_2–NH_3, visible light response arises from the occupied N 2p states above the VB edge, while transition from occupied π^* character N–O localized state resulted in visible light response for N–TiO_2–M [99,100]. The highest localized state for interstitial and substitutional species above the top of VB was found to be at 0.73 eV and 0.14 eV respectively (Fig. 4). Therefore interstitial nitrogen states lie higher in the bandgap and excitation from occupied high energy states to CB is more favored compared to N–TiO_2–NH_3. XPS spectra revealed that the nitrogen surface states were bound directly to lattice oxygen in N–TiO_2–M and it was present in positive oxidation state ranged from that of typical hyponitrite species $(N_2O_2)^{2-}$ to nitrite (NO_2^-) or nitrate species ($NO^-{}_3$), while nitrogen was present in the form of N–Ti–N or O–Ti–N in N–TiO_2–NH_3 [101–103]. The hydrothermal preparation route for N–TiO_2 nanorods using TiF_4, HF, and ethylenediamine precursor showed significant activity for the degradation of MB under visible light compared to Degussa P25 attributable to surface wettability (Fig. 5) [104]. The reversible tuning of surface wettability in N–TiO_2 from hydrophobic to hydrophilic was ascribed to kinetically favored adsorption of water molecules onto the surface oxygen vacancies which were formed by the reaction of photogenerated holes with lattice oxygen vacancy [105,106]. This adsorbed water fills the porous regions along the nanorods and replaces the trapped air resulting in hydrophilic surface (Table 1). N–TiO_2 films deposited on aluminium sheets synthesized by reactive magnetron sputtering technique using reactive gas composition $N_2/(O_2 + N_2) = 80$ showed activity for benzamide degradation under UV light [107]. XPS revealed the presence of surface molecularly

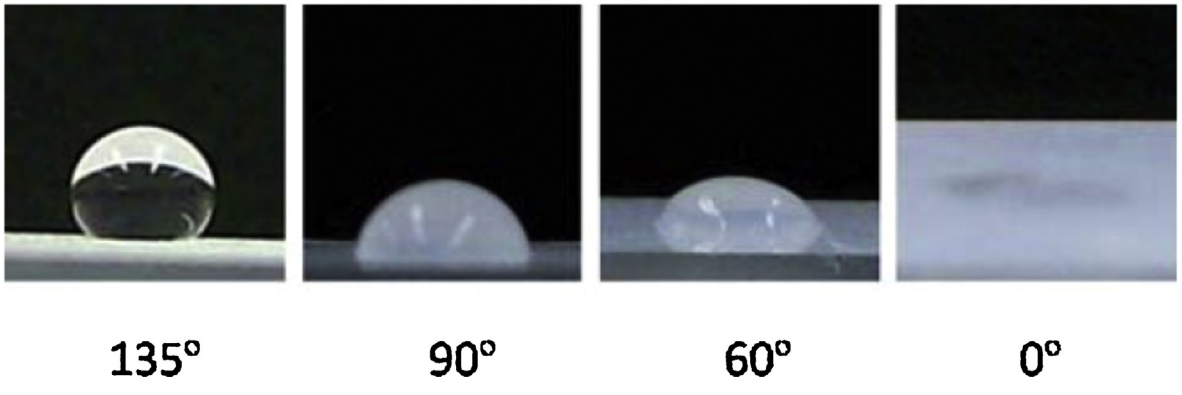

Fig. 5. Photographs of the water droplets on an N-doped TiO_2 film with various surface wettabilities.
Reprinted with the permission from Ref. [104]. Copyright (2010) Royal Society of Chemistry.

Table 1
Contact angle measurements for the N doped TiO_2 samples before and after visible light illumination.

	Contact angles measured per degree	
	Before illumination	After illumination
TiON-6	133	0[a]
TiON-12	133	0
TiON-18	140	0
TiON-24	135	0

Reprinted with permission from Ref. [104]. Copyright (2010) Royal Society of Chemistry.

[a] Water droplet completely spread out.

chemisorbed N_2, doped N^{3-} and solid solution N_2 in the N–TiO_2 matrix. N^{3-} served as charge carrier trap and decreased the average distance between trap site consequently reducing the recombination. In this preparation method, nitrogen doping failed to render visible light response. N–TiO_2 prepared by annealing TiO_2 xerogel powder under NH_3/Ar flow at 500 °C accelerated the MB degradation under visible light compared to Degussa P25 annealed under NH_3/Ar flow [108]. The cooperative effects of specific surface area (70 m^2/g), smaller grain size (10.4 nm), optimal rutile fraction (15%), and appreciable density of oxygen vacancy resulted in excellent activity. During annealing under NH_3/Ar in the temperature range of 500–600 °C, TiO_2 xerogel underwent increase in crystallinity, grain growth, and phase transformation from anatase to rutile along with the formation of mesoporous structure. In contrast, Degussa P25 did not show any textural changes in the physical properties like grain size, anatase–rutile fraction, specific surface area suggesting that these titania polymorphs was subjected to different changes during annealing ambience and microstructure was dependent not only on annealing conditions but also on physicochemical properties of precursor used [108]. N–TiO_2 prepared by high temperature ammonia treatment of anatase TiO_2 showed efficient conversion of formate to CO_2 and H_2O under visible light, but lower efficiency under UV light compared to pure TiO_2 [109]. FTIR suggested that N–TiO_2 have defect sites in the form of Ti–N triple bond and increase of these sites leads to loss of crystallinity resulting in low activity. An optimal synthesis temperature of 550 °C was determined as a balance point between crystallinity and presence of defect sites absorbing visible light photons [109]. In another report, N–TiO_2 films obtained by sputtering the TiO_2 target in a N_2(40%)/Ar gas mixture showed enhanced activity for the photodecomposition of MB and gaseous acetaldehyde under visible light compared to TiO_2 film and N–TiO_2 prepared by annealing TiO_2 powders in NH_3 (67%)/Ar atmosphere [110]. The superior activity was due to the substitutional nitrogen atoms serving as active sites in the form of β-N states, while lower activity of powder form was attributed to high concentration of nitrogen doping in the crystal. The water contact angle measurement revealed that the hydrophilic surface of N–TiO_2 film maintained a contact angle of 6° even after 30 days, while it showed gradual increase for pure TiO_2 film (Fig. 6) [110]. N–TiO_2 films prepared on glass substrate by pulse laser deposition via laser ablation of titanium target in $NH_3/N_2/O_2$ atmosphere exhibited high photoabsorption and MB degradation under visible light irradiation compared to the catalyst calcined in O_2 and N_2/O_2 ambience [111]. Electron deficient nitrogen atoms in N–TiO_2 trap the photogenerated electrons to inhibit the recombination, thereby increasing the quantum efficiency [112]. Moreover, formation of surface hydroxyl species on the film served as the source for generating highly oxidative hydroxyl radicals. The mild heat treatment under the nitrogen atmosphere effectively recovered the photocatalytic ability even after ten times of recycling. N–TiO_2 thin films were deposited on glass substrate by atmospheric pressure chemical vapor deposition using $TiCl_4$, O_2 and N_2O or NH_3

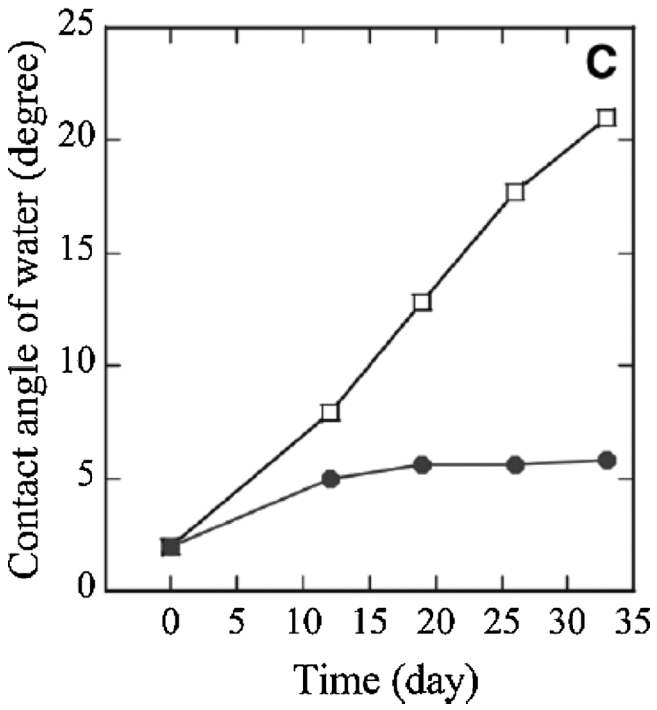

Fig. 6. Contact angles of water as a function of time under interior lighting (with light powers of 28.5 mW cm^2 and 159.4 mW cm^2 in the UV and visible ranges, respectively). All these light powers were measured by the UV radiometer (UVR-2, TOPCON, Tokyo, Japan) with detectors (UD-36 for the UV range and UD-40 for the visible range).
Reprinted with the permission from Ref. [110]. Copyright (2001) Science.

as precursors showed superior photocatalytic decomposition of Rhodamine B (RhB) under visible light compared to pure TiO_2 films [113,114]. This was due to the band gap narrowing and increased hydrophilicity resulting from high density of dentritic islands on thin films [113]. Using NH_3 as nitrogen source, Ti_4O_7 was induced into films and also intermediate products such as $TiNH_2Cl_3$ or TiNCl were produced during the preparation step and generated interstitial titanium and substitutional Cl atom which inhibited anatase to rutile phase transformation [114].

$$TiCl_4(g) + O_2(g) \rightarrow TiO_2(s) + 2Cl_2(g) \quad (7)$$

$$TiCl_4 + 2NH_3 \rightarrow TiNH_2Cl_3 + NH_4Cl \quad (8)$$

$$4TiNCl \rightarrow 3TiN + TiCl_4 + \frac{1}{2}N_2 \quad (9)$$

N–TiO_2 thin films prepared by direct current reactive magnetron sputtering using Ti target in an $(Ar + O_2)/N_2$ gas mixture showed high activity for 2-propanol oxidation under visible light irradiation attributable to nitrogen doping, where oxygen sites were partially replaced with nitrogen atoms simultaneously reducing the TiO_2 [115]. In situ FTIR detection concluded that the photocatalytic oxidation proceeds through the chemisorption of 2-propoxide followed by conversion to acetone, formate species and CO_2 [115]. N–TiO_2 thin films prepared at 425 °C by atmospheric pressure metal organic chemical vapor deposition method deposited on stainless steel using titanium tetra isopropoxide and N_2H_4 as reactive gas mixture in the mole ratio of 2:5 increased the degradation rate of Orange G (OG) under visible light compared to undoped TiO_2 thin films due to the temperature dependent nitrogen incorporation and increase in films crystallinity. However, lower activity of N–TiO_2 under UV light is due to the energy states in the band gap induced by nitrogen doping serving as recombination centers for the light induced charge carriers [116].

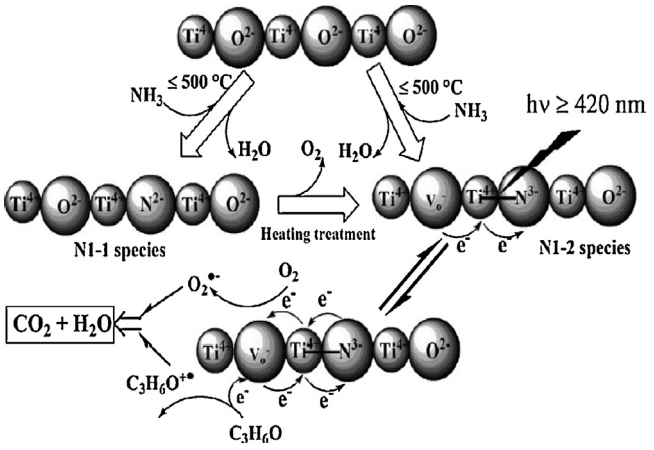

Fig. 7. Structural models of nitrogen species and suggested mechanism for photocatalysis.
Reprinted with the permission from Ref. [117]. Copyright (2010) Elsevier.

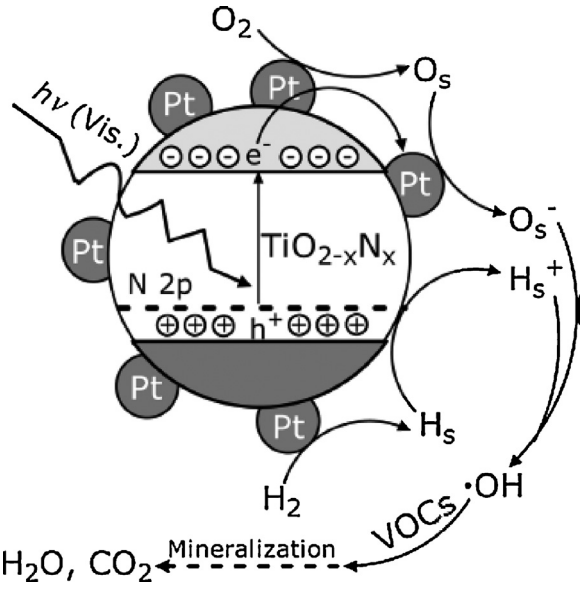

Fig. 8. Proposed mechanism for the visible light photodegradation of VOCs on a $Pt/TiO_{2-x}N_x$ catalyst in the coexistence of H_2 and O_2.
Reprinted with the permission from Ref. [126]. Copyright (2008) American Chemical Society.

The post nitridation of N–TiO_2 at 500 °C resulted in higher photocatalytic oxidation of acetone under visible light compared to N–TiO_2 samples calcined for 20 h at different temperature (400 °C, 450 °C, 550 °C, 650 °C, 700 °C and 800 °C), which was attributed to diamagnetic [O–Ti^{4+}–N^{3-}–Ti^{4+}–V_0^-] photoactive centers containing an oxygen vacancy and nitrogen anion induced on substitution [117]. Electron Paramagnetic Resonance (EPR) results revealed that visible light induces the diamagnetic species to transform into paramagnetic species (Fig. 7), where surface O–Ti^{4+}–N^{3-}–Ti^{4+}–V_0^- species is excited to produce O–Ti^{4+}–N^{2-}–Ti^{3+}–V_0^-, that activates O_2 and acetone molecules leading to complete oxidation. In contrast, N–TiO_2 showed deleterious effect under UV illumination, as these photoactive centers act as electron–hole recombination centers. The results of multiple spectroscopic techniques like near edge X-ray absorption fine structure, XPS, EPR revealed that four kinds of nitrogen species dependent on nitridation temperature; (i) low nitridation temperature (below 500 °C) results in substitutional forms of nitrogen species-diamagnetic [O–Ti^{4+}–N^{3-}–Ti^{4+}–V_0^-] and paramagnetic [O–Ti^{4+}–N^{2-}–Ti^{3+}–V_0^-]; (ii) inert nitrogen species like N–Ti_3 (N co-ordinated to three Ti species) and Ti–N–O observed only at high nitration temperature (>550 °C) [117]. N–TiO_2 films with rutile crystal structure prepared by thermal oxidation of TiN films at 750 °C deposited on titanium substrate by ion beam assisted deposition method showed superior activity for MB degradation under visible light attributed to new state above the VB induced by N^{3-} ion doping [118]. XRD and XPS results concluded that Ti–O–N with a single-phase rutile structure formed by the incorporation of nitrogen atoms into Ti–O–O framework resulting in Ti–O–N bonds. Rice grain shaped N–TiO_2 nano/mesostructures fabricated through combination of sol–gel and electro spinning method was photoactive for the degradation of Alizarin Red S (ARS) under UV light due to nitrogen doping, single crystalline, porous structure with high surface area of ~70 m^2/g [119].

4. Modifications to improve the efficiency of N–TiO_2

The low quantum efficiency and poor oxidative ability of photogenerated holes in N–TiO_2 are still serious obstacles in achieving high degradation efficiency of volatile organic compounds (VOC's). The deposition of noble metals on TiO_2 or N–TiO_2 particles improve the activity as the noble metals act as passive sink for CB electrons promoting the interfacial charge transfer process and enhance the quantum efficiency of photocatalytic system [120–122]. N–TiO_2/PdO thin films (with PdO = 0.5%) synthesized by a sol–gel process demonstrated high activity for humic acid degradation under visible light irradiation because of small band gap (~2.87 eV) with high visible absorbance ability [123]. PdO particles in N–TiO_2/PdO thin films can be reduced to metallic Pd under visible light which creates surface plasmon resonance originating from the collective oscillation of free electrons induced by incident electromagnetic radiation rendering visible light response and also enhances absorption capability for the composite [123]. N–F–TiO_2/PdO nanotube arrays synthesized by dispersing PdO nanoparticles into N–F–TiO_2 nanotube arrays demonstrated excellent photocatalytic activity for MB degradation under visible light compared to N–F–TiO_2 [124]. This enhancement was explained by the rapid hydrophilicity and optoelectronic coupling between dispersed PdO and N–F–TiO_2. Under visible light, N–F–TiO_2 produces electron–hole pair which migrates from N–F–TiO_2 matrix to PdO which locally traps the electron and increases the charge carriers lifetime [124]. PdO/N–TiO_2 nanofiber showed enhanced photocatalytic bactericidal disinfection of *Escherichia coli* (Gram −ve), *Pseudomonas aeruginosa*, and *Staphylococcus aureus* under visible light irradiation compared to PdO/TiO_2 and N–TiO_2 [125]. The enhanced biocidal activity was attributed to nitrogen doping in TiO_2 lattice and incorporation of PdO which acted as an electron trap to prevent charge carrier recombination. The bifunctional photocatalyst Pt/TiO_{2-x} N_x prepared by wet impregnation method showed superior photocatalytic activity and excellent durability for the degradation of VOCs under UV/visible light due to the synergistic effect of nitrogen dopant, deposited metal and the annealing atmosphere [126]. $Pt/TiO_{2-x}N_x$ showed enhancement in the degradation of benzene in H_2–O_2 photo oxidation system compared to pure O_2 system due to the consumption of hydroxyl radical by excess H_2 and production of water which made the system humid hindering the accumulation of carbon on the catalyst (Fig. 8). In addition, it also exhibited excellent performance for the degradation of other VOC's (toluene, ethyl benzene, cyclohexane and acetone) under visible light. The VOC's with high electron density on the ring easily bounds to Pt particles and gets attacked by surface active oxygen species. Contrarily, low conversion of cylcohexane was due to the decrease in electron density of six member cyclic

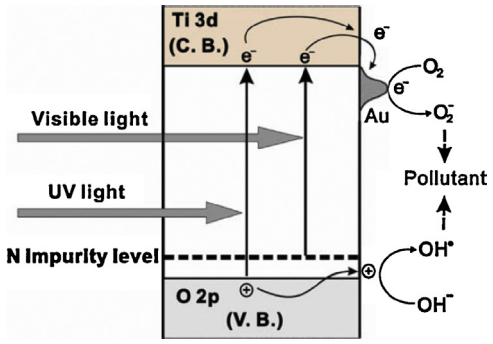

Fig. 9. Proposed mechanism for phototocatalytic degradation of organic pollutant under UV and visible light irradiation over Au/N–TiO_2 photocatalyst.
Reprinted from the permission from Ref. [127]. Copyright (2009) Elsevier.

rings [126]. The proposed mechanism for the degradation of VOC's on Pt/$TiO_{2-x}N_x$ catalyst in H_2–O_2 atmosphere as follows:

$$TiO_{2-x}N_x \rightarrow e^- + h^+ \quad (10)$$

O_2 and H_2 is dissociatively adsorbed on Pt particles give surface O (O_S) and H (H_S) adatoms

$$O_S - Pt + e^- \rightarrow O_S^- \quad (11)$$

$$H_S - Pt + h^+ \rightarrow H_S^+ \quad (12)$$

The resulted adatoms O_S and H_S react with electron and hole respectively to generate $O^-{}_S$ ion and surface $H^+{}_S$. These $O^-{}_S$ ions reacted with surface proton $H^+{}_S$ to generate hydroxyl radicals leading to oxidative degradation:

$$O_S^- + H_S^+ \rightarrow {}^{\cdot}OH \quad (13)$$

$$^{\bullet}OH + VOC's \rightarrow \cdots \rightarrow H_2O + CO_2 \quad (14)$$

The electric field induced surface photovoltage spectra showed the following degradation rate sequence in an O_2 atmosphere with positive potential of +2 V: $TiO_{2-x}N_x < TiO_2 < Pt/TiO_{2-x}N_x$ and $TiO_2 < TiO_{2-x}N_x < Pt/TiO_{2-x}N_x$ under both UV and visible irradiation respectively. The low Surface photovoltage (SPV) signal of $TiO_{2-x}N_x$ under UV irradiation is because of N dopant serving as a charge recombination centers resulting in the fall of UV SPV signal, but it lowered the absorption edge resulting in high SPV response in the visible region. The Schottky barrier formed at the metal–metal oxide interface and Pt acting as a sink for CB electrons promotes charge separation and increases the SPV response in UV/visible region. Pt/$TiO_{2-x}N_x$ showed highest SPV response even in H_2–O_2 atmosphere under similar condition [126]. Gold deposited N–TiO_2 (Au/N–TiO_2 with 2 wt% of Au) prepared by a simple wet-chemical method exhibited enhanced activity for MB degradation under UV light and 2,4-dichloro phenol (2,4-DCP) degradation under visible light compared to N–TiO_2 and Au loaded TiO_2 which was attributed to the synergistic effects of nitrogen doping and Au loading [127]. Improved photocatalytic activity was due to the high density of photo induced electrons and holes generated in short time with N–TiO_2 than pure TiO_2. The electrons were later captured by loaded Au acting as Schottky barrier at TiO_2–Au interface and favor the efficient transfer of electrons from TiO_2 CB to adsorbed O_2 to form superoxide radicals, which initiates degradation reaction (Fig. 9). The degradation rates of 2,4-DCP under visible light irradiation followed the order: 2% Au/N–TiO_2 > 1%Au/N–TiO_2 > 4% Au/N–TiO_2 > N–TiO_2 > 2% Au/TiO_2 ~ pure TiO_2, which was in accordance with PL spectral studies. UV-DRS spectra of Au/N–TiO_2 and Au/TiO_2 exhibited an absorbance band around 550 nm compared with pure TiO_2 and N–TiO_2, which was ascribed to the surface plasmon resonance of metallic Au particles [128–131]. The superhydrophillicity of Ag/N–TiO_2 resulted in stearic acid degradation and antimicrobial killing of *Straphylococcus auereus* EMRSA-16 and *E. coli* ATCC 25922 under UV/white light [132].

N–TiO_2 synthesized by plasma treatment using nitrogen gas and further heat treated in air resulted in faster MB degradation under visible light compared to N–TiO_2 which was subjected to only heat treatment under nitrogen atmosphere [133]. Such a change in activity was due to the low density of oxygen vacancies in the former compared to latter. The increase in the density of oxygen vacancies was due to the removal of doped nitrogen atoms during calcination in nitrogen atmosphere, while the oxygen vacancies disappears as a result of oxidation in air. During the heat treatment in air, non uniform lattice distortion of N–TiO_2 (calculated from Hall's equation) decreased with increasing heat treatment temperature. The optical properties of plasma treated N–TiO_2 before the heat treatment showed the visible light absorption due to simultaneous nitrogen doping and formation of Ti^{3+} defect states caused by oxygen vacancies. The density of oxygen vacancies increased and that of Ti^{3+} decreased during heat treatment, wherein the oxygen vacancies served as recombination centers retarding the visible light activity. However, visible light absorption is decreased after heat treatment due to the structural transformation from $TiO_{2-x}N_x$ to TiO_2 [133]. The enhanced activity of N–TiO_2 nanotube for MB degradation under artificial solar light is attributed to the coupling effects of TiO_2 crystallinity, specific surface area and optimized nitrogen content. Beyond this optimum nitrogen content, photocatalytic activity decreased with increase in nitrogen concentration because of excess oxygen vacancies and Ti^{3+} defects state induced by nitrogen doping served as recombination centers. XRD patterns exhibited a mixture of lepidocrocite and anatase crystal structure suggesting that lepidocrocite play an important role in preserving the tubular structure [134]. N–TiO_2 synthesized via sol–gel method using NH_4Cl as nitrogen source (at pH 3) and calcined at 500 °C showed superior performance for MB and 4-chlorophenol (4-CP) degradation under UV and visible light respectively. This enhanced photoactivity is due to the acidity of precursor solution and calcination temperature impact on the crystallization of xerogel and small particle size [135]. N–TiO_2 prepared at pH 9 using $TiCl_3$ solution and 6 M ammonia solution was effective for gas phase toluene degradation under artificial solar light compared to N–TiO_2 prepared at acidic (pH 4) and neutral (pH 7) conditions due to the presence of large amount of paramagnetic centers (N_b) [136–139]. N–TiO_2 synthesized by modified peroxide sol–gel method using ethylmethylamine as nitrogen source showed excellent activity for MB degradation under visible light [140]. PL spectral studies revealed the trapping of excited electron and hole by oxygen vacancy and doped nitrogen respectively reduced the recombination rate. In addition, electron can also be transferred from VB to new defect levels introduced by nitrogen doping that exists near the CB minimum. Thermal stability of N–TiO_2 examined at different annealing temperatures (300–500 °C) revealed that annealing in air above 400 °C replaces the doped nitrogen from O–Ti–O lattice along with the organics or doped nitrogen is excluded from titania matrix itself [140]. N–TiO_2 with spherical shape and homogeneous size synthesized by a chemical method using $TiCl_3$ precursor and calcined at 400 °C exhibited high photocatalytic activity for MB degradation compared to pure TiO_2 and Degussa P25 under UV/visible light due to the localized nature of nitrogen species within TiO_2 matrix [141]. During the catalyst preparation, Na_2S increases the ionic strength of medium simultaneously inducing in situ formation of transient (NH_4)–TiS_x complex followed by slow hydrolysis results in substitution of nitrogen at lattice sites. Na_2S was also effective in purging dissolved oxygen by H_2S contributes to nitrogen doping in a reductive solution atmosphere. Anatase phase was stabilized even after annealing at 600 °C suggesting that nitrogen dopant stabilized the

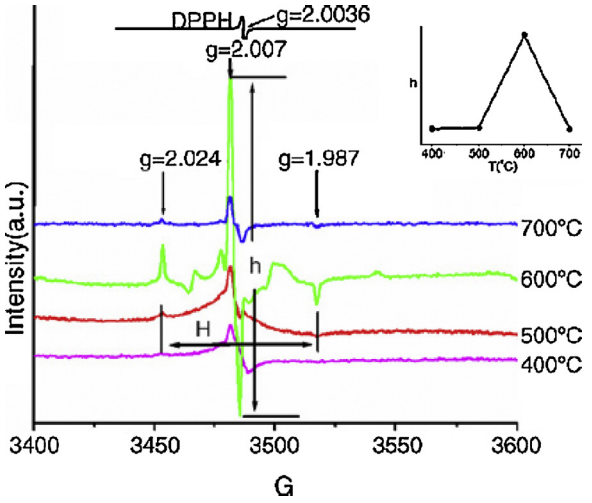

Fig. 10. ESR spectra of N–TiO_2–I (400–700), h = ESR peak height (g = 2.007), H = width between two ESR peaks (g = 2.024–1.987).
Reprinted with the permission from Ref. [142]. Copyright (2006) Elsevier.

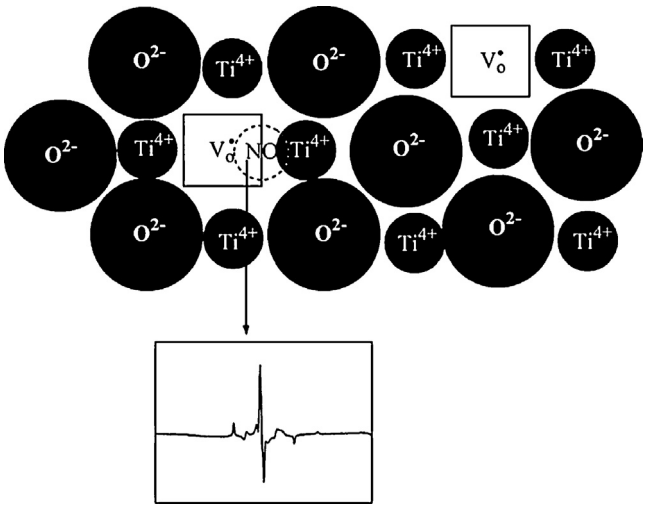

Fig. 12. The model for photoactive center of V_0–NO–Ti: NO is an interstitial molecule between V_0 and Ti in anatase TiO_2 and an O atom in NO links to Ti.
Reprinted with the permission from Ref. [143]. Copyright (2008) Royal Society of Chemistry.

anatase crystal structure. The activity decreased with increase in calcination temperature due to the removal of nitrogen from TiO_2 lattice and it was not due to the change in particle size as evidenced by blue shift in the absorption edge [141]. N–TiO_2 obtained via treating $H_2TiO_5{\cdot}H_2O$ in NH_3 flow at 400–700 °C showed high visible light photocatalytic activity for propylene oxidation (Fig. 10) [142]. In another study, $H_2TiO_5{\cdot}H_2O$ synthesized from $Na_2Ti_2O_5{\cdot}H_2O$ by ion exchange reaction with 0.1 mol/L HCl solution leads to the conversion of orthorhombic $H_2TiO_5{\cdot}H_2O$ into anatase TiO_2 doped with nitrogen. The propylene oxidation increased with increase in temperature up to 600 °C and declined drastically indicating the dependence of NH_3 treating atmosphere for CO_2 production (Fig. 11). ESR results revealed the formation of electron trapped oxygen vacancies and triplet paramagnetic species during the conversion of $H_2TiO_5{\cdot}H_2O$ to TiO_2 [143].

$$H_2TiO_5 \cdot H_2O \rightarrow 2H_2O + 2TiO_2(V_0^{\bullet}) \quad (15)$$

$$TiO_2(V_0^{\bullet}) \xrightarrow{NH_3} N - TiO_2 \quad (16)$$

The high activity was attributed to the synergistic effect of photoactive center $V_0^{\bullet} - N_0 - Ti$ and formation of sub band

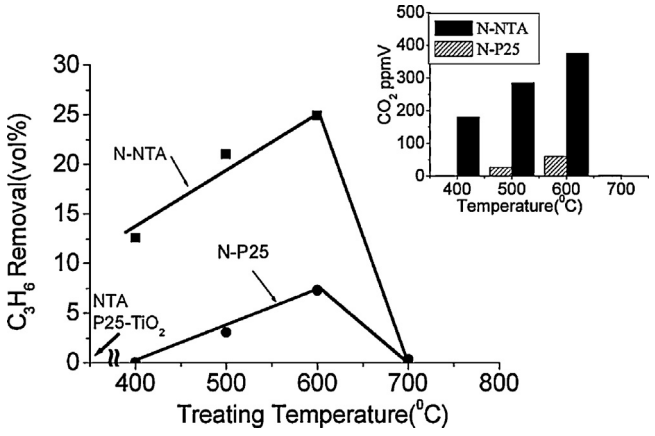

Fig. 11. Visible light photoactivity of N-NTA (400–700) and N-P25 (400–700) evaluated by C_3H_6 removal (vol%). Inset: Change of CO_2 production with NH_3 treating temperature.
Reprinted with the permission from Ref. [143]. Copyright (2008) Royal Society of Chemistry.

originating from the large amount of single electron oxygen vacancies $V_0^{\bullet}$ [144]. ESR study under laser irradiation (λ = 532 nm) indicated that the doped nitrogen stabilized the trapping electron center $V_0^{\bullet}$ and suppressed the PL intensity with consequent enhancement in photocatalysis (Fig. 12). Nanotube titanic acid (NTA, orthorhombic system) was converted to anatase phase accompanied by the formation of $V_0^{\bullet}$ and chemically adsorbed NO [145,146]:

$$TiO_{2-x}\left(V_0^{\bullet}\right)_x \xrightarrow{NH_3} TiO_{2-x-y}\left(V_0^{\bullet}\right)_x + y\,NO. \quad (17)$$

Nitrogen doped dual phase photocatalyst constituting interdispersed protonated titanate (monoclinic $H_2TiO_7{\cdot}xH_2O$) and anatase nanocrystallites synthesized in one-pot process performed well for MB degradation compared to Degussa P25 under UV/visible light which was attributed to the co-operative functioning between surface adsorption and photodegradation [147]. This dual phase photocatalyst surface showed unique affinity for dye adsorption resulting in efficient charge transfer process. N–TiO_2 (anatase) showed higher activity for the degradation of MB under visible light irradiation compared to N–ZrO_2 (cubic) and N–HfO_2 (monoclinic) which was attributed to the increased oxygen vacancies and defects due to nitrogen doping in TiO_2 [148]. N–TiO_2 nanocrystals with mixed phase of anatase (67.0%) and rutile (32.2%) prepared by partial oxidation of TiN at 450 °C in air showed excellent photocatalytic activity for toluene degradation in gas phase under visible light compared to N–TiO_2 nanocrystals prepared at 550 °C, 650 °C and Degussa P25 [149]. The atomic nitrogen content decreased with increase in calcination temperature via removal of nitrogen as N_2 and was replaced by oxygen. Due to the incomplete oxidation, Ti–N bonds were retained and N–Ti–O structure was formed indicating substitutional nitrogen state [150,151]. VB XPS revealed the presence of additional electronic states below 3.05 eV above the VB edge compared to pure TiO_2 attributed to the substitutional N 2p orbitals. Also, Density Functional Theory calculations proved that nitrogen doping favored the formation of oxygen vacancy (V_0) which is located ~0.8 eV below the bottom of CB [149–151]. According to the proposed band gap structure, multiple electronic transitions takes place: (i) energy of visible light (425 nm) is not sufficient to excite electrons from VB to CB as the intrinsic band gap of TiO_2 corresponds to 387 nm (anatase) 410 nm (rutile) (process A); (ii) on nitrogen doping electron is excited from nitrogen impurity level to CB (process B); (iii) excited electrons are trapped or bounds to

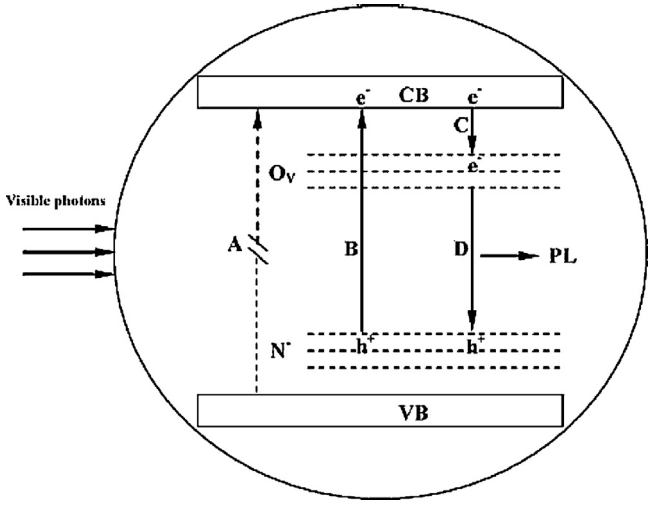

Fig. 13. Schematic diagram of electron transfer process over N-doped TiO_2 nanocrystals under visible light irradiation.
Reprinted with the permission from Ref. [149]. Copyright (2008) Elsevier.

V_0 (process C) and recombines with holes in the nitrogen impurity level (process D) resulting in PL signals (Fig. 13):

$$V_0 + e^-_{CB} \rightarrow V_0^{\bullet} \quad (18)$$

$$V_0^{\bullet} + h^+ \rightarrow V_0 + PL \quad (19)$$

The PL intensity of N–TiO_2 decreased with increasing calcination temperature, due to the low density of V_0 sites which was dependent on nitrogen content. In contrast to the previous literature [152–154], enhanced photocatalytic activity was observed for N–TiO_2 heated at 450 °C in spite of its high PL intensity and results were attributed to the effect of oxygen vacancies [149]. Multi type N–TiO_2 prepared by thermal decomposition of $Ti(OH)_4$ and urea mixtures showed strong visible light absorption due to the coexistence of nitrogen as substitutional N–Ti–O and Ti–O–N as well as π^* character interstitial NO and subsequent formation of localized nitrogen state and oxygen vacancies [155]. The interstitial N–TiO_2 (N_i) showed higher photocatalytic oxidation of gaseous toluene than substitutional N–TiO_2 (N_s) that was attributed to better crystallization, high density of surface hydroxyl groups and enhanced separation of charge carriers as evidenced by PL results (Fig. 14). The proposed band structure of multi type N–TiO_2 illustrates that the electron can be excited from the nitrogen impurity levels (N_s and N_i) to CB with subsequent trapping of electrons by oxygen vacancies which is energetically favored. The photoinduced electrons in the oxygen vacancy and CB may recombine with holes in the nitrogen impurity levels (process E and F) to give rise to PL signals. The oxidation of toluene suggest that initially holes in impurity level (including N_s and N_i states) and electrons in CB were generated under visible light irradiation:

$$TiO_2 - N_s + vis \rightarrow h^+ + e^-_{CB} \quad (20)$$

$$TiO_2 - N_i + vis \rightarrow h^+ + e^-_{CB} \quad (21)$$

These holes and electrons will react with hydroxyl anion and O_2 molecule on the catalyst surface to form hydroxyl and superoxide radicals respectively. The superoxide radicals then interact with H_2O adsorbed to produce more number of hydroxyl radicals which results in complete mineralization of toluene.

$$H_2O \Leftrightarrow OH^-_{(surf)} + H^+ \quad (22)$$

$$OH^-_{(surf)} + h^+ \rightarrow {}^{\bullet}OH \quad (23)$$

$$e^-_{CB} + O_2 \rightarrow O^{\bullet -}_{2(surf)} \quad (24)$$

$$O^{\bullet -}_{2(surf)} + H_2O \rightarrow {}^{\bullet}OH + OH^- \quad (25)$$

$${}^{\bullet}OH + C_7H_8 \rightarrow CO_2 + H_2O \quad (26)$$

It can be inferred from the above results that the surface hydroxyl groups accept holes generated by visible light irradiation to form hydroxyl radicals and prevents recombination [156]. Therefore, it is expected that a greater number of hydroxyl groups yield a higher photocatalytic activity [157,158].

N–TiO_2 with bicrystal anatase (24.6%) and brookite (75.4%) synthesized through a facile solvothermal route using acetylacetone as phase selective agent exhibited maximum photocatalytic decomposition for MB under UV/visible light irradiation compared to Degussa P25 which was attributed to high quantum efficiency induced by large concentration of surface hydroxyl radicals, decrease in the number of Ti^{3+} sites, maximum concentration of chemically bonded active nitrogen species serving as active sites, relatively large surface area and moderate band gap energy [159]. The coupling of brookite and anatase increased the surface hydroxyl groups due to the alteration in the properties of surface external crystal planes induced by variation in phase ratio. Anatase–brookite mixed phase stabilized the charge separation by photoinduced interfacial electron transfer in which transfer of electrons takes place from anatase (3.19 eV) to lower energy brookite (3.11 eV) sites. The results were in excellent agreement with enhanced activity of titania with mixed phase of anatase and brookite in the literature [160–165]. N–TiO_2 with rutile polymorph synthesized by a simple method involving $TiCl_3$, HNO_3 and urea exhibited high photocatalytic activity for MB degradation under visible light compared to commercial rutile TiO_2 and Degussa P25 [166]. The unique synthesis strategy adopted involving urea results in comparatively smaller particle size, higher surface area and lowered point of zero charge value contributed to high activity. The wormlike mesopores N–TiO_2 synthesized by solution combustion method with fuel (titanium nitrate and urea)/oxidizer (oxygen) ratio = 10 and urea:Ti = 10:1 exhibited high photocatalytic activity for the degradation of RhB and selective oxidation of p-anisyl alcohol to p-anisaldehyde under direct sunlight and laboratory light ($\lambda > 420$ nm) compared to other modified N–TiO_2 samples [167]. This was attributed to unique properties like pure anatase phase, smaller particle size (7 nm) and mesoporosity with higher surface area (234 m^2/g) which enhances the adsorption of more reactant molecules on the titania surface, while wormlike mesoporous nature of catalyst decreased the diffusion length for migration of charge carriers to reach active sites and increases the degradation rate [167]. N–TiO_2 (1 atom%) macropores layer with anatase and rutile mixed phase fabricated on Ti substrates by plasma based ion implantation showed superior photocatalytic activity for RhB degradation under visible light [168]. The superior photocatalytic activity of N–TiO_2 (1 atom%) is attributed to the cooperative effect of mixed phase, surface macropores, and interstitial or substitutional nitrogen atoms in TiO_2 lattice [168]. Mesopores N–TiO_2 (with 1:1 ratio of chitosan and TiO_2) synthesized by templating method source exhibited high photocatalytic activity for o-chlorophenol and phenol decomposition under solar and artificial radiation compared to Degussa P25 [169]. The high adsorption and cleavage of aryl-Cl weak bond in o-chlorophenol facile easy hydroxyl radical s attack resulting in faster degradation, while phenol was largely stabilized by resonance resisting its reaction with free radicals. The presence of chloride, carbonate, and bicarbonate were detrimental on phenolic degradation due to: (i) change in pH after addition of salts in aqueous solution of substrates (acidic to alkaline); (ii) carbonate and bicarbonate anions acts as hydroxyl radical

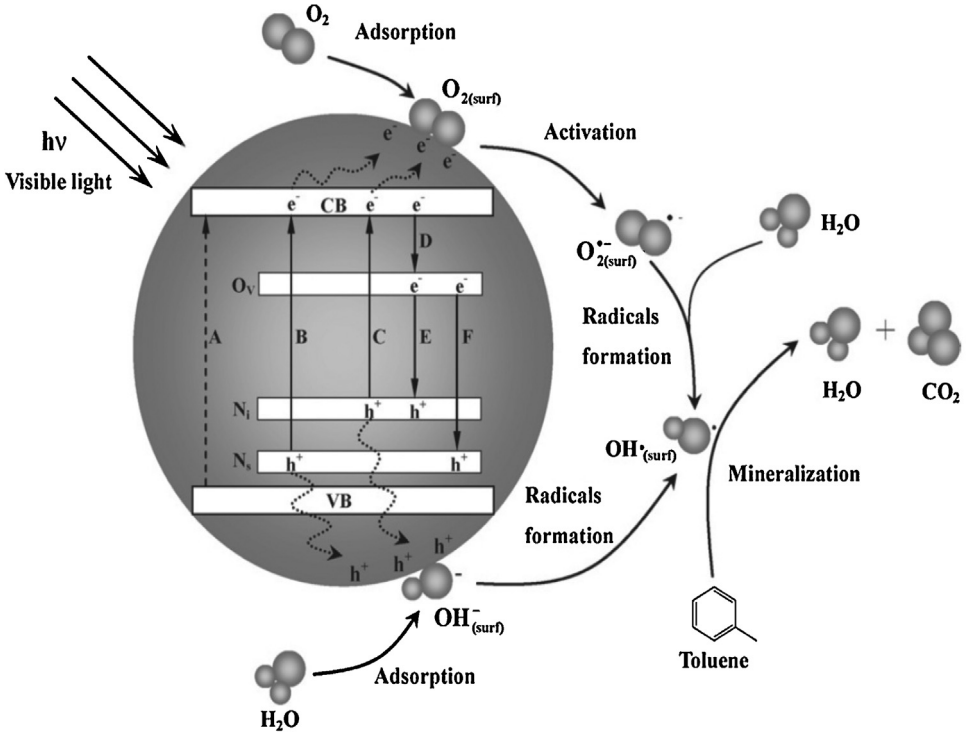

Fig. 14. Proposed band structure of multi-type nitrogen doped TiO_2 and visible light photocatalytic process. Reprinted with the permission from Ref. [155]. Copyright (2009) Elsevier.

scavengers. Maximum degradation of both the phenolics was observed at neutral pH conditions [169].

Compared to Degussa P25, rutile N–TiO_2 prepared by mechanochemical method using high energy ball milling of Degussa P25 powder with hexamethylene tetramine (HMT) mixture at 700 rpm for 120 min followed by calcination in air at 400 °C showed enhanced activity for NO destruction [170]. This was due to the combined chemical reaction between titania and HMT along with the simultaneous phase transformation [171]. The mechanical stressing induced the formation of a fresh oxygen rich surface, which results in the electron transfer from O^{2-} ions of the oxide surface to organic substance leading to the destruction of weak bonds and formation of new bonds between the oxide and non metallic element [172,173]. The high crystal defects induced by planetary milling in the absence of HMT for Degussa P25 did not enhance the charge carrier separation and hence showed very low activity [170]. N–TiO_2 prepared by mechanochemical method via planetary milling of Degussa P25 titania and 10 wt% $(NH_4)_2CO_3$ at milling speed of 700 rpm for 15 min showed excellent ability for oxidative destruction of NO under visible light irradiation, while prolonged milling decreased the activity due to large rutile formation, lattice distortion and powder agglomeration [174]. XRD results suggested that high mechanical energy accelerated the phase transformation from anatase to brookite and rutile, which increased with increase in milling speed and time whereas decreased with increment in $(NH_4)_2CO_3$ content [174]. The ball milling of TiO_2 in $NH_3{\cdot}H_2O$ solution (N–TiO_2) showed activity for monocrotophos degradation under artificial visible light illumination (405 nm) compared to TiO_2 ball milled in H_2O and TiO_2 without ball milling which was attributed to the increased absorption intensity and to the efficient charge carrier generation at the photocatalyst surface [175]. During the ball milling process, the free energy of system is raised by converting mechanical energy of ball milling into distortion energy and defects [176]. The ammonia adsorbed on the defects will be decomposed into nitrogen atoms and then diffuses into TiO_2 lattice. The space left after diffusion is filled with nitrogen atoms rapidly ensuring the non-stop penetration of active nitrogen atoms. Higher the reaction enthalpy, more facile will be nitrogen substitution to form N–TiO_2 during high energy ball milling [175].

N–TiO_2 was prepared by using $NH_3{\cdot}H_2O$ and NH_4NO_3 mixture as nitrogen source for the first time showed a higher efficiency for the 2,4-DCP degradation under visible light at pH 5.87, N/Ti ratio of 2.0 and H_2O/Ti ratio of 76 [177]. XPS results revealed that nitrogen is doped into TiO_2 lattice and also chemically adsorbed on the catalyst surface as N–Ti–O and Ti–O–N respectively. During calcination in air, NH_4^+ was incorporated into TiO_2 lattice to form N–Ti–O and simultaneously oxidized to form Ti–O–N. The activity was improved by the doped nitrogen because of narrowing the band gap. In contrast, photoactivity of N–TiO_2 was reduced by chemically adsorbed nitrogen due to the oxidation states of N_2 covering the catalyst surface and decreasing the number of active sites [178]. H_2O_2 treatment of N–TiO_2 before and after calcination concluded that NH_4^+ ion as a valid nitrogen source for doping, while other nitrogen sources (NO_2 or NO_2^-) cannot be doped [177]. N–TiO_2 with high rutile content prepared by milling Degussa P25 and HMT in atmospheric air showed enhanced photocatalytic activity for RhB degradation under UV/visible light compared to its counterparts with lower rutile content and N–TiO_2 prepared in NH_3 atmosphere [91a]. This high activity was due to high rutile content with favorable surface structure that promoted efficient surface transfer of charge carriers. The spatial overlap of charge carriers is reduced due to the localized nature of surface states resulting in the low recombination and subsequent transfer of surface charge carriers was effective for photocatalytic reactions [91a]. PL studies revealed that the performance of N–TiO_2 has no direct relationship with the amount of surface adsorbed water and hydroxyl groups. In any photocatalytic processes, surface adsorbed water and hydroxyl groups can only be the potential sites to trap holes on the surface, but the final hole transfer needs favorable surface structure to realize this key step. Mesoporous N–TiO_2 prepared via a modified two step hydrothermal route exhibited remarkable photocatalytic degradation of RhB under UV/visible light [91b]. This superior

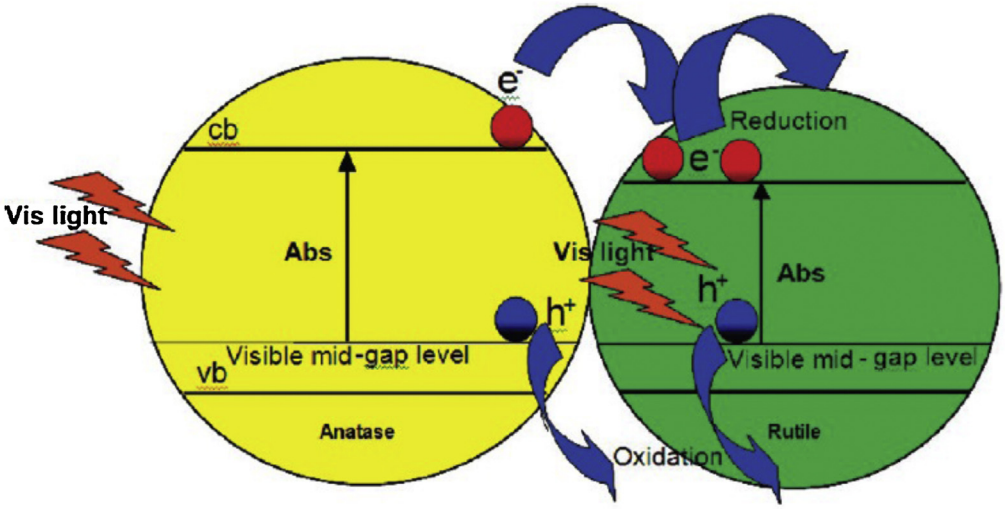

Fig. 15. Electron transfer mechanism in nitrogen doped anatase-rutile heterojunction.
Reprinted with the perimission from Ref. [181]. Copyright (2010) American Chemical Society.

activity is attributed to abundant surface states caused by nitrogen doping and concominant oxygen vacancies which play a vital role in trapping the charge carriers and prolonging their lifetime as evidenced by photoelectrochemical process. N–TiO_2 prepared in $TiCl_3$–HMT–methanol under solvothermal conditions with high anatase phase showed enhanced activity for NO decomposition under visible light illumination compared to N–TiO_2 prepared in $TiCl_3$–HMT–ethanol, $TiCl_3$–HMT–H_2O and Degussa P25 attributed to largest specific surface area (201 m^2/g) [179]. N–TiO_2 synthesized by the homogeneous precipitation in HMT–$TiCl_3$ mixed solution followed by heat treatment in the solution at 90 °C showed high photocatalytic activity under visible light irradiation for the oxidative decomposition of NO(g) [180]. The efficiency with respect to crystal structure followed the order: anatase > brookite > rutile which was in accordance with the sample crystallinity. The efficacy of N–TiO_2 under visible light irradiation with respect to solvent followed the order: methanol > ethanol > 1-propanol > 1-butanol > water. The optimum dopant concentration was 0.2% and reaction rate decreased for higher dopant concentration. This was due to the promotion of electron and hole recombination, since the substitution of O^{2-} by N^{3-} resulted in the formation of oxygen vacancy which served as an electron–hole recombination centers [180]. N–TiO_2 anatase–rutile hetrojunction (with 90% anatase + 10% rutile) synthesized through an ethylenediamine tetra acetic acid (EDTA) modified sol–gel process with 1.5 M EDTA and calcined at 400 °C showed 9 fold enhancement for MB degradation under visible light irradiation [181]. This high activity was found to be as a result of optimum anatase–rutile composition, nanocrystalline nature and band gap narrowing effect of nitrogen. The crystallite size of anatase and rutile were smaller facilitating the formation of more heterojunctions (Fig. 15). The interface between anatase and rutile promotes the electron transfer and rutile works as a reaction site for photoreduction, while photo oxidation can take place either on anatase or on rutile surface. In addition, this sample exhibited low PL intensity due to the effective transfer of photo excited electrons from anatase to rutile thereby leading to lower recombination rates [181].

N–TiO_2 prepared using triethylamine as nitrogen source showed highest photocatalytic decomposition of 2,4-DCP and RhB under visible light compared to N–TiO_2 prepared with other sources like urea, thiourea and hydrazine hydrate (Fig. 16) [182]. Raman and XPS spectra indicated that the chemical environments of doped nitrogen as N–Ti–O and Ti–O–N. The high activity of N–TiO_2 was ascribed to its strong absorption, and lowest PL intensity. The efficient quenching of PL signal by nitrogen dopant in titania was due to the electron trapping by induced oxygen vacancies and hole trap from doped nitrogen.

$$O_v^0 + e_{CB}^- \rightarrow O_v^- \quad (27)$$

$$N^- + h_{VB}^+ \rightarrow N^0 \quad (28)$$

N–TiO_2 synthesized by hydrolysis method using hydrazine hydrate (N^{2-}) as nitrogen donor showed enhanced photocatalytic activity for 4-CP degradation under UV/visible light [183]. In this synthetic route, hydrazine hydrate served as nitrogen source and also reduced Ti^{4+} to Ti^{3+} in N–TiO_2 [184]:

$$NO + O_{surf}^{2-} \rightarrow NO_2^- + e^- \quad (29)$$

$$Ti^{4+} + e^- \rightarrow Ti^{3+} \quad (30)$$

$$NO + 2O_{surf}^{2-} \rightarrow NO_3^- + 3e^- \quad (31)$$

$$3Ti^{4+} + 3e^- \rightarrow 3Ti^{3+} \quad (32)$$

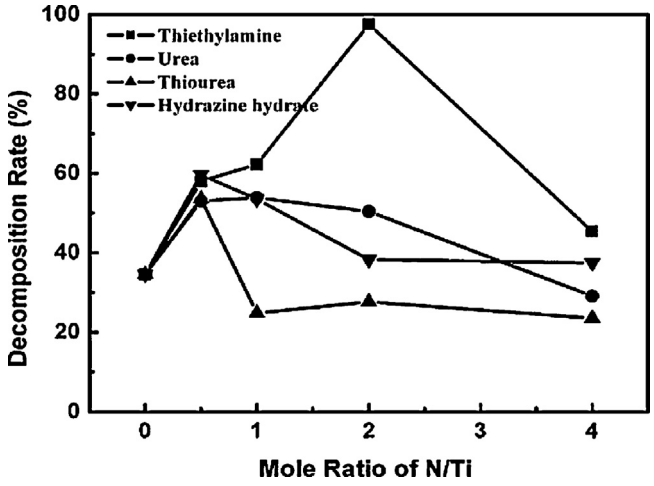

Fig. 16. Photocatalytic decomposition of rhodamine B by N–TiO_2 doped with different nitrogen sources and under various mole ratios of N to Ti.
Reprinted with the permission from Ref. [182]. Copyright (2007) American Chemical Society.

The superior activity is attributed to the synergistic effect of nitrogen dopant and Ti^{3+} species which induced oxygen vacancy states within the band gap of titania. N–TiO_2 prepared by simple wet method at low temperature by treating amorphous TiO_2 powders with hydrazine hydrate (80%) in 110 °C having small crystallite size and large specific surface area exhibited powerful activity for ethylene decomposition and high photochemical stability under visible light compared to undoped TiO_2 [185].

N–TiO_2 prepared by using ammonia–water atmosphere at 100 °C for 4 h was active for the decomposition of reactive red, reactive black and direct green azo dyes under visible light illumination compared to unmodified TiO_2 and Degussa P25 due to the presence of nitrogen groups like –NH, NO_2 and NO that increased the adsorption capacity and hydroxyl radical formation in spite of same crystal size and lower surface area for all the samples. The high adsorption capacity of the photocatalyst surface accelerates the "photosensitizing-oxidation" mechanism resulting in the faster decomposition of dyes [186]. The enhanced activity of N–TiO_2 under visible light irradiation was because of nitrogen doping, smaller particle size (14 nm), increased number of active sites and photosensitized oxidation mechanism [187]. Under visible light, adsorbed dye is excited to singlet (^{1}Dye*) or triplet (^{3}Dye*) state and subsequently the electron is injected from excited dye molecule into TiO_2 CB. The cationic dye radicals can react with reactive oxygenated species and generate intermediates that ultimately lead to degradation.

$$\text{Dye} + h\nu\,(\text{visible light}) \rightarrow {}^1\text{Dye}^* + {}^3\text{Dye}^* \quad (33)$$

$$^1\text{Dye}^* \text{ or } {}^3\text{Dye}^* + \text{TiO}_2 \rightarrow \text{Dye}^{\bullet+} + \text{TiO}_2(e^-_{CB}) \quad (34)$$

$$\text{TiO}_2(e^-_{CB}) + \text{O}_2 \rightarrow \text{O}_2^{\bullet-} + \text{TiO}_2 \quad (35)$$

$$\text{Dye}^{\bullet+} \rightarrow \text{degradation products.} \quad (36)$$

While Degussa P25 showed superior activity compared to N–TiO_2 for Orange G (OG) decomposition under solar light due to the existence of high dispersibility and well developed crystallinity containing anatase–rutile phases with low density of recombination centers. Addition of H_2O_2 with an optimal dosage of 5.0 m mol/L and 15.0 m mol/L showed higher efficiency for OG degradation irrespective of excitation source because of its ability to generate hydroxyl radicals or to trap CB electron.

$$\text{TiO}_2(e^-_{CB}) + \text{H}_2\text{O}_2 \rightarrow \text{TiO}_2 + {}^{\cdot}\text{OH} + \text{OH}^- \quad (37)$$

$$\text{O}_2^{\bullet-} + \text{H}_2\text{O}_2 \rightarrow \text{OH}^- + {}^{\cdot}\text{OH} + \text{O}_2 \quad (38)$$

Meanwhile, degradation efficiency decreased at higher concentration of H_2O_2 as the VB holes was consumed by reactive hydroxyl radicals along with radical–radical recombination [187].

$$^{\bullet}\text{OH} + \text{H}_2\text{O}_2 \rightarrow \text{HO}_2^{\bullet} + \text{H}_2\text{O} \quad (39)$$

$$^{\bullet}\text{OH} + \text{HO}_2^{\bullet} \rightarrow \text{O}_2 + \text{H}_2\text{O} \quad (40)$$

$$\text{TiO}_2\left(h^+_{VB}\right) + \text{H}_2\text{O}_2 \rightarrow \text{TiO}_2 + \text{O}_2 + 2\text{H}^+ \quad (41)$$

$$\text{HO}^{\bullet} + \text{HO}^{\bullet} \rightarrow \text{H}_2\text{O}_2 \quad (42)$$

N–TiO_2 treated with sulphuric acid (0.5 M) synthesized by precipitation method presented superior activity for phenol degradation under UV/visible light irradiation compared to untreated N–TiO_2 and bare TiO_2, despite a decrease in specific surface area (reduced by 50%) and change in pore characteristics were observed upon acid treatment [188]. The adsorbed SO_4^{2-} species increased the surface acidity (0.5–0.9 m mol/g) due to the formation of Bronsted acid centers which favored the degradation reaction [189,190]. The generated surface sulphur complex is potential enough to abstract electron from basic or electron rich molecule enhancing the reaction rate [191]. XPS studies revealed upwards shift in Ti $2p_{3/2}$ binding energy after sulfuric acid treatment, since adsorbed sulfate species forms bidentate bridge structure and strongly abstract electrons from neighboring Ti^{4+} cations [192]. N–TiO_2 loaded with Pt by photo deposition method and dye sensitized with Eosin Y by impregnation method showed high hydrogen evolution rate under visible light with triethanolamine as electron donor due to smaller crystallite size, larger specific surface area, enhanced adsorption of Eosin Y and surface defects induced by nitrogen doping [193]. The Eosin Y chemically adsorbed on N–TiO_2 via carboxyl and phenol hydroxyl group absorb visible light and electrons are excited from HOMO to LUMO. The excited electron transfer to the N–TiO_2 CB and then to the active sites of Pt nanoparticles which favored water reduction into hydrogen. In addition, excited Eosin Y can also transfer its electron directly to Pt and favors hydrogen production [193].

N–SiO_2/TiO_2 (0.05% SiO_2/TiO_2) prepared by treating SiO_2/TiO_2 xerogels in a flow of nitrogen gas bubbled through concentrated ammonia solution was active for ethylene degradation than N–TiO_2 under visible light [194]. The enhanced activity of N–SiO_2/TiO_2 was ascribed to: (i) a large specific surface area which provides more surface sites for the adsorption of reactants molecules, while high pore volume facilitates rapid diffusion of various gaseous products during photocatalytic reactions [195,196]; (ii) the presence of silica in porous N–TiO_2 drastically inhibit the loss of surface hydroxyl group during thermal treatment and hence hydroxyl groups on the catalyst surface will be preserved. Anatase–TiO_2/N–TiO_2 (6:4 weight ratio) composite showed superior photocatalytic activity for the decomposition of NO_x gas under visible light compared to anatase–TiO_2 and N–TiO_2 and other composites with different weight ratio due to decrease in surface area, inefficient electron transfer and poor interparticle contacts [197]. Anatase–TiO_2/N–TiO_2 (6:4) composite showed strong luminous intensity and long life span of singlet oxygen compared to N–TiO_2 ascribed to effective charge carrier separation, while anatase TiO_2 showed no emission of singlet oxygen under visible light. Anatase–TiO_2 accepts an electron which is trapped at Ti^{3+} below 0.8 eV from the bottom of CB which is detrapped to adsorbed O_2, while the hole is trapped on N 2p of N–TiO_2 (Fig. 17). In addition, large surface area of a TiO_2 promoted the electron interaction between adsorbed oxygen with CB electrons and better intimate contact with N–TiO_2 in the composite [197]. The surface adsorbed Fe^{3+} ions on S–TiO_2 or N–TiO_2 treated with $NaBH_4$ and air oxidation was active for 2-propanol and MB degradation compared to unmodified titania under UV/visible light attributed to the efficient trapping of photo excited electrons by Fe^{3+} ions [198,199]. During treatment with $NaBH_4$ and air oxidation, crystal structure of iron compounds on S– or N–TiO_2 changed from γ-Fe_2O_2 to γ-FeO(OH), which was the principle factor for improved activity. ESR measurements confirmed the photo reduction of iron species from Fe^{3+} to Fe^{2+} on the catalyst surface resulting in charge separation. The photoinduced electron transfer from ligand to Fe^{3+} induces oxidative degradation in the presence of O_2. Fe^{3+} ions accept electrons to form Fe^{2+} which diffuses into the solution and then coordinates with dye molecules and these coordination compounds are readily oxidized by O_2 to realize the circulation of photoreduction. The degradation of MB under visible light takes place through opening of a central aromatic ring rather than demethylation as the amount of hydroxyl radicals produced under visible light is much lesser than UV light. The lower quantity of hydroxyl radicals attacks at C–S^+=C functional group rather than methyl group of MB [198]. The modification of N–TiO_2 by adsorbing vanadium species from aqueous solutions of vanadium halides (VCl_2, VCl_3, VBr_2, VI_3, and VCl_4) showed remarkable enhancement for the decomposition of several

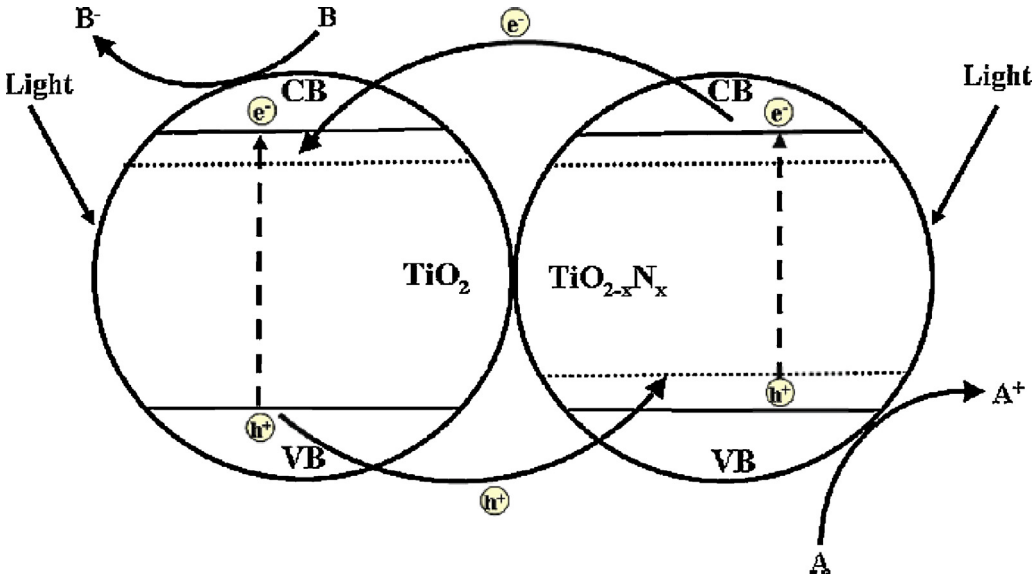

Fig. 17. Mechanism of electron–hole separation in a-TiO_2/N–TiO_2 composites during photocatalysis.
Reprinted with the permission from Ref. [197]. Copyright (2008) American Chemical Society.

VOCs under UV/visible light compared to other samples [200]. The adsorbed vanadium species interacts with surface N–TiO_2 as redox mediator, in which nitrogen impurity is photoexcited under visible light. The photoinduced electrons are effectively trapped on vanadium (+V) to form vanadium (+IV) species, thus suppressing electron–hole recombination. Furthermore, interaction of O_2 with reduced vanadium (+IV) leads to the reoxidation into vanadium (+V) species. Subsequently, formation of active species such as superoxide and hydroxyl radicals initiates a chain reactions resulting in the decomposition of organic compounds. The results of photocatalytic activities suggested that: (i) under UV light irradiation, VCl_3/N–TiO_2 and VCl_3/TiO_2 improves the activity in the same order similar to bare N–TiO_2 or TiO_2, while VCl_3/TiO_2 does not work under visible light irradiation (Table 2). (ii) photocatalytic activity of N–TiO_2 with various vanadium halide species followed the order: VCl_2/N–TiO_2 < VCl_3/N–TiO_2 < VCl_4/N–TiO_2. Thus the vanadium species with higher oxidation state resulted in higher photocatalytic activity: (iii) VCl_3/SiO_2 did not exhibit photocatalytic activity indicating that vanadium species by itself do not participate in photocatalytic reaction under UV/visible light: (iv) photocatalytic activity values of VCl_3/N–TiO_2, VBr_3/N–TiO_2 and VI_3/N–TiO_2 are nearly the same suggesting that photocatalytic activity of N–TiO_2 is not influenced by halides, rather it was critically governed by vanadium oxide species [200].

Table 2
Yields of photo-formed CO_2 for the photodecomposition acetic acid on various samples under λ > 420 nm and λ > 320 nm for 3 h.

Samples[a]	Yields of CO_2/μmol	
	λ > 420 nm	λ > 320 nm
N–TiO_2	1.2	16.4
VCl_2/N–TiO_2	13.4	39.2
VCl_3/N–TiO_2	17.0	40.8
VBr_3/N–TiO_2	16.5	39.8
VI_3/N–TiO_2	18.0	41.0
VCl_4/N–TiO_2	18.8	48.0
TiO_2	Trace	27.0
VCl_3/TiO_2	Trace	42.6
VCl_3/SiO_2	Trace	Trace
SiO_2	Trace	Trace

Reprinted with permission from Ref. [200]. Copyright (2008) Elsevier.
[a] The loading of vanadium on samples were adjusted to be ca 1.0 at%.

5. Photocatalytic activity of co-doped N–TiO_2 (X–N–TiO_2)

The coupling of one dopant with the second has been proposed to enable a reduction in the number of carrier recombination centers by proposed charge equilibrium mechanism as well as enhancing visible light absorbance by increasing the solubility limit of dopants [201,202]. It is generally accepted that electronic coupling between two dopants is the key to realize synergistic effects of codoping on photocatalytic activity [203,204]. Fe–N–TiO_2 prepared by sonochemical method exhibited activity for IC degradation under solar simulator compared to Degussa P25 and N–TiO_2 because of large band gap narrowing. The iron doping forms a new energy level below CB and nitrogen dopant above VB or hybridization of N 2p and O 2p orbitals results in visible light response in this codoped catalyst. The shallow trap states of iron dopant traps electrons or holes to reduce recombination [205]. Cd–N–TiO_2 was beneficial for RhB decomposition under visible light irradiation in the presence of H_2O_2 [206a]. This was attributed to the synergistic effects of interstitial nitrogen atoms and H_2O_2/TiO_2, which inhibits the recombination enabling the reaction of trapped holes with H_2O_2 to generate hydroxyl radicals. While Cd^{2+} distributed on the TiO_2 surface prevented the aggregation of TiO_2 particles resulting in smaller particle size [206a].

The co-doping of cerium and nitrogen showed best photocatalytic performance for nitrobenzene degradation under visible light compared to Degussa P25 and retained its activity even after six times of recycling. XRD and XPS results suggested that nitrogen atoms were incorporated into the crystal lattice and distorted the crystal structure resulting in visible light response, where as cerium in the form of Ce_2O_3 suppressed the recombination. The doping of nitrogen made the catalyst porous with large specific surface area, while cerium dopant induced well crystallized anatase mesostructure [206b]. Ce–N–TiO_2 hollow sphere illustrated 97.8% degradation of Reactive Red dye X-3B under visible light irradiation due to cooperative effects of nitrogen and cerium doping. The nitrogen doping resulted in intense increase in visible light absorption. The electrons are excited from VB of codoped titania into Ce 4f level which reacts with adsorbed oxygen to form oxidizing species. The excited electrons are trapped at Ce^{4+}/Ce^{3+} sites and are transferred to surface adsorbed oxygen reducing recombination [206c].

Sm–N–TiO_2 showed strong visible-light response and high photocatalytic activity for 4-CP degradation under visible light

attributed to cooperative effect of doping nitrogen and Sm^{3+} ions. Sm^{3+} ion dopant in TiO_2 exists in the form of Sm_2O_3, when combined with N–TiO_2 to forms binary metal oxide [207a]. Sm^{3+} trap the electron and easily detraps it to adsorbed O_2 on the TiO_2 surface to produce reactive oxygenated radical:

$$Sm^{3+} + e^- \rightarrow Sm^{2+}(\text{electrontrapping}) \quad (43)$$

$$Sm^{2+} + O^{2-} \rightarrow Sm^{3+} + O_2^-(\text{electron transfer}) \quad (44)$$

$$O_2^- + 2H^+ \rightarrow 2OH^{\bullet}(\text{generation of oxidative species}) \quad (45)$$

La–N–TiO_2 showed improved activity for RhB decomposition under visible light attributed to synergistic effect of codoping [207b]. The La^{3+} ion acts as electron trap and accelerates the charge carrier separation while, nitrogen doping narrowed the band gap. The optimum concentration of La to show high activity was found to be 0.1%. At this optimum concentration, surface barriers becomes higher and space charge region gets extended leading to the efficient separation of electrons and holes due to large electric field experienced by photogenerated charge carriers. Above the optimum level, space charge region becomes very narrow and the penetration depth of light into TiO_2 greatly exceeds the thickness of the space charge layer, which increases the recombination rate of electrons and holes. Thus, optimum concentration of dopant ions is always necessary to make the thickness of the space charge layer substantially equal to the light penetration depth [207c]. The co-doping of nickel and nitrogen not only prevented the phase transition from anatase to rutile but also leads to visible light activity for formaldehyde degradation [208]. Nickel dispersed on the TiO_2 surface inhibited the recombination, while nitrogen doping resulted in band gap narrowing leading to visible light activity for the codoped catalyst [208]. W–N–TiO_2 synthesized via hydrolysis method and calcined at 500 °C exhibited high selectivity for nitrate reduction under visible light compared to their single ion doped or undoped counterparts [209a]. This high activity was attributed to synergistic effect of tungsten and nitrogen codoping, optimum surface hydroxyl group density, mesoporosity and visible light absorption of the catalyst. XRD patterns revealed the shift of 1 0 1 peak towards lower d value indicating tungsten doping in the form of W–O–Ti bonds. XPS studies showed the high intense peak at 532 eV indicating the increased hydroxyl ion concentration due to tungsten doping [209a]. It is reported that doping of tungsten in TiO_2 lattice leads to the appearance of Lewis and Bronsted acid sites and therefore increases the surface acidity [210,211]. Such surfaces will have higher affinity to the species with unpaired electrons and can easily adsorb hydroxyl groups and water, which are essential for the hydroxyl radical generation. The addition of hole scavenger (formic acid) increases the reduction activity. Formic acid undergoes oxidation by reacting with hole to form CO_2^- species which has large reduction potential of 1.8 V compared to an electron (0.29 V) and acts as an driving force for nitrate ion reduction [212].

$$HCOO^- + H^+ \rightarrow 2H^+ + CO_2^{-\bullet} \quad (46)$$

Photocatalytic activity with respect to product selectivity revealed that nitrate reduction to nitrogen proceeds via nitrite formation and not by NH_4^+ formation which was facilitated by the presence of CO_2^- species (Fig. 18):

$$NO_3^- + HCO_2^- + H^+ \rightarrow NO_2^- + CO_2 + H_2O \quad (47)$$

$$NO_3^- + 3HCO_2^- + 7H^+ \rightarrow NH_4^+ + 3CO_2 + 3H_2O \quad (48)$$

$$NO_3^- + HCO_2^- + 11H^+ \rightarrow N_2 + CO_2 + 6H_2O \quad (49)$$

Mesoporous W–N–TiO_2 synthesized via one step solution combustion method and UV pretreated for 1 h showed ~12 fold

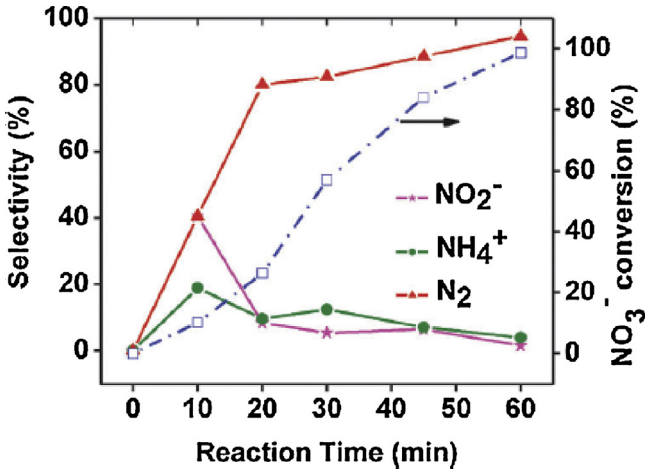

Fig. 18. Correlation of nitrate photoreduction and product selectivity with reaction time over 2-WTiN photocatalyst.

Repirnted with the permission from Ref. [209a]. Copyright (2011) Royal Society of Chemistry.

enhanced RhB degradation under UV/visible light compared to Degussa P25 and UV untreated N–W–TiO_2. The UV pretreatment of W–N–TiO_2 with 5 ml of 50% methanol–H_2O (w/w) produced atomic hydrogen under intense UV irradiation, reducing Ti^{4+} to Ti^{3+} resulting in visible light absorption. The lower activity of untreated W–N–TiO_2 was due to the presence of carbon residues on the surface which promotes the recombination process. While UV treated W–N–TiO_2 removed carbon impurities and XPS studies showed ~2% decrease in carbon content and increase in oxygen amount after UV treatment which was crucial for degradation process. The UV treatment increases the wettability of TiO_2 facilitating water adsorption and hydroxyl radical formation [209b]. The degradation of RhB and 2,4-DCP was faster with thermally stable W–N–TiO_2 under UV/visible light compared to that of Degussa P25, N–TiO_2 and pure WO_3. The nitrogen dopant forms new states above VB, while tungsten forms below CB generating energy states like N–Ti–O, N–W–O, Ti–O–N and W–O–N linkages (confirmed by XPS) which narrowed the band gap. EPR result illustrated the presence of oxygen vacancies induced on codoping traps the electrons to produce active species. The high chemical affinity of tungsten modified titania surface facilitates nitrogen species to coordinate with tungsten dispersed on titania to form N–W–O linkages. In addition W^{6+} near the bottom of CB also traps the excited electrons and inhibits the recombination, additionally contributing to overall efficiency [209c].

Ta–N–TiO_2 thin films fabricated by RF magnetron sputtering was active for oleic acid decomposition under visible light irradiation attributed to the positive shift of N 2p narrow band caused by donor (Ta)-acceptor (N) interaction and charge compensation. The calculated electronic structures of Ta–N–TiO_2 suggested that the complete Ta and N neigbouring lead to the hybridization of N 2p and O 2p producing delocalized and dispersed VB which generates holes with high mobility favorable for photocatalysis. In addition, changes in incident photon to current conversion efficiency (IPCE) spectra in presence of SCN^-, Br^- and I^- as reductants proved that the holes produced in N 2p band of Ta–N–TiO_2 under visible light had higher oxidation power than N–TiO_2 [209d]. Cu–N–TiO_2 (with N = 0.6 wt% and Cu = 0.8 wt%) exhibited enhanced photocatalytic activity under visible light for xylenol orange decomposition due to mixing of N 2p with O 2p leading to visible light response and that copper oxide absorbs to longer wavelength increasing the absorption intensity [213]. Sr–N–TiO_2 (0.5 mol% of Sr^{2+}) prepared by polymerized complex (PC) method exhibited better performance

Table 3
Characterization and visible light photocatalytic activity of codoped titania prepared by polymerized complex (PC) method. All the metal ion dopants had concentration of 0.5 mol%.

	Ionic radius of metal ion (Å)	Colour	BET surface area (m^2/g)	Crystalline structure	Rate of CO_2 evolution (ppm/h)[a]
PC–N–TiO_2	–	Gray	6	Rutile	7
PC–K–N–TiO_2	1.52	Pale gray	2	Rutile	4
PC–Ca–N–TiO_2	1.14	Pale green	11	Anatase/rutile	21
PC–Sr–N–TiO_2	1.32	Pale yellow	28	Anatase/rutile	87
PC–Ba–N–TiO_2	1.49	Pale yellow	40	Anatase/rutile	20
PC–Nb–N–TiO_2	0.78	Pale blue	9	Anatase/rutile	0.4
PC–Fe–N–TiO_2	0.69	Brown	6	Anatase/rutile	4
PC–Zn–N–TiO_2	0.88	Pale gray	3	Rutile	0
PC–Al–N–TiO_2	0.68	White	17	Anatase/rutile	0

Reprinted with the permission from Ref. [214]. Copyright (2004) Materials Research Society.
[a] Degradation experiments carried out using 500 W xenon lamp equipped with UV and infrared cut-off filters as excitation source.

for acetaldehyde decomposition under visible light irradiation compared to other dopant metal ions (K^+, Ca^{2+}, Ba^{2+}, Nb^{5+}, Fe^{3+}, Zn^{2+} and Al^{3+}), N–TiO_2 and sol–gel Sr–N–TiO_2 (Table 3) [214]. The strong activity of Sr–N–TiO_2 was attributed to the large BET surface area, high crystallinity and absorption of light in the wavelength range of 400–500 nm. Importantly, codoping was achieved without the formation of Ti^{3+} defects that otherwise served as recombination sites. ESR spectra revealed triplet signals (g = 1.983, 2.004, 2.002) assigned to paramagnetic nitrogen species (e.g. NO, NO_2, NO^{2-}, $NO_2{}^{2-}$) [215,216]. It is reported that NH_3 was doped into the precursor oxide reacting with lattice oxygen to form paramagnetic nitrogen species rendering visible light response [214]. The optimal dosage and uniform distribution of Sr^{2+} in TiO_2 prior to calcination also contributed to high activity. The superior photoelectrocatalytic activity of Zr–N–TiO_2 nanotube for 4,4′-dibromobiphenyl degradation at low potential of 1.0 V under UV light followed the order: Zr–N–TiO_2 > Zr–TiO_2 > TiO_2 indicating that codoping of zirconium and nitrogen made it easier to absorb more light and transfer more photo induced electrons and holes [217]. However, degradation rate decreased for applied potential > 1.0 V indicating the existence of optimum potential for efficient degradation. The degradation proceeds through debromination as evidenced by the concentration of bromide ion, formation of intermediates and pH value during the course of reaction [217]. Both Fe–TiO_2 and Fe–N–TiO_2 showed poor photocatalytic performance for RhB degradation compared to pure TiO_2 under UV/visible light in spite of their large band gap narrowing [218]. The photocatalytic performance and terephthalic acid fluorescence studies showed that iron doping modified the surface charge transfer and carrier trapping behaviors by changing the electronic band gap structure of TiO_2 (Fig. 19). Moreover, iron dopant suppresses the transfer of photogenerated charges to the surface of TiO_2 and decreases the redox reactions producing hydroxyl radicals implying that energy levels of iron dopant promoted the radiative recombination through quantum tunneling and also by lowering the mobility of excited carriers. However for N–TiO_2, interstitial nitrogen do not change the surface charge transfer, carrier trapping and recombination behaviors of pure TiO_2 leading to the significant photocatalytic efficacy under visible light range [219,220]. The high activity of C–N–TiO_2 films for MO degradation under visible light was attributed to the formation of Ti–O–N–C chemical bond as revealed by XPS and IR analysis and presence of oxygen vacancies induced by Ti^{3+} species within the band gap states of titania [221].

The biocidal activity of S–N–TiO_2 for *E. coli* inactivation was attributed to interstitial nitrogen doping and substitutional sulphur doping both at Ti^{4+} and O^{2-} sites [222]. S–N–TiO_2 nanotube array prepared by two step electrochemical anodization method showed higher photocurrents and faster MB degradation under visible light compared to undoped TiO_2 nanorod arrays films as a result of improved charge carrier separation [223]. Moreover, surface defects induced by incorporated nitrogen and sulphur atoms served as catalytic centers. XPS analysis revealed that nitrogen existed as N–Ti–O and N–O–Ti forms and that sulphur was incorporated at O^{2-} lattice sites [223]. S–N–TiO_2 was prepared by manually grinding commercial anatase powders and annealed at 400 °C in two crucibles with different surface-to-volume ratio (S/V = 20 and 1.5). S–N–TiO_2 with S/V = 20 (DTKP 102-A) showed high *E. coli* inactivation under visible light irradiation compared to S–N–TiO_2 with S/V = 1.5 (DTKP 102-B) and undoped TiO_2 [224]. The high *E. coli* inactivation by DTKP 102-A was due to the electronic promotion from nitrogen, sulphur localized states to the CB by leaving a localized hole in VB. The electrons in CB react with molecular oxygen previously adsorbed on oxygen vacancies producing superoxide radicals [225–227], which may be oxidized by the holes trapped on the midgap nitrogen and sulphur states leading to singlet oxygen thereby inactivating *E. coli* (Fig. 20). I–N–TiO_2 displayed high photocatalytic activity for MO degradation under UV/visible light compared to their monodoped counterparts and Degussa P25 [228]. The doping of iodine created energy levels within the band gap states of TiO_2 and this sub transition ($I^{+7}/I^{5+}/I^-$) improved the visible light response [229]. I^{7+} and I^- serves as electron and hole traps respectively preventing recombination. Self disproportionation reaction during heat treatment process leads to the formation of heptavalent iodine (I^{7+}) and negatively charged iodine (I^-) species.

$$4IO_3^- \rightarrow 3IO_4^- + I^- \quad (50)$$

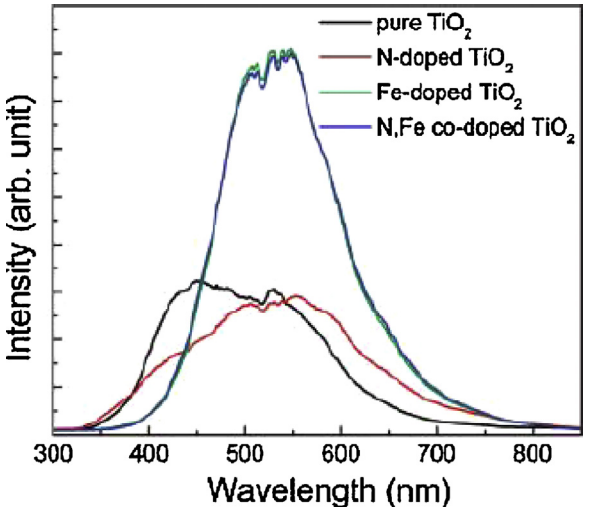

Fig. 19. Photoluminescence spectrum (PL) of pure, N-doped, Fedoped, and N/Fe-codoped TiO_2 at 10 K.
Reprinted with the permission from Ref. [218]. Copyright (2010) American Chemical Society.

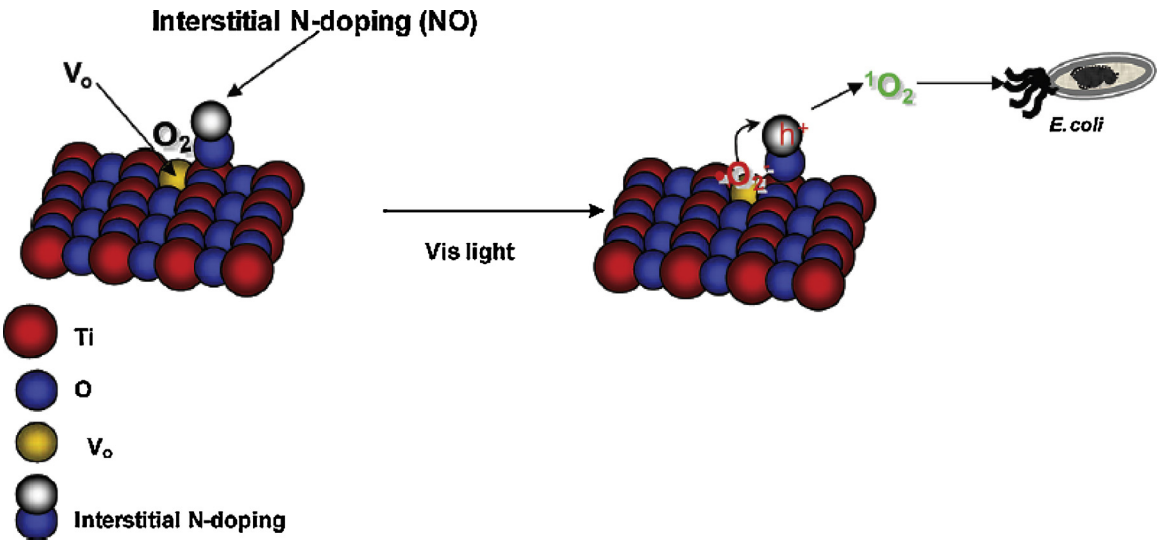

Fig. 20. Mechanism of Singlet Oxygen Formation on D-TKP-102-A Surfaces.
Reprinted with the permission from Ref. [224]. Copyright (2010) American Chemical Society.

COD analysis revealed that MO degradation takes place in a two step manner where the preliminary steps involves cleavage of chromophore (–N=N–) and secondary step results in complete mineralization [228].

The codoping of nitrogen and fluorine via anodizing titanium in HF and heat treatment in NH_3 atmosphere degraded MO under visible light at a faster rate compared to bare titania [230]. The unexpected incorporation of fluorine species during either anodizing or annealing promoted the formation of surface oxygen vacancies which strongly modifies the surface band structures with appearance of intraband states leading to the formation of radical species by adsorbing molecular oxygen on site [231]. XRD and Raman studies suggested that nitrogen doping facilitated the phase transition of titanium nanotube to rutile at low annealing temperature [230].

The high tendency N–F–TiO_2 for microcystin-LR degradation under visible light at acidic pH of 3.0 attributed to its versatile structural properties like high surface area (141 m^2/g), high porosity (49%), mesoporous structure (2–10 nm pore size) and low degree of agglomeration. The oxygen vacancy concentration increased in the titania matrix upon fluorine substitution which served as active sites for the generation of oxidizing species. However degradation rate decreased at higher pH suggesting the critical dependence of solution acidity/basicity, electrostatic interaction between microcystin-LR and N–F–TiO_2, surface charge density of catalyst and interaction of pollutant with free radicals depending on their molecular structure [232]. The activity of F–N–TiO_2 for acetaldehyde, trichloroethylene and toluene decomposition under UV/visible light irradiation was ascribed to combined effects of doped nitrogen and fluorine [93]. The highly porous and strong acidic surface favored the adsorption of pollutant on F–N–TiO_2 surface [233]. Moreover surface acidity site also acted as electron acceptor, enhancing charge carrier separation [234]. The doped nitrogen improved visible light absorption, while doped flourine atoms led to the formation of oxygen vacancies (F and F^+ i.e., oxygen vacancies trapped with two and one electrons respectively) which is critical for superoxide and hydroxyl radical generation [235–237]. F–N–TiO_2 inverse opal (IO) films with hierarchical meso-/macropores improved visible light response for MB degradation compared to other F–N–TiO_2 films without IO structure due to the combined effects of stopband effect, multiple scattering, Ti^{3+} generation and nitrogen and fluorine codoping [238]. UV–vis absorption analysis exhibited red edge of stopband peaks (433 nm, 487 nm, 671 nm) for F–N–TiO_2 in the visible light range (400–760 nm) indicating a slow photo effect. Moreover, multiple scattering effects of IO's due to macropores can increase the effective optical path length of light in F–N–TiO_2 IO films and can also enhance the photo absorbance [239–243]. In addition, high porosity of structure favors the transportation and adsorption of dyes and H_2O molecules more effectively. However, multiple scattering effect of macroporous structure is more pronounced than the slow photon effect of F–N–TiO_2 IO's for facilitating visible light photocatalysis. F–N–TiO_2 exhibited better photostability and adsorbility even after ten cycles for MB degradation under UV/visible light [238]. F–N–TiO_2 synthesized by the hydrolysis of tetra butyl titanate with ammonium fluoride and calcined at 350 °C showed 2.4 times superior activity for phenol degradation under visible light compared to Degussa P25 and other doped samples. This was ascribed to the smaller particle size and higher adsorption towards the organic substrate, both of which were cooperative to facilitate the organic molecule accessible to the active sites of TiO_2 surface [244]. F–N–TiO_2 exhibited mesoporous structure which allowed rapid diffusion of various liquid reactants and products thus enhancing the reaction rate. XRD results revealed that codoped TiO_2 contained only anatase phases even at 1000 °C indicating that ammonium fluoride added during preparation process retarded phase transformation from anatase to rutile [244]. F–N–TiO_2 prepared by hydrothermal route using NH_4HF_2 as both nitrogen and fluorine precursor at 80 °C for 2 h degraded gaseous toluene in air under UV light compared to other samples calcined in the range of 300–600 °C [245]. This high photoactivity of uncalcined sample is attributed to high specific surface area which provided more active sites and photocatalytic reaction centers for the reactant molecules. Further, large pore volume allows reactant molecule to reach the active sites on the surface along with high percentage of surface ≡Ti–F group that suppress the recombination. In contrast, F–N–TiO_2 calcined at 300 °C showed superior activity for RhB and gaseous acetone degradation under visible light which was ascribed to the enhanced crystallinity and decreased defect density. Due to shielding effect of surface fluorination, phase transformation from anatase to rutile as well as removal nitrogen dopants from F–N–TiO_2 matrix during annealing was significantly inhibited [246a]. This enhanced thermal stability was associated with the restricted direct contacts between anatase nanocrystals protected with fluorine. Surface fluorination facilitated the dominant crystal growth changing from Ostwald ripening to oriented attachment [245]. Cl–N–TiO_2 synthesized through simple one step sol–gel

reactions in presence of NH_4Cl was beneficial for RhB and phenol degradation under visible light compared to N–TiO_2 and Degussa P25 attributed to small crystallite size, intense light absorption and narrow band gap. XRD results indicated that codoping with nitrogen and chlorine retarded the anatase to rutile phase transition [246b].

B–N–TiO_2 particles [247] and B–N–TiO_2 [248] nanotube arrays exhibited excellent activity for pollutants degradation due to the presence of Ti–O–B–N surface states. These states originate from electronic coupling between the codoped boron and nitrogen suggesting the positive correlation of synergistic effect on photocatalytic activity. Ti–O–B–N surface states generates partially occupied localized states in the band gap with enhanced visible light absorption and leads to the creation of electron hole pair with sufficient oxidizing power to allow photo-oxidation reactions. In addition, Ti–O–B–N moiety acts as a photocatalytic "hot site" to promote surface separation and transfer of carriers by trapping holes [247]. This is due to the localized nature of Ti–O–B–N states contributing to a more effective physical separation of surface reduction and oxidation reactions by minimizing the state overlap that would contribute to electron hole recombination [247]. B–N–TiO_2 synthesized by doping boron first and subsequently by nitrogen in NH_3 at 550 °C (nitrogen doping atmosphere) exhibited highest photocatalytic activity for MO decomposition under UV/visible light compared to B–N–TiO_2 prepared by calcining at different temperature (500 °C, 600 °C, 650 °C) with various nitrogen content [249]. This highest activity at 550 °C is due to the high nitrogen content leading to more oxygen vacancies resulting in high absorbance intensity in visible light range. At 550 °C, main forms of doped boron and nitrogen are Ti–O–B–N or Ti–O–N and Ti–O–B bonds play a vital role on photocatalytic activity under visible light. When nitrogen doping temperature is higher than 600 °C, Ti–O–B–N structure is unstable and transforms into Ti–O–B or Ti–B and Ti–N bonds leading to poor activity (Fig. 21) [249]. B–N–TiO_2 nanorods prepared by using TiN as precursor by two step hydrothermal method showed high MO degradation and a better photocurrent response than N–TiO_2 nanorods under visible light attributable to the synergistic effect of B–N-doping [250].

C–S–N–Fe tetra doped TiO_2 synthesized by a facile sol–gel method showed superior photocatalytic activity for RhB degradation under visible light compared to undoped TiO_2, which was due to the generation of new impurity levels within the band gap states of titania [251]. In such a situation, multiple transitions takes place wherein the electrons are promoted from: (i) VB to impurity level introduced by iron dopant or CB; (ii) from lower impurity level (introduced by C, N, S dopants) to higher impurity level (iron dopant) or CB (Fig. 22). In addition, surface carbonaceous species acts as a photosensitizer injecting an electron to TiO_2 CB under visible light rendering the dioxygen reduction with subsequent formation of free radicals thereby accelerating RhB degradation [251]. Mesoporous C–N–S–TiO_2 developed by solid phase reaction exhibited 6 times higher daylight induced photocatalytic oxidation of formaldehyde than that of Degussa P25 and undoped TiO_2 [252]. This high activity was ascribed to the synergistic effect of strong UV/visible light absorption and presence of two phase structure of undoped TiO_2 and C–N–S–TiO_2. The two phases of same semiconductor will be beneficial in reducing the recombination rate, where interface between the two phases act as a rapid separation site for the charge carriers due to the difference in the energy level of their CB and VB [252].

The photocatalytic activity of C–N–TiO_2 nanotube/carbon nanorod composite for MO degradation under simulated solar light was attributed to large band gap narrowing via broadening of VB width by mixing 2p orbitals of nitrogen and carbon with O 2p states [253]. In addition, formation of carbon nanorods in TiO_2 facilitates the transportation of photogenerated holes from

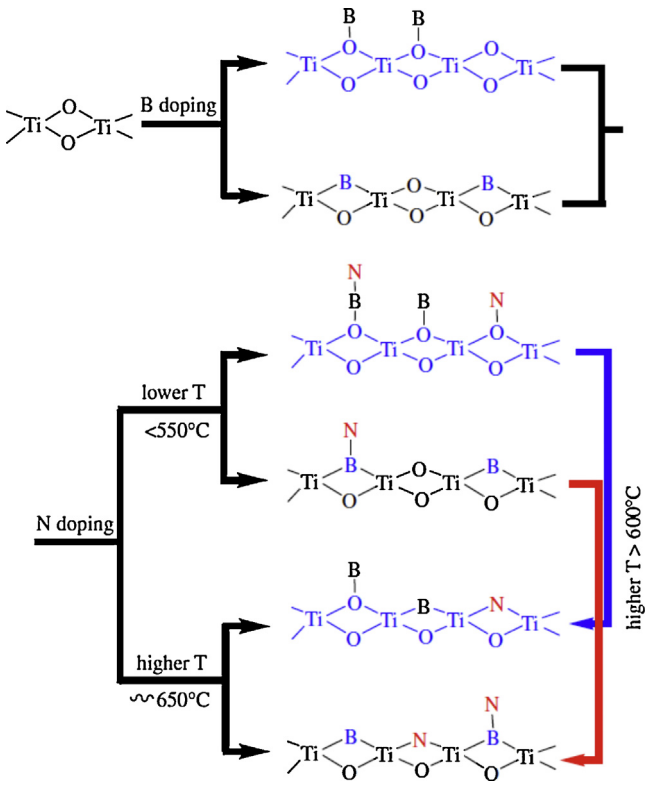

Fig. 21. The transformations of B–N–TiO_2 structure both at lower and higher temperature.
Reprinted with permission from Ref. [249]. Copyright (2011) Elsevier.

TiO_2 surface to electrolyte leading to high photocurrent conversion efficiency.

The enhanced activity of mesoporous Au/S–N–TiO_2 for CO oxidation is attributed to uniform mesoporous structure, large surface area, 3 D connected pore system which favors the adsorption of CO and O_2 [254–256]. XPS spectra revealed that sulphur and nitrogen species were in the form of O–Ti–S, O–Ti–SO_4^{2-} and O–Ti–N linkages and strong metal support interaction rendered the high catalytic activity [254]. Titania nanotubes modified with nitrogen and sulfur by coupling hydrothermal reaction and wet impregnation method using thiourea (1 wt%) as nitrogen and sulphur source respectively showed enhanced activity for the degradation of gaseous isopropanol under visible light compared

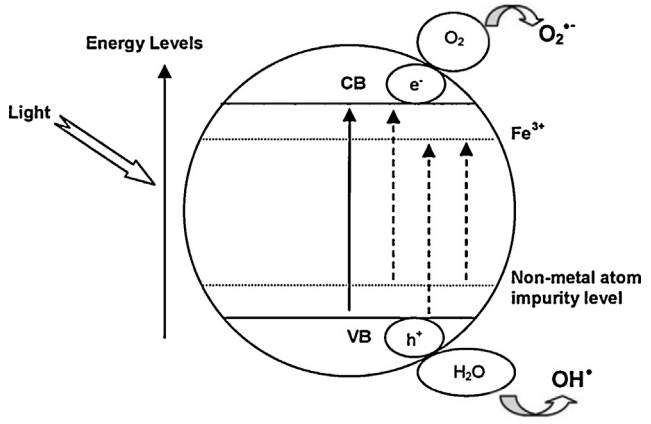

Fig. 22. Schematic diagram of doped-TiO_2 and initial redox process after activation by light.
Reprinted with permission from Ref. [251]. Copyright (2009) Elsevier.

Table 4
The kinetic constants and regression coefficients of atrazine degradation by B-doped TiO_2 nanotube array with 3.1 atom% boron electrode under simulated sunlight irradiation (I_0 = 80 mW/cm^2).

Processes	Kinetic constants (h^{-1})	R^2
Electrochemical	0.0186	0.9073
Photolysis	0.420	0.9955
Photocatalysis	0.705	0.9860
Photoelectrocatalysis	1.08	0.9929

Reprinted with the permission from Ref. [264]. Copyrights (2008) Elsevier.

to unmodified titania nanotubes [257]. This was ascribed to high crystallinity, high specific surface area, reduction of band gap by nitrogen doping and surface modifications (with NH_3 and SO_x species) and its interaction with reactants and products [257].

6. Other non metal doped titania

6.1. Photocatalytic activity of B–TiO_2

The doped boron (amorphous) occupied the interstitials between TiO_2 crystallites improving the microstructure properties and degradation of Orange II under visible light [258]. However, annealing at 700 °C with high boron dopant (0.75 g, 1.0 g and 3.0 g of boron powder) resulted in the crystallization of sassolite (HBO_3) and rutile titania decreasing the photocatalytic activity. B–TiO_2 prepared by both sol–gel method and grinding TiO_2 with boric acid triethyl ester (BATE) showed high activity for phenol oxidation under visible light ascribed to Ti–O–B structure and surface carbon content [259]. In contrast, B–TiO_2 did not reveal better activity under UV light compared to pure TiO_2. B–TiO_2 obtained by surface impregnation method of TiO_2 with 2 wt% BATE and calcined at 400 °C showed high visible light photoactivity for phenol degradation ascribed to the efficient incorporation of boron as B–O–Ti and carbonaceous species like (C–C), (C–C_{arom}) and C–OH on the TiO_2 surface which acts as a sensitizer to induce visible light activated photocatalysis [260]. Meso-macroporous Au/B–TiO_2 (Au = 2 wt%, B = 0.25 wt% calcined at 650 °C) structure prepared via facile agrose gel templating process combined with sol–gel chemistry was significantly active for MB degradation under visible light [261]. The enhancement in activity was due to the sensitization of TiO_2 as a result of surface plasmon excitation by gold nano particles and also it served as an electron sink as demonstrated by the decreased PL intensity implying the inhibition of charge carrier recombination [262,128]. In addition, enhancement is also attributed to the decrease in band gap as a result of boron doping and intimate contact between optimum anatase to rutile ratio (3:1) benefiting the vectorial electron transfer process. In another study, mesoporous Ag/B–TiO_2 structure showed high activity for the degradation of Rhodamine 6G under artificial visible light irradiation compared to B–TiO_2, Ag/TiO_2, TiO_2 and Degussa P25 attributed to the synergistic effect of boron and Ag loading [263]. Under visible light, electrons are excited from mixed energy level of B and O 2p to TiO_2 CB which is subsequently trapped by Ag deposits and transfers to adsorbed O_2 to form superoxide radicals. The presence of Ag effectively restrains the recombination rate of charge carriers by forming Schottky barrier at the interface of TiO_2/Ag composite. B–TiO_2 (B = 3.1 at%) nanotube arrays fabricated by potentiostatic anodization of titanium in an aqueous electrolyte containing fluoride ion and sodium fluroborate ($NaBF_4$) exhibited the best photoelectrochemical and photoelectocatalytic degradation of atrazine under simulated sunlight irradiation in comparison to those mediated only by electrochemical, direct photolysis and photocatalysis (Table 4) [264]. This efficiency was attributed to the function of bias potential which promotes the lifetime of electron hole pairs. B–TiO_2 (B:Ti = 5) prepared by simple sol–gel method showed photocatalytic activity for nicotinamide adenine dinucleotide (NADH) regeneration under UV light irradiation, due to the quantization effect and intense absorption in the UV range [265]. The size quantization resulted in an increase of band gap confining the photogenerated electrons in CB with subsequent increase in their lifetime. The increased band gap energy leads to larger thermodynamic driving force and faster charge carrier transfer rates in the normal Marcus region compared to bulk phase counterparts. The enhancement in UV absorbance accelerates the concentration of photogenerated charge carriers to participate in photocatalytic reactions. Furthermore, water acted as electron donor and ionizes into H^+ and OH^-, which plays a key factor in NADH regeneration [266]. Thus, B–TiO_2 improved the electron supplying capacity of water followed by improving the NADH regeneration rate [267].

6.2. Photocatalytic activity of C–TiO_2

It is generally accepted that carbon doping improves the adsorption of organic pollutant molecules on catalyst surface. Besides, carbon doping can enhance the TiO_2 conductivity as it could facilitate the charge transfer from the bulk to the surface region of TiO_2 structure where the desired oxidation reactions take place [268,269]. The formal oxidation state of carbon dopants ranges from −4 (as carbides with Ti–C bond) to +4 (as carbonates with C–O bond) [270].

C–TiO_2 with rutile structure prepared by flame pyrolysis of Ti metal sheet showed maximum photoconversion efficiency for water splitting at a minimal applied potential of 0.30 V with a photocurrent density of 3.60 mA/cm^2 under 150 W xenon lamp illumination [271]. C–TiO_2 (rutile) nanotube arrays synthesized by anodization of Ti metal sheet at 20 V for 20 h followed by annealing in air at 500 °C for 1 h and natural gas flame oxidation at 820 °C for 18 min produced highest photocurrent density under UV/visible light compared to undoped TiO_2 nanotube film and C–TiO_2 thin film [272]. This enhancement was attributed to increased surface area of nanotube arrays and also to reduced diffusion path length and with simultaneous inhibition of volume carrier recombination [273]. C–TiO_2 prepared by the hydrolysis of $TiCl_4$ with tetrabutylammonium hydroxide calcined at 400 °C for 1 h demonstrated superior photocatalytic activity in the degradation of 4-CP and remazol red under diffuse indoor daylight [274]. Furthermore, C–TiO_2 supported on filter paper was active in the oxidation of gaseous acetaldehyde, benzene and carbon due to the presence of surface states close to VB edge which resulted in the rapid hydroxyl radical formation via oxidation of water or surface hydroxyl groups driven by holes [274]. Mesoporous C–TiO_2 prepared by one pot green synthetic approach using sucrose as new carbon doping source and calcined at 200 °C showed superior photocatalytic degradation of gaseous toluene compared C–TiO_2 calcined at different temperatures (100 °C and 300 °C) under UV/visible light illumination [275]. The superior activity is contributed to the promoted visible light absorbance enabling the sample to utilize more photoenergy taking part in the photocatalytic reaction and generates more charge carriers. The post thermal treatment reduced the electron trapped defect sites and inhibits electron–hole recombination [275]. Mesoporous C–TiO_2 prepared by one pot green synthetic approach using $Ti(SO_4)_2$ and glucose as precursors exhibited efficient photocatalytic activity for gas phase toluene degradation under visible light irradiation with respect to C–TiO_2 prepared from high temperature oxidation of TiC at 450 °C for 2 h [276]. This high activity of the former sample was ascribed to the strong visible light absorption, high surface area and pore volume. The high surface area and pore volume offers more active adsorption sites, enhanced photocatalytic reaction centers and faster flow of gaseous molecules leading to maximum activity [277,278]. C–TiO_2 prepared by a conventional sol–gel synthesis using titanium butoxide as a precursor of both Ti

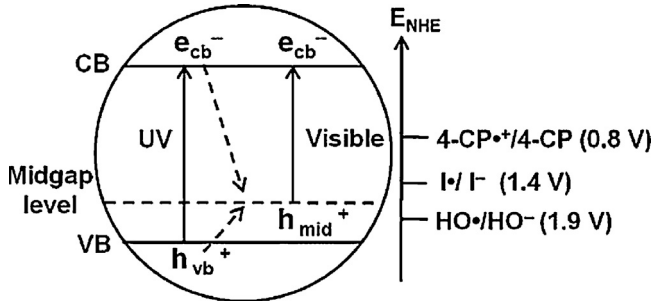

Fig. 23. Photocatalytic degradation of 4-chlorophenol using C–TiO_2 under UV/visible light. The broken line represents carbon induced mid band gap level within the band gap states of titania.
Reprinted with permission from Ref. [279]. Copyright (2009) Elsevier.

and C calcined at 250 °C demonstrated high photocatalytic degradation of 4-CP and photocatalytic oxidation of iodide to triodide under visible light illumination compared to Degussa P25 [279]. The origin of photocatalytic activity was ascribed to the presence of carbon in the lattice and surface carbon species on TiO_2 serving as efficient photosensitizer enabling visible light response. The major oxidants produced during photocatalysis was holes trapped in the midgap state and their oxidation potential seems to be strong enough to directly oxidize [(4CP•/4-CP) = 0.8 V vs NHE], but not to generate hydroxyl radical E ($OH^•/OH^-$) = 1.9 V vs NHE [280–282] (Fig. 23). The photocatalytic oxidation of iodide follows with the reaction of h^+_{mid} with I^- leading to the generation of iodine or triodide [279]:

$$h^+_{mid} + I^- \rightarrow I^• \quad (51)$$

$$I^• + I^- \leftrightarrow I_2^- \quad (52)$$

$$I_2^- + I_2^- \rightarrow I_3^- + I^- \quad (53)$$

$$I_3^- + e^-_{CB} \rightarrow I_2^- + I^- \quad (54)$$

C–TiO_2/V_2O_5 composite prepared by surface loading of C–TiO_2 with 0.05 wt% V_2O_5 through incipient wetness impregnation method exhibited enhanced visible light photocatalytic activity in degradation of gaseous toluene compared to that of SiO_2/V_2O_5 and C–TiO_2 [283]. Under visible light irradiation, charge transfer process includes: (i) photoexcitation of electrons from VB to CB of C–TiO_2; (ii) transition of electrons from CB of C–TiO_2 to CB of V_2O_5; (iii) photoexcitation of electrons from VB to CB of V_2O_5; (iv) hole transfer from VB of V_2O_5 to VB of C–TiO_2 (Fig. 24). Thus, multiple charge transfer pathways leads to separation of excited electron–hole pairs in C–TiO_2/V_2O_5 composite and promotes the activity [283].

6.3. Photocatalytic activity of P–TiO_2

Compared with other elements, phosphorous can significantly increase the specific surface area of TiO_2 and prevent the phase transformation from anatase to rutile, resulting in high photocatalytic activity. The change in surface chemistry by the introduction of phosphorous can be used to engineer the properties of titania for catalytic applications and for organic chemical transformations. P–TiO_2 synthesized by liquid hydrolysis of $TiCl_4$ with NH_3 using H_3PO_4 and calcined at 700 °C showed enhanced activity for the decomposition of MB under visible light irradiation [284]. P–TiO_2 exhibited excellent thermal stability by retaining anatase phase even at high calcination temperature (500–900 °C). The presence of phosphorous species on grain boundary suppressed the particle growth during calcination and also stabilized the anatase phase [285]. Anatase formed during hydrolysis act as crystallization seed

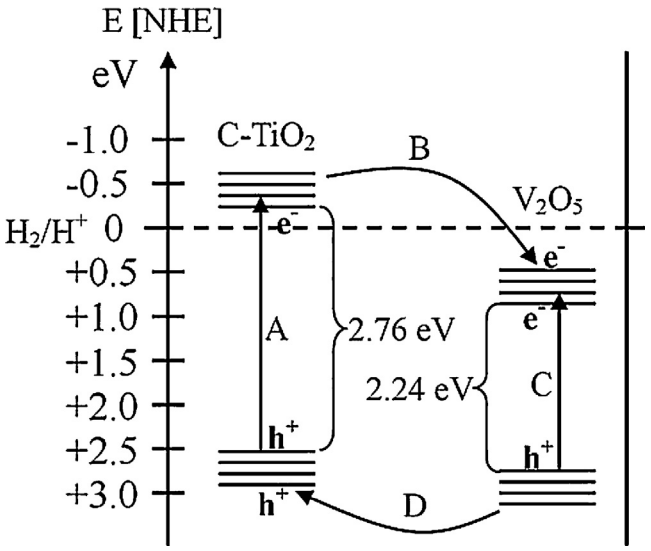

Fig. 24. Electronic band structure of C–TiO_2 loaded with V_2O_5 and charge transfer process under visible light excitation.
Reprinted with permission from Ref. [283]. Copyright (2009) Elsevier.

leading to the transformation of amorphous titania to anatase at lower temperature with high resistance to sintering than the amorphous sample. This may be probable reason for the superior thermal stability of P–TiO_2. Phosphorous content on the surface increased with increase in the calcination temperature leading to enhanced surface acidity favoring the efficient adsorption of cationic dye in spite of very low surface area of P–TiO_2. The degradation mechanism of MB involved the cleavage of C–S^+=C functional groups which is adsorbed on the titania surface by Columbic attraction leading to complete mineralization of pollutant (Fig. 25). Additionally, surface phosphorous species effectively trap the CB electrons preventing the carrier recombination rate [284]. P–TiO_2 synthesized by modified sol–gel method exhibited higher activity for MB degradation under UV/visible light attributed to high surface area, smaller crystallize size, high adsorption capability of MB for P–TiO_2. The charge imbalance induced when P^{5+} substitutes

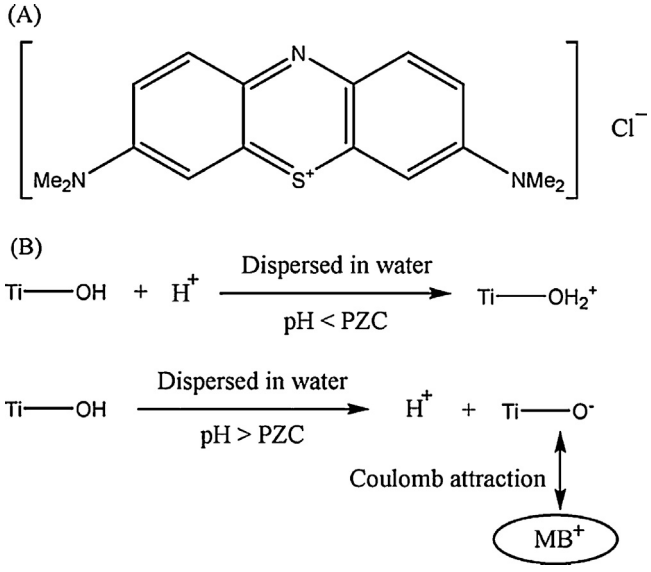

Fig. 25. (A) Molecular structure of methylene blue (MB); (B) schematic representation of MB adsorption on titania by Coulombic attraction.
Reprinted with the permission from Ref. [284]. Copyright (2010) Elsevier.

Table 5
Structural properties and photocatalytic activity of different TiO_2 samples. Surface area of the catalyst is ignored for clarity.

Sample	PO_4 content (wt%)	Crystallite size (nm)	Initial rate (Ms^{-1}) × 10^{-5}	Phenol conversion % (after 120 min)	TC conversion (%)
TiO_2/300 °C	0	7.8	6.4	46.7	38.3
P–TiO_2/0.01/300 °C	1.4	7.3	9.6	71.3	46.5
P–TiO_2/0.05/300 °C	6.1	4.8	3.2	28.3	27.6
P–TiO_2/0.10/300 °C	10.4	Amorphous	2.6	27.6	16.1
P–TiO_2/0.01/500 °C	1.4	11.3	23.6	73.1	46.7
P–TiO_2/0.01/700 °C	1.4	29.0	56.2	92.1	33.1
P–TiO_2/0.01/900 °C	1.4	125.2	7.7	66.3	2.6

Reprinted with the permission from Ref. [293]. Copyright (2006) Elsevier.

Ti^{4+} in the crystal lattice reduces the electron hole recombination that favored efficient photocatalysis [286]. P–TiO_2 synthesized by sol–gel method using H_3PO_4 with "separated phase" showed high activity for MO degradation under visible light compared to P–TiO_2 with "congregated phase" [287]. In the "separated phase" phosphorous species is encapsulated by Ti–O ligands and emerges at microcosmic regions where P/Ti ratio is relatively low and acts as dominating phosphorous species (for phosphorous content < 20%). Because of stronger electrostatic force and smaller ionic radii of phosphorous, "separated phase" introduces oxygen into TiO_2 lattice resulting in visible light response and produces structural defects within the TiO_2 matrix which suppress the crystal growth. All these effects enabled the high activity of P–TiO_2 under visible light. On the other hand "congregated phase" TiO_2 clusters are surrounded by phosphorous species at very high content, which causes higher specific surface area and delays anatase to rutile phase transformation. Furthermore, quantum-size effect brought by "congregated phase" leads to the blue-shift in band gap absorption of anatase. When the calcination temperature increases, phosphorous species in "congregated phase" begins cross-linking and forms new titanyl phosphate at high temperature, such as $Ti_5O_4(PO_4)_4$, $(TiO)_2P_2O_7$ and TiP_2O_7 depending on the ratio of P/Ti in the "congregated phase". Thus, "congregated phase" is sensitive only under UV light. Therefore the ratio between "separated phase" and "congregated phase" in phosphorous species is a pivotal factor in dominating the photoresponse range and photocatalytic activity of P–TiO_2 [287]. Mesoporous P–TiO_2 synthesized by surfactant-templated approach and calcined at 500 °C showed enhanced photocatalytic activity for n-pentane degradation under UV light which is related to its extended band gap energy (3.17 eV) with more powerful redox ability, large surface area (224 m^2/g) that provides more active sites to adsorb water and hydroxyl groups [288]. Meanwhile, Ti ions in tetrahedral co-ordination provides additional surface hydroxyl groups by absorbing water in air and stabilized the photoexcited charge carrier pair [289,290]. The sol–gel preparation of P–TiO_2 showed high ability for NADH regeneration under visible light than pure TiO_2. In this study, phosphorous dopant shifted the absorption edge to the visible region and also served as efficient charge carrier traps [291]. Concretely, electron excited from VB were injected into the surface traps arising from phosphorous doping, which was later captured by $[Cp^*\ Rh\ (bpy)\ (H_2O)]^{2+}$ adsorbed on TiO_2 resulting in $[Cp^*\ Rh\ (bpy)\ (H^+)]^+$. Subsequently, transformation of NAD^+ to NADH was achieved by the oxidation process of $[Cp^*\ Rh\ (bpy)\ H^+]^+$ to $[Cp^*\ Rh\ (bpy)\ (H_2O)]^{2+}$ (Fig. 26) [291]. Phosphate modified TiO_2 prepared by phosphoric acid treatment accelerated the degradation of 4-CP, phenol and RhB despite weak adsorption ability of these pollutants on TiO_2, while much lower degradation rate for dichloroacetic acid, alizarin red and catechol (with strong adsorption on TiO_2) was observed under UV light [292]. The accelerated photocatalytic activity was attributed to phosphate modification which markedly shifts the point of zero zeta potential of TiO_2 to lower pH value. Thus, accumulation of negative charges on the surface creates negative electrostatic field promoting the separation of electrons and holes by drawing the photoinduced hole to the surface. In addition, phosphate ions interacted with H_2O through hydrogen bond accomplishing efficient electron transfer between TiO_2 and chromophore. Although adsorption of dichloroacetic acid, alizarin red and catechol was effective on catalyst surface, its degradation rate was rather low due to the inhibition of direct hole oxidation of substrates than that of hydroxyl radical attack [292]. Thermally stable P–TiO_2 prepared by sol–gel synthesis without addition of surfactants calcined at 300 °C and 500 °C with P/Ti ratio = 0.01% showed enhanced photocatalytic degradation of phenol compared to unmodified TiO_2 and P–TiO_2 calcined at 700 °C and 900 °C (Table 5) [293]. The enhanced activity is assigned to increase in the specific surface area without chemically blocking the TiO_2 surface and to the formation of active sites on TiO_2 surface. In addition, presence of moderate amount of titanium phosphate enhanced the photoinduced charge separation resulting in more hydroxyl radicals, thereby increasing the phenol degradation rate, where as higher content of phosphate decreased the phenol degradation because of complete coverage of titanium phosphate on TiO_2 surface [293].

6.4. Photocatalytic activity of S–TiO_2

The doping of sulphur at oxygen sites could significantly modify the electronic structures of TiO_2, because sulphur has larger ionic radius compared to nitrogen and fluorine. S–TiO_2 porous layers grown by micro arc oxidation process under pulse current exhibited better performance in the degradation of MB under visible light irradiation compared to the layers synthesized under direct current. The improved photocatalytic behavior is due to the fine pore size, high surface area and anatase phase structure [294]. Simultaneous doping of sulphur into TiO_2 bulk and surface sulfate species (SST) prepared through low temperature solvothermal method using $K_2S_2O_8$ as sulphur source (0.5 M ratio of $K_2S_2O_8$ to Ti) performed well for phenol degradation under visible light compared to TiO_2, N–TiO_2 and C–TiO_2 (Fig. 27). The synergistic effect

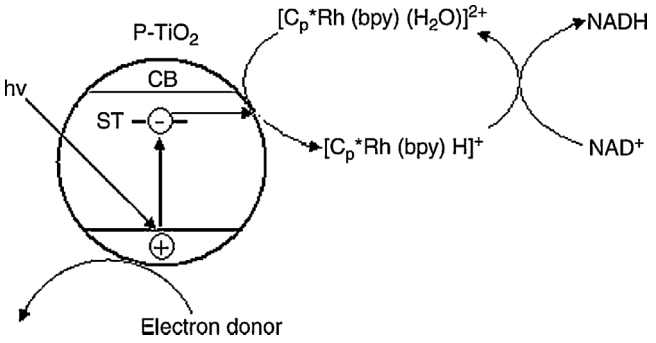

Fig. 26. Cartoon illustrating the electron transfer pathway in the photoregeneration system of NADH with P-doped TiO_2 as the photocatalyst and $[Cp^*Rh(bpy)(H2O)]^{2+}$ as the electron mediator, in which CB, VB and ST are the abbreviations of conduction band, valence band and surface trap, respectively.
Reprinted with the permission from Ref. [291]. Copyright (2006) Elsevier.

Table 6
Sulphur content, Crystal size and visible light photocatalytic activity of S–TiO_2 reprinted with the permission from W. Ho, J.C. Yu, S. Lee, J. Solid State Chem. 179 (2006) 1171–1176. Copyright (2006) Elsevier.

S doped TiO_2 prepared from[a]	Sulphur content (atom%)[b]	Crystal size (nm)[c]	% 4-Chlorophenol degraded[d]
0.1 M TiS_2	1.5	6.5	51
0.5 M TiS_2	2.5	7.5	71
1 M TiS_2	2.8	7.9	86
2 M TiS_2	3.8	8.2	88

[a] Initial concentration used in the hydrothermal process.
[b] Measured by XPS.
[c] Determined by the Scherrer equation.
[d] Measured after 6 h of visible light irradiation.

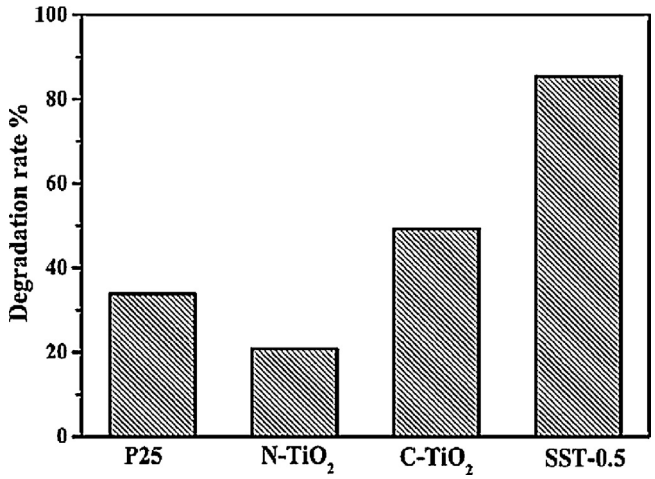

Fig. 27. The degradation of phenol under visible light using various photocatalysts. Reprinted with the permission from Ref. [295]. Copyright (2012) Elsevier.

of S^{4+} dopant to induce visible light response and anchored sulphate group acting as reactive electron trapping site contributes to high activity (Fig. 28). Under visible light irradiation, electrons are injected from O 2p to impurity energy level (S^{4+}) and in turn detrap to O_2. Both CB electron and VB hole produces hydroxyl radicals [295]:

$$SST + h\nu \rightarrow SST + e^- + h^+ \quad (55)$$

$$OH^- + h^+ \rightarrow OH^{\cdot} \quad (56)$$

$$O_2 + e^- \rightarrow O_2^{\bullet -} \quad (57)$$

$$O_2^{\bullet -} + H^+ \rightarrow HO_2^{\bullet} \quad (58)$$

$$2HO_2^{\cdot} \rightarrow H_2O_2 + O_2 \quad (59)$$

$$H_2O_2 + e^- \rightarrow OH^{\bullet} + OH^- \quad (60)$$

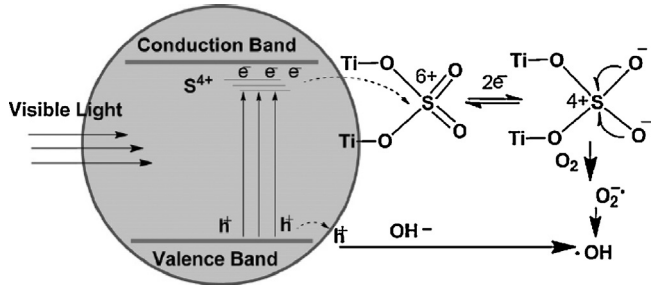

Fig. 28. The process of charge transfer for degradation of phenol. Reprinted with the permission from Ref. [295]. Copyright (2012) Elsevier.

S–TiO_2 (S = 3.8 at%) developed from one step low temperature hydrothermal route from 2 M TiS_2 (Both TiO_2 and sulphur source) and HCl was active for 4-CP degradation under visible light compared to other catalyst prepared with different concentration of TiS_2 (0.1–1 M) (Table 6) [296]. S–TiO_2 exhibited strong visible light induced antibacterial effect for *Micrococcus lylae* bacterium compared to TiO_2 and the involvement of hydroxyl radicals for bacteria inactivation was confirmed by ESR measurements [297]. S–TiO_2 prepared by the reaction of titanium butoxide and thiourea in methanol and calcined at 500 °C showed activity for the 4-CP photodecomposition under visible light irradiation [298]. XRD patterns showed stabilization of anatase crystalline structure up to 700 °C, as sulphate groups (from decomposition of thiourea) anchored on TiO_2 delayed the anatase to rutile transformation [299]. CdS/S–TiO_2 showed enhanced activity for the degradation of MO under visible light attributed to the synergetic effect of S^{6+} doping and CdS modification [300]. S^{6+} doping narrowed the band gap to facilitate the visible light response and decreased the standard reduction potential of CB to enhance the electron transfer from CdS to TiO_2 [301–303]. Upon visible light irradiation, more charge carriers and active radicals are generated on CdS/S–TiO_2 which enhances the activity. S–TiO_2 nanotube loaded with Fe_2O_3 improved the activity for gaseous acetaldehyde oxidation under UV/visible light [304]. The reaction rates enhancement was strongly dependent on the site of Fe_2O_3 nanoparticles loaded on S–TiO_2 nanotube. Under UV light irradiation (λ = 350 nm), Fe_2O_3 loaded inside the S–TiO_2 surface (FSI) showed the highest level of photocatalytic activity compared to Fe_2O_3 loaded outside the S–TiO_2 surface (FSO) and Fe_2O_3 loaded on both the sides (FSIO). In contrast, FSO showed highest activity compared to FSI and FSIO under visible light. The photo excited electrons in Fe_2O_3 loaded on S–TiO_2 transfers to CB of S–TiO_2 and holes in Fe_2O_3 oxidize the acetaldehyde (Fig. 29) [304]. S–TiO_2 with mixed anatase and rutile crystal structure prepared by calcining the mixture of $TiCl_3$ and NH_4SCN solutions exhibited high activity for MB and gaseous acetaldehyde degradation in presence of oxygen under visible light compared to S–TiO_2 with only anatase phase [305]. XPS spectra of S–TiO_2 showed that sulfur atoms existed on the surface of TiO_2 powders and disappeared after Ar^+ etching, indicating that sulphur was not doped into the bulk of TiO_2 [305]. S–TiO_2 prepared by hydrothermal route at 180 °C exhibited the best photocatalytic activity for the decomposition of MO under UV irradiation, ascribed to its particle size (30 nm), spherical morphology, anatase-rutile mixed crystal with high photonic efficiency [306]. S–TiO_2 (S = 1.8%) prepared by treating TiO_2 precursor (xerogel) under supercritical conditions in CS_2/ethanol fluid (SCT) showed high activity for MB degradation under visible light compared to S–TiO_2 prepared by direct calcination (DCT), undoped TiO_2 and N–TiO_2 (N = 1.7%) [307]. This enhanced activity shows the promoting effect of supercritical treatment attributed to high surface area and large porous channels in SCT was favorable for diffusion and adsorption of MB molecules. Further, high crystallization degree of anatase in SCT facilitates the transfer of photoelectrons from bulk to surface resulting in high quantum efficiency [307].

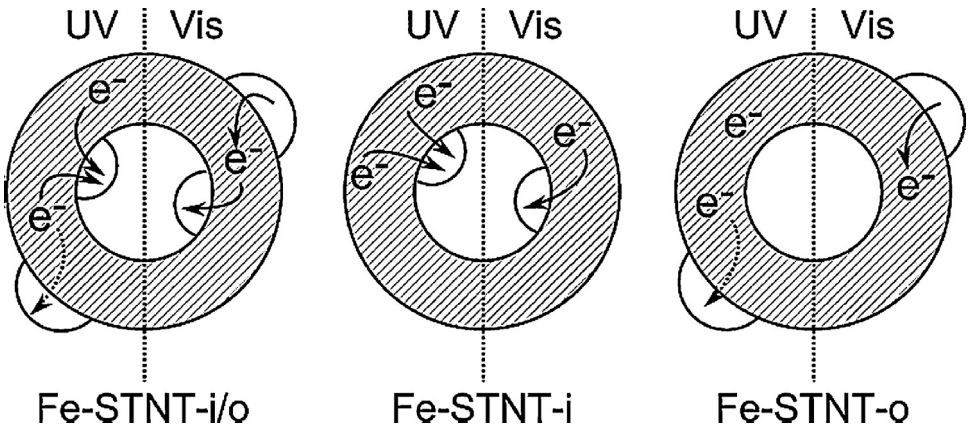

Fig. 29. Mechanism of trapping of the photoexcited electrons by Fe_2O_3 loaded on S doped TNT under UV light irradiation or under visible light irradiation. Reprinted with the permission from Ref. [304]. Copyright (2008) Elsevier.

Moreover, sulphur modification generates more oxygen vacancies and/or defects which capture photoinduced electrons and holes [308,309]. XPS spectra revealed that the electrons were transferred from sulphur to oxygen in SCT making sulphur electron deficient or sulphur to act as reactive electron trapping site [307]. Cu–S–TiO_2 showed high degradation rate for MO under UV/visible light due to the increased light absorption, small grain size of catalyst, large enhanced specific surface area, and presence of Cu^{2+}, Cu^{+}, and O_2 as electron acceptors [310]. The reduction potentials of Cu^{2+}/Cu^0 and Cu^{+}/Cu^0 are 0.17 V and 0.52 V respectively. Thus, it is thermodynamically feasible for Cu^{2+} and Cu^{+} to behave as electron traps since they have more positive reduction potentials than the CB edge of TiO_2 (−0.2 V).

$$TiO_2 \xrightarrow{h\nu} e^- + h^+ \quad (61)$$

$$Cu^+ + e^- \rightarrow Cu^0 \quad (62)$$

$$H_2O + h^+ \rightarrow OH^{\cdot} \quad (63)$$

$$O_2 + e^-(Cu^+ \text{ or } Cu^0) \rightarrow O_2^{\bullet -} \quad (64)$$

$$OH^{\cdot} + R \rightarrow CO_2 + H_2O \quad (65)$$

The longer wavelength response, existence of surface acidic sites and large surface area of Bi–S–TiO_2 prepared by sol–gel method resulted in faster degradation of IC under visible light [311]. The surface acidity is ascribed to doped sulphur existing as sulphate ions which facilitates the high concentration of pollutants to get adsorbed on TiO_2 surface. S–TiO_2 and F–TiO_2 was prepared by sol–gel method using thiourea and NH_4F respectively as dopant source [312]. Both undoped and S–TiO_2 showed similar photocatalytic activity for formic acid degradation due to the inefficient insertion of sulphur into TiO_2 crystal structure characterized by its large ionic radius. Contrarily, F–TiO_2 exhibited superior activity for formic acid decomposition mainly ascribed to highly crystalline and low defective structure which results in reduced charge carrier recombination. In addition, presence of Ti^{3+} species, NO trapped in micro voids that was induced during synthesis by precursor and single nitrogen atom trapped in the bulk of TiO_2 were responsible for longer wavelength absorption [312].

6.5. Photocatalytic activity of F–TiO_2

Highly crystalline flower like F–TiO_2 nanostructure exhibited high photoelectrochemical activity for water splitting and 4-NP degradation compared to Degussa P25 under UV/visible light illumination [313]. The photoelectrocatalytic activity exhibited increased photocurrent intensity with increase in applied electrode potential suggesting reduced charge carrier recombination [314,315]. F–TiO_2 synthesized by spray pyrolysis (SP) method from aqueous solution of H_2TiF_6 at 1173 K demonstrated the highest photocatalytic activity for the decomposition of gas phase acetaldehyde under UV/visible light illumination compared to Degussa P25 [316]. This was attributed: (i) fluorine doping leads to the enhancements of surface acidity, increasing the adsorptivity for reactant molecules on catalyst surface; (ii) doped fluorine atoms promoted the formation of oxygen vacancies like F and F^+ center which were responsible for the appearance of visible light photocatalytic activity and provided sites for the formation of active species (superoxide and hydroxyl radicals). Moreover, doped fluorine atoms increased the photogenerated electron mobility from the inner region to the surface and initiates redox reactions [316]. The high activity of hierarchical porous F–TiO_2 structure for 4-CP degradation was due to the excitation of extrinsic absorption bands by oxygen vacancies rather than the excitation of intrinsic absorption band of bulk TiO_2 [317]. In addition hierarchical porous F–TiO_2 structure allows more efficient transport for reactant molecules to reach the active sites on the framework walls, thus enhancing the efficiency of photocatalysis [318–320]. F–TiO_2 prepared by sol–gel route using CF_3COOH and tetraethyl orthotitatanate as precursors followed by calcination at 400 °C exhibited higher activity for acetone decomposition under UV–vis illumination attributed to suitable mixed anatase–rutile phase composition (A = 72.5 wt% and R = 27.4 wt%) and high surface area (48.48 m^2/g) [321]. In addition, crystallization of rutile alone or along with anatase phase at low temperature is attributed to the acidic character of fluorine precursor which provides low pH conditions during peptization. At these acidic conditions, edge shared bonding among the TiO_6 octahedrons responsible for anatase formation is suppressed, while the corner-shared bonding responsible for rutile nucleation is favored during calcination [321]. F–TiO_2 nanotubes prepared by impregnation method and calcined at 300 °C showed superior photocatalytic activity for MO degradation in comparison to TiO_2 nanotubes ascribed to the synergistic effect of both oxygen vacancy and Ti^{3+} states [322]. The formation of superoxide radical from chemisorbed oxygen or hydroxyl radicals from adsorbed water requires presence of surface oxygen vacancy. These oxygen vacancy leads to the formation of new active sites for hydroxyl radical generation. In addition, Ti^{3+} surface states capture the CB electrons and transfer them to adsorbed O_2 to reduce recombination [323,324].

6.6. Photocatalytic activity of I–TiO_2

The use of iodine-doped TiO_2 (I–TiO_2) to conserve solar energy efficiently has triggered a new area of research. From the view point of radius matching, it is possible for I^{5+} to replace Ti^{4+} or iodine can be in the form of I^{7+} and I^- via disproportionation of IO_3^-. I–TiO_2 not only alters the surface charge and bulk band gap of TiO_2, but also act as a CB electron scavenger capable of inhibiting the rapid recombination of electron–hole pairs [325]. The first principle calculations indicated that I 5p and/or I 5s orbitals mixing with O 2p and Ti 3d orbitals were responsible for visible light response. Besides, it was reported that I–TiO_2 films showed good IPCE for dye sensitized solar cells under simulated sunlight [326]. In line with the above remarkable features, I–TiO_2 can be of great promise in the area of heterogeneous photocatalysis.

The enhancement in photocatalytic activity of I–TiO_2 for phenol decomposition under UV/visible light was due to the generation of Ti^{3+} surface states/cation vacancies and low degree of charge carrier recombination. In addition, anatase phase with small crystal size (~5 nm) requires less time for the photogenerated carriers to diffuse from the inner region to the photocatalyst surface thereby accelerating the charge carrier separation [327]. Mesoporous I–TiO_2 with bicrystalline (57% anatase and 43% rutile) framework synthesized by a two step template hydrothermal synthesis route showed positive result for MB photodegradation under UV/visible light compared to I–TiO_2 (anatase), which is mainly attributed to its mixed crystalline framework, high crystallinity, large surface area, mesoporous structure and high absorbance in the visible light range [328]. The anatase–rutile interfacial polymorph structure would contain a surplus amount of tetrahedral Ti^{4+} sites which can act as reactive electron-trapping sites. These isolated tetrahedral Ti^{4+} sites are more active than octahedrally coordinated Ti^{4+} sites as in bulk TiO_2, and serve as catalytic hot spots at the interface of anatase/rutile heterojunction and thus avail the mixed polymorph nanocrystals into an effective photocatalytic relay for efficient solar energy conversion [329–332]. The electron and hole pairs generated in rutile titania with small particle size possessed much stronger redox ability than bulk rutile titania resulting in efficient photocatalysis. Furthermore, energetic electrons in the CB of rutile TiO_2 effectively transferred into lattice trapping sites of anatase resulting in low recombination rate. The disordered mesoporous structure was beneficial in promoting the diffusion of reactants and products to the reactive sites on the photocatalyst surface [328]. I–TiO_2 nanospheres synthesized via two step hydrothermal route showed high photocatalytic efficiency for MO decoloration under visible light compared to I–TiO_2 powder, which was attributed to better crystallization and bimodal porous nanosphere structure. The interaggregated pores increased the light harvesting efficiency by multiple scattering within the porous fragment and provided more efficient transport channels for reactant molecules to approach the reactive sites on the framework walls of small mesopores [333]. I–TiO_2 with surface dominant I–O–I and I–O–Ti structures demonstrated better photocatalytic activity for RhB degradation under UV/visible light (Fig. 30). The enhanced performance was attributed to lower energy photon excitation pathways from the occupied states of I–O–Ti structure (located above VB) to unoccupied states of I–O–I structure (situated below CB) which results in the extended light absorption edge upto 800 nm. Furthermore, occupied states very close to VB give rise to strong oxidative power of generated holes, which together with favorable surface structure for surface transfer of carriers contributes to efficient photoactivity [334]. Multivalent I–TiO_2 prepared via combination of deposition–precipitation process and hydrothermal treatment exhibited enhanced degradation rate of gaseous acetone under visible light [335]. The experimental and theoretical calculations proposed a sub band gap transition mechanism in which iodine incorporation creates IO_4^-/I^- species. The redox potential E^0 (I^{7-}/I^-) = 1.24 V lies between the E_{CB} (TiO_2) = −0.5 V and E_{VB} (TiO_2) = 2.7 V (vs. NHE), favoring the thermodynamic electron promotion from TiO_2VB to surface iodine species (Fig. 31). The holes left on VB oxidize the hydroxyl ions to give hydroxyl radicals resulting in faster degradation of organic pollutants. Alternatively, IO_4^- can trap electron and get reduced to I^- lowering the oxidation state of iodine from +7 to −1 [335]. Under UV/visible light irradiation, I–TiO_2 prepared via hydrothermal treatment demonstrated high photocatalytic activity for 4-CP degradation than commercial ST01. It was suggested that iodine induced continuous states mixed with the VB of TiO_2 facilitating hole trap to produce more hydroxyl radicals (Fig. 32) [336].

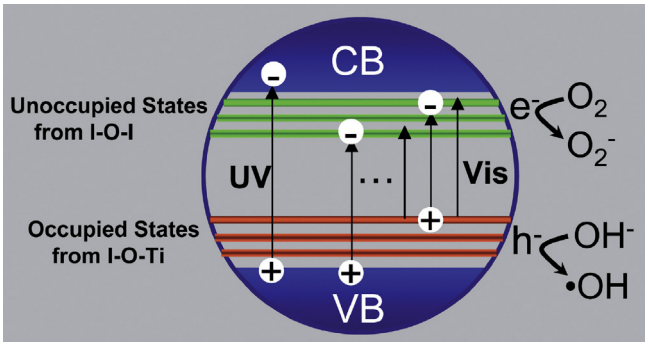

Fig. 30. The mechanism of photon excitation via different pathways under UV/visible light irradiation with subsequent surface reactions of photoexcited electrons and holes in I–TiO_2 with I–O–I and I–O–Ti surface structure.

Reprinted with permission from Ref. [334]. Copyright (2009) Royal Society of Chemistry.

The doping of iodine with concentration of 0.20 wt% and 0.32 wt% showed high activity under UV and visible light respectively for the degradation of Orange II dye [337]. The degradation mechanism for Acid Orange 7, MO and 2,4-DCP under visible light with I–TiO_2 was due to indirect oxidation of pollutants by hydroxyl radicals, as evidenced by decline in degradation rate with ethanol [338]. Ag–I–TiO_2 with 3% Ag content exhibited more efficient p-chlorophenol degradation under visible light compared to their single doped counterparts [339]. The cooperative effect of iodine doping in shifting the band gap absorption to visible light region and ability of Ag^+ to trap electron and detraps the same for dioxygen reduction favors efficient photocatalysis [339]. La–I–TiO_2 with

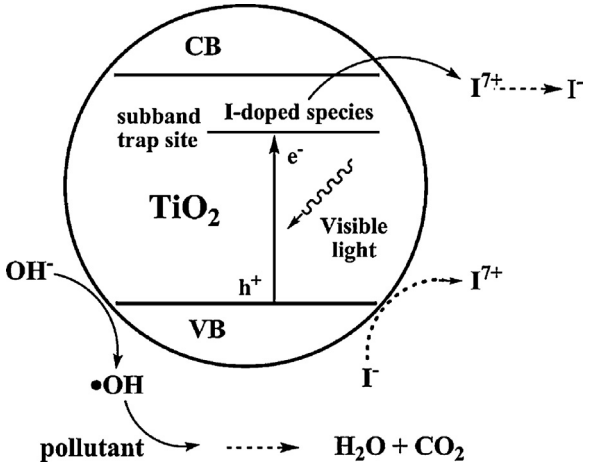

Fig. 31. Photocatalytic mechanism of I–TiO_2 under visible light, showing the electron trap by I^{7+} and hole trap by I^-.

Reprinted with permission from Ref. [335]. Copyright (2008) American Chemical Society.

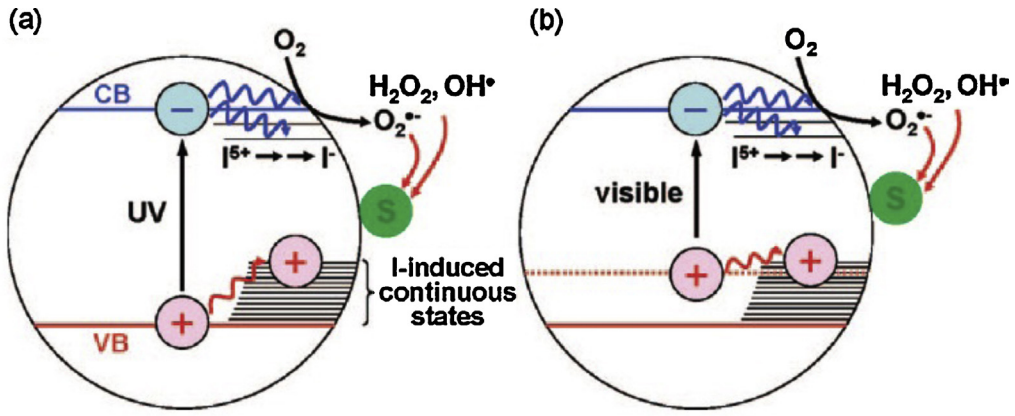

Fig. 32. Charge transfer process of I–TiO_2 under (a) UV (b) visible light. S refers to the substrate.
Reprinted with permission from Ref. [336]. Copyright (2008) American Chemical Society.

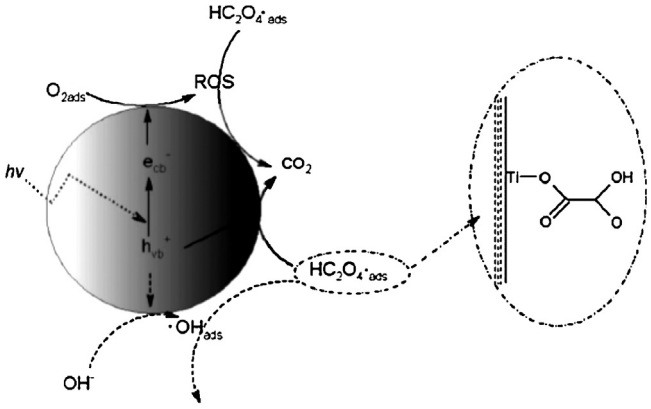

Fig. 33. Surface complexation and degradation of oxalic acid using La–I–TiO_2 under visible light.
Reprinted with the permission from Ref. [340]. Copyright (2008) American Chemical Society.

molar ratio of 20:20:100 and calcined at 400 °C exhibited remarkable photocatalytic degradation of oxalic acid under visible light irradiation [340]. The dopant La was uniformly dispersed on the TiO_2 surface as La_2O_3 deposits efficiently inhibited the recombination. In addition, photocatalytic degradation of oxalic acid was inhibited in presence of KI and was not affected with tertiary butyl alcohol indicating the dominant role of VB hole and surface adsorbed hydroxyl radicals in the degradation mechanism of oxalic acid (Fig. 33). Ga–I–TiO_2 with 0.5% Ga^{3+} exhibited more efficient photocatalytic activity in the degradation of 2-CP under visible and UV–vis light compared to I–TiO_2 [341]. The beneficial role of Ga^{3+} was observed in the retardation of anatase- rutile phase transformation, extending the band gap absorption to longer wavelength and creation of oxygen vacancy for charge compensation [342]. These oxygen vacancy defects act as electron traps and effectively enhance the lifetime of holes which facilitates pollutant degradation [343]. Zr–I–TiO_2 exhibited high activity in MO decolorization under visible light compared to I–TiO_2 [344]. This superior activity of Zr–I–TiO_2 originates from its smaller crystal size (5.5 nm) and larger surface area, providing more surface active sites for photocatalysis reactions to occur. Furthermore, effective electron trapping by Zr^{4+} ions and the presence of I^{7+} and I^- species responsible for red shift in the band gap absorption synergistically contributed to overall efficiency [344]. Pt/I–TiO_2 showed superior activity compared to I–TiO_2 for phenol transformation under visible light as platinum modification enhanced the electron hole separation [345]. However, photomineralization was not improved due to the presence of tautomeric equilibrium between quinone and hydroquinone (Fig. 34). Phenol photodegradation was preferentially initiated by the formation of Ti–OH–Ph structure, which was attacked by VB hole to directly generate quinone and this keto-enol tautomeric equilibrium retards the photomineralization process [345]. I–TiO_2 film electrode with mesoporous nanocrystalline framework fabricated via doctor blade method showed highest photoelectrocatalytic (PEC) and photocatalytic efficiency for the degradation of RhB and 1-naphthol under visible light irradiation compared to undoped TiO_2 [346]. The enhanced performance was explained by improved visible light response, formation of

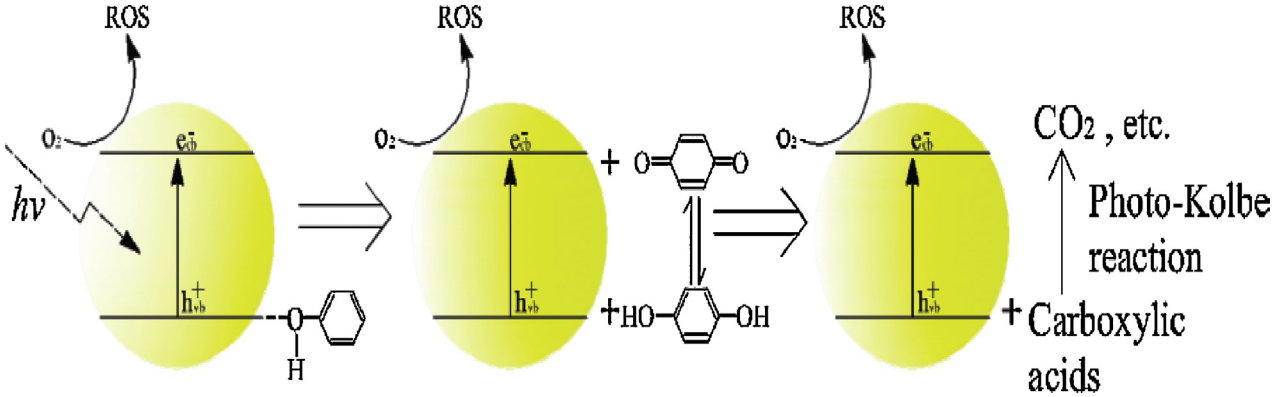

Fig. 34. Representation of tautomeric equilibrium between quinone and hydroquinone during Photomineralization of phenol using I–TiO_2.
Reprinted with permission from Ref. [345]. Copyright (2010) American Chemical Society.

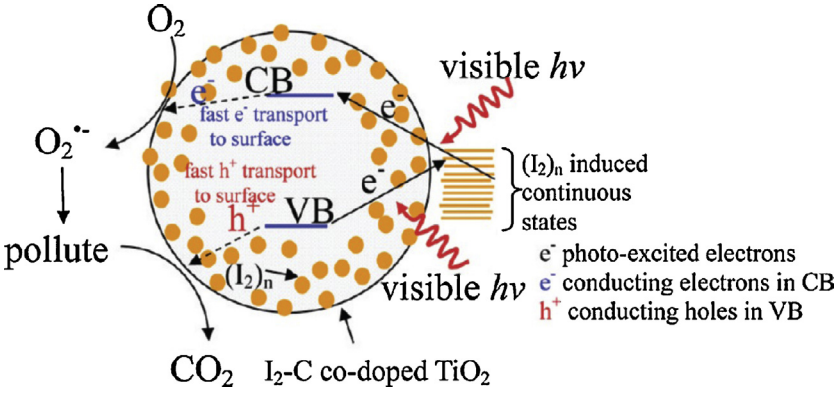

Fig. 35. Visible light driven mechanism of I_2–C–TiO_2 nanoparticle.
Reprinted with permission from Ref. [349]. Copyright 2010, American Chemical Society.

iodine states below CB, relatively large surface area (245.6 m^2/g) with mesoporous structure providing more adsorptive active sites and intensifying the mass transport process [347,348]. In addition, synergistic effect between applied potential and light irradiation contributed to high activity.

Bimodal meso/nanoporous I_2–C-codoped TiO_2 synthesized through a template-free process and calcined at 400 °C exhibited high activity for MB degradation under visible light compared to C–TiO_2 and Degussa P25 [349]. The iodine doping induced continuous states which can accept visible light excited electrons from TiO_2 VB or provide the electrons from I_2 induced state to TiO_2 CB. The induced defect state concentrated in the surface region facilitates the trapping of charge carriers (Fig. 35). The carbon doping enhances the conductivity of TiO_2 so that the photoinduced carriers can rapidly transfer to the surface region and participate in desired oxidation reactions. The highly crystalline anatase promotes the electron transfer from bulk to surface and inhibits bulk recombination of charge carriers. B–I–TiO_2 prepared by hydrolyzation–precipitation method and calcined at 400 °C for 3 h showed promising activity for MO degradation under visible light due to its smaller particle size as a result of codoping boron and iodine [350]. Since the doping of B^{3+} in TiO_2 lattice was electron deficient, it served as a shallow trap for electrons prolonging the lifetime of photoinduced electrons and holes [351]. Meanwhile, multivalent iodine (I^{7+}, I^- and I^{5+}) at the surface forms a space charge layer which further separates the charge carrier to a larger extent.

7. Conclusion

Anatase TiO_2 is universally recognized as the standard photocatalyst as it has good light harvesting capacity, high adsorption ability for pollutant molecules and high density of surface hydroxyl groups that are vital and crucial to drive photocatalytic reactions. The fatal drawback of charge carrier recombination and large band gap is overcome by the doping of foreign ions into TiO_2 matrix and significant advancement is achieved over the years. However, complexities involved in metal ion doping into titania are thermal instability, dopant insolubility, formation of secondary phase or surface aggregation rather than substitution, phase transformation among the titania polymorphs, metal ion serving as recombination centers, dopant electronic configuration, alteration of charge carrier diffusion length, narrow band bending etc., implicates quite confusing results and therefore choice of effective dopant still remains questionable. It is accepted that doping with non metal ions into TiO_2 either at Ti^{4+} or O^{2-} lattice sites provides favorable surface-electronic structure, modulates the band gap energy for visible light response and facilitates efficient charge carrier transfer process. Accordingly, this review provides a comprehensive research focused on fundamental issues in the degradation of organic pollutants using non metal doped TiO_2 under light illumination. In addition, correlation of variable parameters like preparative techniques, crystallographic structure (anatase, rutile, mixed phase of anatase–rutile and anatase–brookite), crystallite size, surface area, acid–base properties, surface states, surface morphology, nature of dopant substitution, band gap energy, trap states, intrinsic and induced defects (oxygen vacancies and Ti^{3+} states) on the photocatalytic performance is discussed, besides outlining the degradation mechanism of few pollutants. Further improvement in the activity of non metal doped titania achieved by co-doping with foreign ions, deposition with noble metals, sensitization with inorganic complexes/dyes and surface modification with anions (sulphate and phosphate) is highlighted. The mechanism for efficient photocatalysis is discussed in the light of charge carrier generation, trapping, detrapping, interfacial and recombination pathways.

Acknowledgements

The authors would like to acknowledge University Grants Commission (UGC) and Department of Science and Technology (DST-SERC & IDP), Government of India for Financial Assistance.

References

[1] J. Yu, X. Yu, Environmental Science & Technology 42 (2008) 4902–4907 (and references cited therein).
[2] G.K. Prasad, P.V.R.K. Ramacharyulu, B. Singh, K. Batra, A.R. Srivatsava, K. Ganesan, R. Vijayaraghavan, Journal of Molecular Catalysis A: Chemical 349 (2011) 55–62.
[3] J. Yu, J. Xiong, B. Cheng, Y. Yu, J. Wang, Journal of Solid State Chemistry 178 (2005) 1968–1972.
[4] X. Zhu, J. Zhang, F. Chen, Chemosphere 78 (2010) 1350–1355.
[5] L. Guo, F. Chen, X. Fan, W. Cai, J. Zhang, Applied Catalysis B: Environmental 96 (2010) 162–168.
[6] J. Yu, X. Yu, B. Huang, X. Zhang, Y. Dai, Crystal Growth & Design 9 (2009) 1474–1480.
[7] A.G.S. Prdo, L.B. Bolzon, C.P. Pedroso, A.O. Moura, L.L. Costa, Applied Catalysis B: Environmental 82 (2008) 219–224.
[8] P. Ctibor, H. Ageorges, V. Stengl, N. Murafa, I. Pis, T. Zahoranova, V. Nehasil, Z. Pala, Ceramics International 37 (2011) 2561–2567.
[9] P. Wang, C. Fan, Y. Wang, G. Ding, P. Yuan, Materials Research Bulletin 48 (2013) 869–877.
[10] S. Ahuja, T.R.N. Kutty, Journal of Photochemistry and Photobiology A: Chemistry 97 (1996) 99–107.
[11] H. Fu, J. Lin, L. Zhang, Y. Zhu, Applied Catalysis A: General 306 (2006) 58–67.
[12] A. Ishikawa, T. Takata, J.N. Kondo, M. Hara, H. Kobayashi, K. Domen, Journal of the American Chemical Society 124 (2002) 13547–13553.
[13] J. Yu, J. Zhang, S. Liu, Journal of Physical Chemistry C 114 (2010) 13642–13649.
[14] X.F. Cheng, W.H. Leng, D.P. Liu, J.Q. Zhang, C.N. Cao, Chemosphere 68 (2007) 1976–1984.

[15] (a) G. Dai, J. Yu, G. Liu, Journal of Physical Chemistry C 116 (2012) 15519–15524;
(b) G. Liu, P. Niu, L. Yin, H.M. Cheng, Journal of the American Chemical Society 134 (2012) 9070–9073.
[16] A. Fujishima, K. Honda, Nature 238 (1972) 37–38.
[17] S. Liu, J. Yu, M. Jaroniec, Chemistry of Materials 23 (2011) 4085–4093.
[18] A. Kubacka, M.F. Garcia, G. Colon, Chemical Reviews 112 (2012) 1555–1614.
[19] S. Liu, J. Yu, B. Cheng, M. Jaroniec, Advances in Colloid and Interface Science 173 (2012) 35–53.
[20] M.A. Henderson, Surface Science Reports 66 (2011) 185–297.
[21] A.R. Khataee, M.B. Kasiri, Journal of Molecular Catalysis A: Chemical 328 (2010) 8–26.
[22] (a) G. Palmisano, V. Augugliaro, M. Pagliaro, L. Palmisano, Chemical Communications 33 (2007) 3425–3437;
(b) T. Berger, D.M. Satoca, M. Jankulovska, T.L. Villarreal, R. Gomez, ChemPhysChem 13 (2012) 2824–2875.
[23] G. Liu, L. Wang, H.G. Yang, H.M. Cheng, G.Q. Lu, Journal of Materials Chemistry 20 (2010) 831–843.
[24] A. Hangfeldt, M. Gratzel, Chemical Reviews 95 (1995) 49–68.
[25] P.V. Kamat, Chemical Reviews 93 (1993) 267–300.
[26] O. Legrini, E. Oliveros, A.M. Braun, Chemical Reviews 93 (1993) 671–698.
[27] A.L. Linsebigler, G. Lu, J.T. Yates, Chemical Reviews 95 (1995) 735–758.
[28] M.R. Hoffmann, S.T. Martin, W. Choi, D.W. Bahnemann, Chemical Reviews 95 (1995) 69–96.
[29] K. Lv, B. Cheng, J. Yu, G. Liu, Physical Chemistry Chemical Physics 14 (2012) 5349–5362.
[30] M.A. Fox, M.T. Dulay, Chemical Reviews 93 (1993) 341–357.
[31] X.X. Chen, S.S. Mao, Chemical Reviews 107 (2007) 2891–2959.
[32] A. Fujishima, T.N. Rao, D.A. Tryk, Journal of Photochemistry and Photobiology C: Photochemistry Reviews 1 (2000) 1–21.
[33] A. Mills, S.L. Hunte, Journal of Photochemistry and Photobiology A: Chemistry 108 (1997) 1–35.
[34] O. Carp, C.L. Huisman, A. Reller, Progress in Solid State Chemistry 32 (2004) 33–177.
[35] D. Chatterjee, S. Dasgupta, Journal of Photochemistry and Photobiology C: Photochemistry Reviews 6 (2005) 186–205.
[36] (a) A. Kudo, Y. Miseki, Chemical Society Reviews 38 (2009) 253–278;
(b) K. Maeda, K. Domen, Journal of Physical Chemistry Letters 18 (2010) 2655–2661;
(c) P.V. Kamat, Journal of Physical Chemistry Letters 3 (2012) 663–672.
[37] U.I. Gaya, A.H. Abdullah, Journal of Photochemistry and Photobiology C: Photochemistry Reviews 9 (2008) 1–12.
[38] U.G. Akpan, B.H. Hameed, Journal of Hazardous Materials 170 (2009) 520–529.
[39] S. Ahmed, M.G. Rasul, R. Brown, M.A. Hashib, Journal of Environmental Management 92 (2011) 311–330.
[40] F. Han, V.S.R. Kambala, M. Srinivasan, D. Rajarathnam, R. Naidu, Applied Catalysis A: General 359 (2009) 25–40.
[41] X. Chen, S. Shen, L. Guo, S.S. Mao, Chemical Reviews 110 (2010) 6503–6570.
[42] (a) S.G. Kumar, L.G. Devi, Journal of Physical Chemistry A 115 (2011) 13211–13241;
(b) L.G. Devi, S.G. Kumar, Central European Journal of Chemistry 9 (2011) 959–961.
[43] M. Kitano, M. Matsuoka, M. Ueshima, M. Anpo, Applied Catalysis A: General 325 (2007) 1–14.
[44] X. Hu, G. Li, J.C. Yu, Langmuir 26 (2010) 3031–3039.
[45] C. Aprile, A. Corma, H. Garcia, Physical Chemistry Chemical Physics 10 (2008) 769–783.
[46] Q. Xiang, J. Yu, M. Jaroniec, Chemical Society Reviews 41 (2012) 782–796.
[47] S. Livraghi, A.M. Czoska, M.C. Paganini, E. Gimello, Journal of Solid State Chemistry 182 (2009) 160–164.
[48] X. Zhou, F. Peng, H. Wang, H. Yu, J. Yang, Materials Research Bulletin 46 (2011) 840–844.
[49] D. Zhang, F. Zeng, Applied Surface Science 257 (2010) 867–871.
[50] (a) E.A.R. Garcia, Y. Sun, D. Raftery, Journal of Physical Chemistry C 111 (2007) 17146–17154;
(b) L.G. Devi, S.G. Kumar, Applied Surface Science 261 (2012) 137–146.
[51] (a) N. Murakami, T. Chiyoya, T. Tsubota, T. Ohno, Applied Catalysis A: General 348 (2008) 148–152;
(b) L.G. Devi, K.E. Rajashekhar, Journal of Molecular Catalysis A: Chemical 334 (2011) 65–76.
[52] G. Shao, F. Wang, T. Ren, Y. Liu, Z. Yuan, Applied Catalysis B: Environmental 92 (2009) 61–67.
[53] C. Chen, W. Cai, M. Long, J. Zhang, B. Zhou, Y. Wu, D. Wu, Journal of Hazardous Materials 178 (2010) 560–565.
[54] J. Xu, Y. Ao, D. Fu, Applied Surface Science 256 (2009) 884–888.
[55] F. Dong, H. Wang, G. Sen, Z. Wu, S.C. Lee, Journal of Hazardous Materials 187 (2011) 509–516.
[56] A. Charanpahari, S.S. Umare, S.P. Gokhale, V. Sudarsan, B. Sreedhar, R. Sasikala, Applied Catalysis A: General 443–444 (2012) 96–102.
[57] E.A. Kozlova, T.P. Lyubina, M.A. Nasalevich, A.V. Vorontsov, A.V. Miller, V.V. Kaichev, V.N. Parmon, Catalysis Communications 12 (2011) 597–601.
[58] S. Zhang, F. Peng, H. Wang, H. Yu, S. Zhang, J. Yang, H. Zhao, Catalysis Communications 12 (2011) 689–693.
[59] V. Subramanian, E.E. Wolf, P.V. Kamat, Journal of the American Chemical Society 126 (2004) 4943–4950.
[60] A.Z. Jurek, E. Kowalska, J.W. Sobczak, W. Lisowski, B. Ohtani, A. Zaleska, Applied Catalysis B: Environmental 101 (2011) 504–514.
[61] S. Yin, T. Sato, Journal of Photochemistry and Photobiology A: Chemistry 169 (2005) 89–94.
[62] (a) N. Wang, L. Zhu, K. Deng, Y. She, Y. Yu, H. Tang, Applied Catalysis B: Environmental 95 (2010) 400–407;
(b) X. Yan, T. Ohno, K. Nishijima, R. Abe, B. Ohtani, Chemical Physics Letters 429 (2006) 606–610;
(c) K. Vinodgopal, D. Wynkoop, P.V. Kamat, Environmental Science & Technology 30 (1996) 1660–1666;
(d) Z. Jin, Zhang, Journal of Physical Chemistry B 104 (2000) 7239–7253.
[63] N. Fu, G. Lu, Chemical Communications 24 (2009) 3591–3593.
[64] S. Kim, J. Yeo, W. Choi, Applied Catalysis B: Environmental 84 (2008) 148–155.
[65] N. Yang, G. Li, W. Wang, X. Yang, W.F. Zhang, Journal of Physics and Chemistry of Solids 72 (2011) 1319–1324.
[66] J. Liu, R. Han, Y. Zhao, H. Wang, W. Lu, T. Yu, Y. Zhang, Journal of Physical Chemistry C 115 (2011) 4507–4515.
[67] T. Ohno, T. Mitsui, M. Matsumura, Chemistry Letters 32 (2003) 364–365.
[68] L. Pan, J. Zou, X. Zhang, L. Wang, Journal of the American Chemical Society 133 (2011) 10000–10002.
[69] N. Wang, L. Zhu, Y. Huang, Y. She, Y. Yu, H. Tang, Journal of Catalysis 266 (2009) 199–206.
[70] R. Sasikala, V. Sudarsan, C. Sudakar, R. Naik, L. Panicker, S.R. Bhardwaj, International Journal of Hydrogen Energy 34 (2009) 6105–6113.
[71] F. Zuo, L. Wang, T. Wu, Z. Zhang, B. Borchardt, P. Fen, Journal of the American Chemical Society 132 (2010) 11856–11857.
[72] (a) J. Zhang, Y. Wu, M. Xing, S.A.K. Leghari, S. Sajjad, Energy & Environmental Science 3 (2010) 715–726;
(b) M.V. Dozzi, E. Selli, Journal of Photochemistry and Photobiology C: Photochemistry Reviews 14 (2013) 13–28;
(c) M. Pelaez, N.T. Nolan, S.C. Pillai, M.K. Serry, P. Falaras, A.G. Kontos, P.S.M. Dunlop, J.W.J. Hamilton, J.A. Byrne, K.O. Shea, M.H. Entezari, D.D. Dionysiou, Applied Catalysis B: Environmental 125 (2012) 331–349.
[73] L.G. Devi, N. Kottam, S.G. Kumar, Journal of Physical Chemistry C 113 (2009) 15593–15601.
[74] L.G. Devi, B.N. Murthy, S.G. Kumar, Chemosphere 76 (2009) 1163–1166.
[75] L.G. Devi, S.G. Kumar, B.N. Murthy, N. Kottam, Catalysis Communications 10 (2009) 794–798.
[76] L.G. Devi, B.N. Murthy, S.G. Kumar, Journal of Molecular Catalysis A: Chemical 308 (2009) 174–181.
[77] L.G. Devi, N. Kottam, B.N. Murthy, S.G. Kumar, Journal of Molecular Catalysis A: Chemical 328 (2010) 44–52.
[78] L.G. Devi, B.N. Murthy, S.G. Kumar, Materials Science and Engineering: B 166 (2010) 1–6.
[79] L.G. Devi, N. Kottam, S.G. Kumar, K.E. Rajashekhar, Central European Journal of Chemistry 8 (2009) 142–148.
[80] L.G. Devi, N. Kottam, S.G. Kumar, K.S.A. Raju, Catalysis Letters 131 (2009) 612–617.
[81] L.G. Devi, B.N. Murthy, S.G. Kumar, Catalysis Letters 130 (2009) 496–503.
[82] N. Murakami, T. Chivova, T. Tsubota, T. Ohno, Applied Catalysis A: General 348 (2008) 148–152.
[83] J. Yu, Q. Xiang, M. Zhou, Applied Catalysis B: Environmental 90 (2009) 595–602.
[84] P. Bouras, E. Stathatos, P. Lianos, Applied Catalysis B: Environmental 73 (2007) 51–59.
[85] M. Matsuoka, M. Kitano, M. Takeuchi, K. Tsujimaru, M. Anpo, J.M. Thomas, Catalysis Today 122 (2007) 51–61.
[86] W. Choi, A. Termin, M.R. Hoffmann, Journal of Physical Chemistry 98 (1994) 13669–13679.
[87] K. Nagaveni, M.S. Hegde, G. Madras, Journal of Physical Chemistry B 108 (2004) 20204–20212.
[88] L.G. Devi, S.G. Kumar, Applied Surface Science 257 (2011) 2779–2790.
[89] J. Choi, H. Park, M.R. Hoffmann, Journal of Physical Chemistry C 114 (2010) 783–792.
[90] C. Burda, M.A. El-Sayed, Pure and Applied Chemistry 72 (2000) 165–177.
[91] (a) G. Liu, X. Wang, Z. Chen, H.M. Cheng, G.Q. Lu, Journal of Colloid and Interface Science 329 (2009) 331–338;
(b) G. Liu, X. Wang, L. Wang, Z. Chen, F. Li, G.Q. Lu, H.M. Cheng, Journal of Colloid and Interface Science 334 (2009) 171–175.
[92] S. Higashimoto, M. Azuma, Applied Catalysis B: Environmental 89 (2009) 557–562.
[93] D. Li, H. Haneda, S. Hishita, N. Ohashi, Chemistry of Materials 17 (2005) 2596–2602.
[94] Y. Lei, L.D. Zhang, G.H. Li, X.Y. Zhang, G.W. Meng, C.H. Liang, W. Chen, S.X. Wang, Applied Physics Letters 78 (2001) 1125–1127.
[95] J.S. Jang, H.G. Kim, S.M. Ji, S.W. Bae, J.H. Jung, B.H. Shon, J.S. Lee, Journal of Solid State Chemistry 179 (2006) 1067–1075.
[96] I.N. Martyanov, S. Uma, S. Rodrigues, K.J. Klabunde, Chemical Communications 21 (2004) 2476–2477.
[97] X. Chen, Y. Lou, A.C.S. Samia, C. Burda, J.L. Gole, Advanced Functional Materials 15 (2005) 4–49.
[98] F. Peng, L. Cai, H. Yu, H. Wang, J. Yang, Journal of Solid State Chemistry 181 (2008) 130–136.
[99] C.D. Valentin, G. Pacchioni, A. Selloni, S. Livraghi, E. Giamello, Journal of Physical Chemistry B 109 (2005) 11414–11419.

[100] C.D. Valentin, G. Pacchioni, A. Selloni, Physical Review B 70 (2004) (Article ID 085116).
[101] X.B. Chen, C. Burda, Journal of Physical Chemistry B 108 (2004) 15446–15449.
[102] M.S. Wong, H.P. Chou, T.S. Yang, Thin Solid Films 494 (2006) 244–249.
[103] S. Sakthivel, M. Janczarek, H. Kisch, Journal of Physical Chemistry B 108 (2004) 19384–19387.
[104] J. Wang, B. Mao, J.L. Gole, C. Burda, Nanoscale 2 (2010) 2257–2261.
[105] F. Xia, Y. Zhu, L. Feng, L. Jiang, Soft Matter 5 (2009) 275–281.
[106] X.J. Feng, J. Zhai, L. Jiang, Angewandte Chemie International Edition 44 (2005) 5115–5118.
[107] S. Chen, P.Y. Zhang, D.M. Zhuang, W.P. Zhu, Catalysis Communications 5 (2004) 677–680.
[108] X. Fang, Z. Zhang, Q. Chen, H. Ji, X. Gao, Journal of Solid State Chemistry 180 (2007) 1325–1332.
[109] W. Balcerski, S.Y. Ryu, M.R. Hoffmann, Journal of Physical Chemistry C 111 (2007) 15357–15362.
[110] R. Asahi, T. Morikawa, K. Ohwaki, K. Aoki, Y. Taga, Science 293 (2001) 269–271.
[111] L. Mi, P. Xu, H. Shen, P.N. Wang, Journal of Photochemistry and Photobiology A: Chemistry 193 (2008) 222–227.
[112] H. Li, Y. Hou, Journal of Physical Chemistry B 110 (2006) 1559–1565.
[113] Y. Guo, X.W. Zhang, W. Hao, G.R. Han, Thin Solid Films 515 (2007) 7117–7121.
[114] Y. Guo, X.W. Zhang, G.R. Han, Materials Science and Engineering: B 135 (2006) 83–87.
[115] K. Prabakar, T. Takahashi, T. Nezuka, K. Takahashi, T. Nakashima, Y. Kubota, A. Fujishima, Renewable Energy 33 (2008) 277–281.
[116] F.D. Duminica, F. Maury, R. Hausbrand, Surface and Coatings Technology 201 (2007) 9349–9353.
[117] Z. Zhang, X. Wang, J. Long, Q. Gu, Z. Ding, X. Fu, Journal of Catalysis 276 (2010) 201–214.
[118] L. Wan, J.F. Li, J.Y. Feng, W. Sun, Z.Q. Mao, Applied Surface Science 253 (2007) 4764–4767.
[119] V.J. Babu, A.S. Nair, Z. Peining, S. Ramakrishna, Materials Letters 65 (2011) 3064–3068.
[120] S.K. Kim, S.J. Hwang, W. Choi, Journal of Physical Chemistry B 109 (2005) 24260–24267.
[121] X.F. You, F. Chen, J.L. Zhang, M. Anpo, Catalysis Letters 102 (2005) 247–250.
[122] B.Z. Tian, J.L. Zhang, T.Z. Tong, F. Chen, Applied Catalysis B: Environmental 79 (2008) 394–401.
[123] Q. Li, R. Xie, E.A. Mintz, J.K. Shang, Journal of the American Ceramic Society 90 (2007) 3863–3868.
[124] Q. Li, J.K. Shang, Environmental Science & Technology 44 (2010) 3493–3499.
[125] P. Wu, R. Xie, J.A. Imlay, J.K. Shang, Applied Catalysis B: Environmental 88 (2009) 576–581.
[126] D. Li, Z. Chen, Y. Chen, W. Li, H. Huang, Y. He, X. Fu, Environmental Science & Technology 42 (2008) 2130–2135.
[127] B. Tian, C. Li, F. Gu, H. Jiang, Catalysis Communications 10 (2009) 925–929.
[128] X.Z. Li, F.B. Li, Environmental Science & Technology 35 (2001) 2381–2387.
[129] R. Zanella, S. Giorgio, C.H. Shin, C.R. Henry, C. Louis, Journal of Catalysis 222 (2004) 357–367.
[130] I.M. Arabatzis, T. Stergiopoulos, D. Andreeva, S. Kitova, S.G. Neophytides, P. Falaras, Journal of Catalysis 220 (2003) 127–135.
[131] J. Yu, L. Yue, S. Liu, B. Huang, X. Zhang, Journal of Colloid and Interface Science 334 (2009) 58–64.
[132] C.W. Dunill, Z. Ansari, A. Kafizas, S. Perni, D.J. Morgan, M. Wilson, I.P. Parkin, Journal of Materials Chemistry 21 (2011) 11854–11861.
[133] K. Yamada, H. Yamane, S. Matsushima, H. Nakamura, K. Ohira, M. Kouya, K. Kumada, Thin Solid Films 516 (2008) 7482–7487.
[134] J. Geng, D. Yang, J. Zhu, D. Chen, Z. Jiang, Materials Research Bulletin 44 (2009) 146–150.
[135] Y. Huang, Z. Xixu, Y. Zhongi, T. Feng, F. Beibei, H. Keshan, Chinese Journal of Chemical Engineering 15 (2007) 802–807.
[136] C.L. Bianchi, G. Cappelletti, S. Ardizzone, S. Gialanella, A. Naldoni, C. Oliva, C. Pirola, Catalysis Today 144 (2009) 31–36.
[137] S. Livraghi, M.C. Paganini, E. Giamello, A. Selloni, C. Di Valentin, G. Pacchioni, Journal of the American Chemical Society 128 (2006) 15666–15671.
[138] S. Livraghi, A. Votta, M.C. Paganini, E. Giamello, Chemical Communications 28 (2005) 498–500.
[139] S. Livraghi, K. Elghniji, A.M. Czoska, M.C. Paganini, E. Giamello, M. Ksibi, Journal of Photochemistry and Photobiology A: Chemistry 205 (2009) 93–97.
[140] T.C. Jagadale, S.P. Takale, R.S. Sonawane, H.M. Joshi, S.I. Patil, B.B. Kale, S.B. Ogale, Journal of Physical Chemistry C 112 (2008) 14595–14602.
[141] M. Satish, B. Viswanathan, R.P. Viswanth, C.S. Gopinath, Chemistry of Materials 17 (2005) 6349–6353.
[142] Y. Wang, C. Feng, Z. Jin, J. Zhang, J. Yang, S. Zhang, Journal of Molecular Catalysis A: Chemical 260 (2006) 1–3.
[143] C. Feng, Y. Wang, Z. Jin, J. Zhang, S. Zhang, Z. Wu, Z. Zhang, New Journal of Chemistry 32 (2008) 1038–1047.
[144] C. Feng, Z. Jin, J. Zhang, Z. Wu, Z. Zhang, Photochemistry and Photobiology 86 (2010) 1222–1229.
[145] A.V. Emeline, N.V. Sheremetyeva, N.V. Khomchenko, V.K. Ryabchuk, N. Serpone, Journal of Physical Chemistry C 111 (2007) 11456–11462.
[146] Q.Y. Li, X.D. Wang, Z.S. Jin, D.G. Yang, S.L. Zhang, X.Y. Guo, J.J. Yang, Z.J. Zhang, Journal of Nanoparticle Research 5 (2007) 951–957.
[147] Y.H. Cheng, Y. Huang, P.D. Kanhere, V.P. Subramaniam, D. Gong, S. Zhang, J. Highfield, M.K. Schreyer, Z. Chen, Chemistry: A European Journal 17 (2011) 2575–2578.
[148] X. Qui, Y. Zhao, C. Burda, Advanced Materials 19 (2007) 3995–3999.
[149] Z. Wu, F. Dong, W. Zhao, S. Guo, Journal of Hazardous Materials 157 (2008) 57–63.
[150] X. Qiu, C. Burda, Chemical Physics 339 (2007) 1–10.
[151] Y. Cong, J.L. Zhang, F. Chen, M. Anpo, Journal of Physical Chemistry C 111 (2007) 6976–6982.
[152] J.G. Yu, H.G. Yu, B. Cheng, X.J. Zhao, J.C. Yu, W.K. Ho, Journal of Physical Chemistry B 107 (2003) 13871–13879.
[153] X.Z. Li, F.B. Li, C.L. Yang, W.K. Ge, Journal of Photochemistry and Photobiology A: Chemistry 141 (2001) 209–217.
[154] M. Zhou, J. Yu, S. Liu, P. Zhai, L. Jiang, Journal of Hazardous Materials 154 (2008) 1141–1148.
[155] F. Dong, W. Zhao, Z. Wu, S. Guo, Journal of Hazardous Materials 162 (2009) 763–770.
[156] K. Nagaveni, M.S. Hegde, N. Ravishankar, G.N. Subbanna, G. Madras, Langmuir 20 (2004) 2900–2907.
[157] J. Yu, H.G. Yu, B. Cheng, M.H. Zhou, X.J. Zhao, Journal of Molecular Catalysis A: Chemical 253 (2006) 112–118.
[158] Z.B. Wu, Z.L. Gu, W.R. Zhao, H.Q. Wang, Chinese Science Bulletin 52 (2007) 3061–3067.
[159] L. Li, C.Y. Liu, European Journal of Inorganic Chemistry (2009) 3727–3733.
[160] J.C. Yu, L. Zhang, J. Yu, Chemistry of Materials 14 (2002) 4647–4653.
[161] J. Yu, J.C. Yu, W. Ho, L.Z. Zhang, Chemical Communications 19 (2001) 1942–1943.
[162] S. Ardizzone, C.L. Bianchi, G. Cappelletti, S. Gialanella, C. Pirola, V. Ragaini, Journal of Physical Chemistry C 111 (2007) 13222–13231.
[163] J. Yu, M. Zhou, B. Cheng, H. Yu, X. Zhao, Journal of Molecular Catalysis A: Chemical 227 (2005) 75–80.
[164] Y. Yu, J.C. Yu, J. Yu, Y.C. Kwok, Y.K. Che, J.C. Zhao, L. Ding, W.K. Ge, P.K. Wong, Applied Catalysis A: General 289 (2005) 186–196.
[165] X. Kang, S. Chen, Journal of Materials Science 45 (2010) 2696–2702.
[166] A.R. Gandhe, J.B. Fernandes, Journal of Solid State Chemistry 178 (2005) 2953–2957.
[167] K. Sivaranjani, C.S. Gopinath, Journal of Materials Chemistry 21 (2011) 2639–2647.
[168] G. Tang, J. Li, M. Sun, X. Ma, Applied Surface Science 255 (2009) 9224–9229.
[169] P.A. Mangrulkar, S.P. Kamble, M.M. Joshi, J.S. Meshram, N.K. Labhsetwar, S.S. Rayulu, International Journal of Photoenergy (2012), Article ID 780562.
[170] S. Yin, H. Yamaki, M. Komatsu, Q. Zhang, J. Wang, Q. Tang, F. Saito, T. Sato, Solid State Sciences 7 (2005) 1479–1485.
[171] S. Yin, H. Yamaki, M. Komatsu, Q. Zhang, J. Wang, Q. Tang, F. Saito, T. Sato, Journal of Materials Chemistry 13 (2003) 2996–3300.
[172] T. Ikoma, Q. Zhang, F. Saito, K. Akiyama, S. Tero, T. Kato, Bulletin of Chemical Society of Japan 74 (2001) 2303–2309.
[173] L. Lee, Q. Zhang, F. Saito, Industrial & Engineering Chemistry Research 40 (2001) 4785–4788.
[174] S. Yin, H. Yamaki, Q. Zhang, M. Komatsu, J. Wang, Q. Tang, F. Saito, T. Sato, Solid State Ionics 172 (2004) 205–209.
[175] C. Shifu, C. Lie, G. Shen, C. Gengyu, Chemical Physics Letters 413 (2005) 404–409.
[176] C. Shifu, C. Lie, G. Shen, C. Gengyu, Materials Chemistry and Physics 98 (2006) 116–120.
[177] M. Xing, J. Zhang, F. Chen, Applied Catalysis B: Environmental 89 (2009) 563–569.
[178] Y. Zhao, X. Qiu, C. Burda, Chemistry of Materials 20 (2008) 2629–2636.
[179] Y. Aita, M. Komatsu, S. Yin, T. Sato, Journal of Solid State Chemistry 177 (2004) 3235–3238.
[180] T. Sato, Y. Aita, M. Komatsu, S. Yin, Journal of Materials Science 41 (2006) 1433–1438.
[181] V. Etacheri, M.K. Seery, S.J. Hinder, S.C. Pillai, Chemistry of Materials 22 (2010) 3843–3853.
[182] Y. Cong, J. Zhang, F. Chen, M. Anpo, Journal of Physical Chemistry C 111 (2007) 6976–6982.
[183] H. Sun, Y. Bai, W. Jin, N. Xu, Solar Energy Materials and Solar Cells 92 (2008) 76–83.
[184] A. Markovits, B. Mguig, M. Calatayud, C. Minot, Catalysis Today 113 (2006) 201–207.
[185] D. Li, H. Huang, X. Chen, W. Li, D. Ye, X. Fu, Journal of Solid State Chemistry 180 (2007) 2630–2634.
[186] M. Janus, J. Chiona, A.W. Morawski, Journal of Hazardous Materials 166 (2009) 1–5.
[187] K. Vinodgopal, D.E. Wynkoop, P.V. Kamat, Environmental Science & Technology 30 (1996) 1660–1666.
[188] R. Kun, S. Tarjan, A. Oszko, T. Seemann, V. Zollmer, M. Busse, I. Dekany, Journal of Solid State Chemistry 182 (2009) 3076–3084.
[189] O. Saur, M. Bensitel, A.B.M. Saad, J.C. Lavalley, C.P. Tripp, B.A. Morrow, Journal of Catalysis 99 (1986) 104–110.
[190] G. Colon, J.M.S. Espana, M.C. Hidalgo, J.A. Navio, Journal of Photochemistry and Photobiology A: Chemistry 179 (2006) 20–27.
[191] T. Jin, T. Yamaguchi, K. Tanabe, Journal of Physical Chemistry 90 (1986) 4794–4796.
[192] X. Wang, J.C. Yu, P. Liu, X. Wang, W. Su, X. Fu, Journal of Photochemistry and Photobiology A: Chemistry 179 (2006) 339–347.
[193] Y. Li, C. Xie, S. Peng, G. Lu, S. Li, Journal of Molecular Catalysis A: Chemical 282 (2008) 117–123.

[194] Y.D. Hou, X.C. Wang, L. Wu, X.F. Chen, Z.X. Ding, X.X. Wang, X.Z. Fu, Chemosphere 72 (2008) 414–421.
[195] J.G. Yu, H.G. Yu, B. Cheng, B.X.J. Zhao, J.C. Yu, W.K. Ho, Journal of Physical Chemistry B 107 (2003) 13871–13879.
[196] L. Zhang, J.C. Yu, Chemical Communications (2003) 2078–2079.
[197] I.C. Kang, Q. Zhang, S. Yin, T. Sato, F. Saito, Environmental Science & Technology 42 (2008) 3622–3626.
[198] M. Xing, J. Zhang, F. Chen, Journal of Physical Chemistry C 113 (2009) 12848–12853.
[199] T. Ohno, Z. Miyamoto, K. Nishijima, H. Kanemitsu, F. Xueyuan, Applied Catalysis A: General 302 (2006) 62–68.
[200] S. Higashimoto, W. Tanihata, Y. Nakagawa, M. Azuma, H. Ohue, Y. Sakata, Applied Catalysis A: General 340 (2008) 98–104.
[201] T. Ikeda, T. Tomonori, K. Eda, Y. Mizutani, H. Kato, A. Kudo, H. Onishi, Journal of Physical Chemistry C 112 (2008) 1167–1173.
[202] R. Niishiro, H. Kato, A. Kudo, Physical Chemistry Chemical Physics 7 (2005) 2241–2245.
[203] J. Graciani, A. Nambu, J. Evans, J.A. Rodriguez, J.F. Sanz, Journal of the American Chemical Society 130 (2008) 12056–12063.
[204] Y. Wang, Y. Wang, Y.L. Meng, H.M. Ding, Y.K. Shan, X. Zhao, X.Z. Tang, Journal of Physical Chemistry C 112 (2008) 6620–6626.
[205] T.H. Kim, V.R. Gonzalez, G. Gyawali, S.H. Cho, T. Sekino, S.W. Lee, Catalysis Today (2012), http://dx.doi.org/10.1016/jcattod.2012.09.014.
[206] (a) W. Pingxiao, T. Jianwen, D. Zhi, Materials Chemistry and Physics 103 (2007) 264–269;
(b) X.Z. Shen, Z.C. Liu, S.M. Xie, J. Guo, Journal of Hazardous Materials 162 (2009) 1193–1198;
(c) C. Wang, Y. Ao, P. Wang, J. Hou, J. Qian, Powder Technology 210 (2011) 203–207.
[207] (a) D.G. Huang, S.J. Liao, W.B. Zhou, S.Q. Quan, L. Liu, Z.J. He, J.B. Wan, Journal of Physics and Chemistry of Solids 70 (2009) 853–859;
(b) Y. Cong, B. Tian, J. Zhang, Applied Catalysis B: Environmental 101 (2011) 376–381;
(c) A.W. Xu, Y. Gao, H.Q. Liu, Journal of Catalysis 207 (2002) 151–157.
[208] X. Zhang, Q. Liu, Applied Surface Science 254 (2008) 4780–4785.
[209] (a) T. Mishra, M. Mahato, N. Aman, J.N. Patel, R.K. Sahu, Catalysis Science & Technology 1 (2011) 609–615;
(b) S.S. Thind, G. Wu, M. Tian, A. Chen, Nanotechnology 23 (2012) 475706;
(c) A.K.L. Sajjad, S. Shamaila, J. Zhang, Materials Research Bulletin 47 (2012) 3083–3089;
(d) K. Obata, H. Irie, K. Hashimoto, Chemical Physics 339 (2007) 124–132.
[210] V. Keller, P. Bernhardt, F. Garin, Journal of Catalysis 215 (2003) 129–138.
[211] J. Papp, S. Soled, K. Dwight, A. Wold, Chemistry of Materials 6 (1994) 496–500.
[212] D.M. Stanbury, Advances in Inorganic Chemistry 33 (1989) 69–138.
[213] K. Song, J. Zhou, J. Bao, Y. Feng, Journal of the American Ceramic Society 91 (2008) 1369–1371.
[214] Y. Sakatani, H. Ando, K. Okusako, H. Koike, Journal of Materials Research 19 (2004) 2100–2108.
[215] R.D. Iyengar, R. Kellerman, Journal of Colloid and Interface Science 35 (1971) 424–433.
[216] M. Che, C. Naccache, Chemical Physics Letters 8 (1971) 45–48.
[217] H. Liu, G. Liu, J. Fan, Q. Zhou, H. Zhou, H. Zhou, N. Zhang, Z. Hou, M. Zhang, Z. He, Chemosphere 82 (2011) 43–47.
[218] M. Yang, C. Hume, S. Lee, Y.H. Son, J.K. Lee, Journal of Physical Chemistry C 114 (2010) 15292–15297.
[219] A. Fujishima, X. Zhang, D.A. Tryk, Surface Science Reports 63 (2008) 515–582.
[220] M. Maeda, T. Watanabe, Journal of the Electrochemical Society 153 (2006) 186–189.
[221] K. Yang, H. Bai, X. Tan, J. Lian, Applied Surface Science 253 (2006) 1988–1994.
[222] J.A.R. Herrera, E. Mielczarski, J. Mielczarski, N.C. Castillo, J. Kiwi, C. Pulgarin, Applied Catalysis B: Environmental 84 (2008) 448–456.
[223] G. Yan, M. Zhang, J. Hou, J. Yang, Materials Chemistry and Physics 129 (2011) 553–557.
[224] J.A.R. Herrera, K. Pierzchala, A. Sienkiewiez, L. Forro, J. Kiwi, J.E. Moser, C. Pulgarin, Journal of Physical Chemistry C 114 (2010) 2717–2723.
[225] T.L. Thompson, J.T. Yates, Chemical Reviews 106 (2006) 4428–4453.
[226] C.D. Valentin, E. Finazzi, G. Pacchioni, A. Selloni, S. Livraghi, M.C. Paganini, E. Giamello, Chemical Physics 339 (2007) 44–56.
[227] C. Naccache, P. Meriaudeau, M. Che, A.J. Tench, Transactions of the Faraday Society 67 (1971) 506–512.
[228] L. Zhou, J. Deng, Y. Zhao, W. Liu, L. An, F. Chen, Materials Chemistry and Physics 117 (2009) 522–527.
[229] W.Y. Su, Y.F. Zhang, Z.H. Li, L. Wu, X.X. Wang, J.Q. Li, X.Z. Fu, Langmuir 24 (2008) 3422–3428.
[230] C.G. Xi, M. Ying, L. Dong, G. Cao, Y. Ma, X. Jia, G. Ye, S. Guan, Transactions of Nonferrous Metals Society of China 19 (2009) 1583–1587.
[231] L. Dong, Y. Ma, Y. Wang, Y. Tian, G. Ye, X. Jia, G. Cao, Materials Letters 64 (2009) 1598–1600.
[232] M. Pelaez, A.A. Cruz, E. Stathatos, P. Falaras, D.D. Dionysiou, Catalysis Today 144 (2009) 19–25.
[233] Y.T. Kwon, K.Y. Song, W.I. Lee, G.J. Choi, Y.R. Do, Journal of Catalysis 191 (2000) 192–199.
[234] S.R. Morrison, Surface Science 50 (1975) 329–342.
[235] N. Serpone, D. Lawless, R. Khairutdinov, Journal of Physical Chemistry 99 (1995) 16646–16654.
[236] Y. Lei, L.D. Zhang, G.W. Meng, G.H. Li, X.Y. Zhang, C.H. Liang, W. Chen, X.S. Wang, Applied Physics Letters 78 (2001) 1125–1127.
[237] A.V. Emeline, G.N. Kuzmin, D. Pirevdorj, V.K. Ryabchuk, N. Serpone, Journal of Physical Chemistry B 104 (2000) 2989–2999.
[238] J. Xu, B. Yang, M. Xu, Z. Fu, Y. Lv, Y. Zhao, Journal of Physical Chemistry C 114 (2010) 15251–15259.
[239] Y. Li, T. Kunitake, S. Fujikawa, Journal of Physical Chemistry B 110 (2006) 13000–13004.
[240] Q. Li, J.K. Shang, Journal of the American Ceramic Society 91 (2008) 660–663.
[241] S. Nishimura, N. Abrams, B.A. Lewis, L.I. Halaoui, T.E. Mallouk, K.D. Benkstein, J. Van de Lagemaat, A.J. Frank, Journal of the American Chemical Society 125 (2003) 6306–6310.
[242] J.I.L. Chen, G.V. Freymann, S.Y. Choi, V. Kitaev, G.A. Ozin, Journal of Materials Chemistry 18 (2008) 369–373.
[243] J.I.L. Chen, G.V. Freymann, V. Kitaev, G.A. Ozin, Journal of the American Chemical Society 129 (2007) 1196–1202.
[244] W.Z. Peng, X. Jun, C. Weimin, Z.B. Xue, H.Z. Guang, C.C. Guang, H.X. Ting, Journal of Environmental Sciences 17 (2005) 76–80.
[245] S. Liu, J. Yu, W. Wang, Physical Chemistry Chemical Physics 12 (2010) 12308–12315.
[246] (a) J.C. Parker, R.W. Siegal, Journal of Materials Research 5 (1990) 1246–1252;
(b) X. Cheng, X. Yu, Z. Xing, L. Yang, International Journal of Photoenergy (2012), Article ID 593245.
[247] G. Liu, C. Sun, L. Cheng, Y. Jin, H. Lu, L. Wang, S.C. Smith, G.Q. Lu, H.M. Cheng, Journal of Physical Chemistry C 113 (2009) 12317–12324.
[248] X. Zhou, F. Peng, H. Wang, H. Yu, J. Yang, Electrochemistry Communications 13 (2011) 121–124.
[249] X. Zhou, F. Peng, H. Wang, H. Ju, J. Yang, Journal of Solid State Chemistry 184 (2011) 134–140.
[250] X. Zhou, F. Peng, H. Wang, H. Yu, Journal of Solid State Chemistry 184 (2011) 3002–3007.
[251] X. Yang, C. Cao, L. Erickson, K. Hohn, R. Maghirang, K. Klabunde, Applied Catalysis B: Environmental 91 (2009) 657–662.
[252] M. Zhou, J. Yu, Journal of Hazardous Materials 152 (2008) 1229–1236.
[253] S. Liu, L. Yang, S. Xu, S. Xu, S. Luo, Q. Cai, Electrochemistry Communications 11 (2009) 1748–1751.
[254] K.M. Parida, N. Sahu, A.K. Tripathi, V.S. Kamble, Environmental Science & Technology 44 (2010) 4155–4160.
[255] M. Chen, W. Goodman, Accounts of Chemical Research 39 (2006) 739–746.
[256] M.A. Henderson, S. OteroTapia, M.E. Castro, Faraday Discussions 114 (1999) 313–329.
[257] M. Grandcolas, J. He, Science and Technology of Advanced Materials 11 (2010) 055001.
[258] V. Stengl, V. Houskova, S. Bakardjieva, N. Murafa, Applied Materials & Interfaces 2 (2010) 575–580.
[259] A. Zaleska, J.W. Sobczak, E. Grabowska, J. Hupka, Applied Catalysis B: Environmental 78 (2008) 92–100.
[260] A. Zaleska, E. Grabowska, J.W. Sobczak, M. Gazda, J. Hupka, Applied Catalysis B: Environmental 89 (2009) 469–475.
[261] X. Wang, M. Blackford, K. Prince, R.A. Caruso, Applied Materials & Interfaces 4 (2012) 476–482.
[262] E. Kowalska, O.O.P. Mahaney, R. Abe, B. Ohtani, Physical Chemistry Chemical Physics 12 (2010) 2344–2355.
[263] B. Tian, Z. Shao, Y. Ma, J. Zhang, F. Chen, Journal of Physics and Chemistry of Solids 72 (2011) 1290–1295.
[264] N. Lu, H. Zhao, J. Li, X. Quan, S. Chen, Separation and Purification Technology 62 (2008) 668–673.
[265] D. Chen, D. Yang, Q. Wang, Z. Jiang, Industrial & Engineering Chemistry Research 45 (2006) 4110–4116.
[266] H. Asada, T. Itoh, Y. Kodera, Biotechnology and Bioengineering 76 (2001) 86–90.
[267] Z. Jiang, C. Lu, H. Wu, Industrial & Engineering Chemistry Research 44 (2005) 4165–4170.
[268] M. Janus, M. Inagaki, B. Tryba, M. Toyoda, A.W. Moraswski, Applied Catalysis B: Environmental 63 (2006) 272–276.
[269] Q. Xiao, L.L. Ouyang, Chemical Engineering Journal 148 (2009) 248–253.
[270] C.D. Valentin, G. Pacchioni, A. Selloni, Chemistry of Materials 17 (2005) 6656–6665.
[271] S.U.M. Khan, M. Al-Shahry, W.B. Ingler, Science 297 (2002) 2243–2244.
[272] C. Xu, Y.A. Shaban, W.B.I.S Jr., S.U.M. Khan, Solar Energy Materials and Solar Cells 91 (2007) 938–943.
[273] G.K. Mor, K. Shankar, M. Paulose, O.K. Varghese, C.A. Grimes, Nano Letters 5 (2005) 191–195.
[274] S. Sakthivel, H. Kisch, Angewandte Chemie International Edition 42 (2003) 4908–4911.
[275] F. Dong, S. Guo, H. Wang, X. Li, Z. Wu, Journal of Physical Chemistry C 115 (2011) 13285–13292.
[276] F. Dong, H. Wang, Z. Wu, Journal of Physical Chemistry C 113 (2009) 16717–16723.
[277] S. Liu, J. Yu, M. Jaroniec, Journal of the American Chemical Society 132 (2010) 11914–11916.
[278] J.G. Yu, G.H. Wang, B. Cheng, M.H. Zhou, Applied Catalysis B: Environmental 69 (2007) 171–180.
[279] Y. Park, W. Kim, H. Park, T. Tachikawa, T. Majima, W. Choi, Applied Catalysis B: Environmental 91 (2009) 355–361.

[280] U. Stafford, K.A. Gray, P.V. Kamat, Journal of Physical Chemistry 98 (1994) 6343–6351.
[281] P. Wardman, Journal of Physical and Chemical Reference Data 18 (1989) 1637–1755.
[282] C. Lormann, D.W. Bahnemann, M.R. Hoffmann, Journal of Physical Chemistry 92 (1988) 5196–5201.
[283] Z. Wu, F. Dong, Y. Liu, H. Wang, Catalysis Communications 11 (2009) 82–86.
[284] R. Zheng, Y. Guo, C. Jin, J. Xie, Y. Zhu, Y. Xie, Journal of Molecular Catalysis A: Chemical 319 (2010) 46–51.
[285] L. Korosi, S. Papp, I. Bertoti, I. Dekany, Chemistry of Materials 19 (2007) 4811–4819.
[286] R. Zheng, L. Lin, J. Xie, Y. Zhu, Y. Xie, Journal of Physical Chemistry C 112 (2008) 15502–15509.
[287] F. Li, Y. Jiang, M. Xia, M. Sun, B. Xue, D. Liu, X. Zhang, Journal of Physical Chemistry C 113 (2009) 18134–18141.
[288] J.C. Yu, L.Z. Zhang, Z. Zheng, J.C. Zhao, Chemistry of Materials 15 (2003) 2280–2286.
[289] J.C. Yu, L.Z. Zhang, J.G. Yu, Chemistry of Materials 14 (2002) 4647–4653.
[290] S.J. Tsai, S. Cheng, Catalysis Today 33 (1997) 227–237.
[291] Q. Shi, D. Yang, Z. Jiang, J. Li, Journal of Molecular Catalysis B: Enzymatic 43 (2006) 44–48.
[292] D. Zhao, C. Chen, Y. Wang, H. Ji, W. Ma, L. Zang, J. Zhao, Journal of Physical Chemistry C 112 (2008) 5993–6001.
[293] L. Korosi, I. Dekany, Colloids and Surfaces A: Physicochemical and Engineering Aspects 280 (2006) 146–154.
[294] M.R. Bayati, F.G. Fard, A.Z. Moshfegh, R. Molaei, Materials Research Bulletin 46 (2011) 1642–1647.
[295] Y. Niu, M. Xing, B. Tian, J. Zhang, Applied Catalysis B: Environmental 115–116 (2012) 253–260.
[296] W. Ho, J.C. Yu, S. Lee, Journal of Solid State Chemistry 179 (2006) 1171–1176.
[297] J.C. Yu, W. Ho, J. Yu, H. Yip, P. Wong, J. Zhao, Environmental Science & Technology 39 (2005) 1175–1179.
[298] L. Szatmary, S. Bakardjievaa, J. Subrt, P. Bezdicka, J. Jirkovsky, Z. Bastl, V. Brezova, M. Korenko, Catalysis Today 161 (2011) 23–28.
[299] G. Colon, M.C. Hidalgo, G. Munuera, I. Ferino, M.G. Cutrufello, J.A. Navio, Applied Catalysis B: Environmental 63 (2006) 45–59.
[300] X. Zhang, L. Lei, J. Zhang, Q. Chen, J. Bao, B. Fang, Separation and Purification Technology 66 (2009) 417–421.
[301] W. Zhao, W. MA, C. Chen, J.C. Zhao, Z.G. Shuai, Journal of the American Chemical Society 126 (2004) 4782–4783.
[302] S. Sakthivel, H. Kisch, ChemPhysChem 4 (2003) 487–490.
[303] T. Ohno, M. Akiyoshi, T. Umebayashi, K. Asai, T. Mitsui, M. Matsumura, Applied Catalysis A: General 265 (2004) 115–121.
[304] K. Nishijima, Y. Fujisawa, N. Murakami, T. Tsubota, T. Ohno, Applied Catalysis B: Environmental 84 (2008) 584–590.
[305] M. Katoh, H. Aihara, T. Horikawa, T. Tomida, Journal of Colloid and Interface Science 298 (2006) 805–809.
[306] H. Tian, J. Ma, K. Li, J. Li, Ceramics International 35 (2009) 1289–1292.
[307] H. Li, X. Zhang, Y. Huo, J. Zhu, Environmental Science & Technology 41 (2007) 4410–4414.
[308] H. Liu, H.J. Wu, F.X. Sun, Y.L. Yao, M. Wu, W.Z. Li, Chinese Journal of Molecular Catalysis A: Chemical 15 (2001) 47–50.
[309] G. Liu, C. Sun, S.C. Smith, L. Wang, G.Q.M. Lub, H.M. Cheng, Journal of Colloid and Interface Science 349 (2010) 477–483.
[310] M. Hamadanian, A.R. Vanani, A. Majedi, Applied Surface Science 256 (2010) 1837–1844.
[311] Y. Wang, Y. Wang, Y. Meng, H. Ding, Y.S. Zhao, X. Tang, Journal of Physical Chemistry C 112 (2008) 6620–6626.
[312] M.V. Dozzi, S. Livraghi, E. Giamello, E. Selli, Photochemical & Photobiological Sciences 10 (2011) 343–349.
[313] G. Wu, J. Wang, D.F. Thomas, A. Chen, Langmuir 24 (2008) 3503–3509.
[314] J.H. Park, S. Kim, A.J. Bard, Nano Letters 6 (2006) 24–28.
[315] G.S. Wu, T. Nishikawa, B. Ohtani, A. Chen, Chemistry of Materials 19 (2007) 4530–4537.
[316] D. Li, H. Haneda, S. Hishita, N. Ohashi, N.K. Labhsetwar, Journal of Fluorine Chemistry 126 (2005) 69–77.
[317] W. Ho, J.C. Yu, S.C. Yu, S.C. Lee, Chemical Communications (2006) 1115–1117.
[318] S.A. Bagshaw, E. Prouzet, T.J. Pinnavaia, Science 269 (1995) 1242–1244.
[319] R.T. Yang, T.J. Pinnavaia, W. Li, W. Zhang, Journal of Catalysis 172 (1997) 488–493.
[320] T.R. Pauly, Y. Liu, T.J. Pinnavaia, S.J. Billinge, T.P. Rieker, Journal of the American Chemical Society 121 (1999) 8835–8842.
[321] N. Todorova, T. Giannakopoulou, G. Romanos, T. Vaimakis, J. Yu, C. Trapalis, International Journal of Photoenergy (2012), Article Id 534038.
[322] Y. Yu, H. Hong, B.L. Zhu, S.R. Wang, W.P. Haung, S.H. Wu, S.M. Zhang, Catalysis Letters 121 (2008) 165–171.
[323] J.C. Yu, J.G. Yu, W. Ho, Z.T. Jiang, L. Zhang, Chemistry of Materials 14 (2002) 3808–3816.
[324] J. Yu, J.C. Yu, B. Cheng, S.K. Hark, K. Lu, Journal of Solid State Chemistry 174 (2003) 372–380.
[325] Y. Ma, J.W. Fu, X. Tao, X. Li, J.F. Chen, Applied Surface Science 257 (2011) 5046–5051.
[326] Q. Hou, Y.Z. Zheng, J.F. Chen, W.L. Zhou, J. Deng, X. Tao, Journal of Materials Chemistry 21 (2011) 3877–3883.
[327] X. Hong, Z. Wang, W. Cai, F. Lu, J. Zhang, Y. Yang, N. Ma, Y. Liu, Chemistry of Materials 17 (2005) 1548–1552.
[328] G. Liu, Z. Chen, C. Dong, Y. Zhao, F. Li, G.Q. Lu, H.M. Cheng, Journal of Physical Chemistry B 110 (2006) 20823–20828.
[329] G. Li, N.M. Dimitrijevic, L. Chen, J.M. Nichols, T. Rajh, K.A. Gray, Journal of the American Chemical Society 130 (2008) 5402–5403.
[330] G. Li, K.A. Gray, Chemical Physics 339 (2007) 173–187.
[331] D.C. Hurum, K.A. Gray, T. Rajh, M.C. Thurnauer, Journal of Physical Chemistry B 109 (2005) 977–980.
[332] D.C. Hurum, A.G. Agrios, K.A. Gray, T. Rajh, M.C. Thurnauer, Journal of Physical Chemistry B 107 (2003) 4545–4549.
[333] Z. He, L. Zhan, F. Hong, S. Song, Z. Lin, J. Chen, M. Jin, Journal of Environmental Sciences 23 (2011) 166–170.
[334] G. Liu, C. Sun, X. Yan, L. Cheng, Z. Chen, X. Wang, L. Wang, S.C. Smith, G.Q.M. Lu, H.M. Cheng, Journal of Materials Chemistry 19 (2009) 2822–2829.
[335] W. Su, Y. Zhang, Z. Li, L. Wu, X. Wang, J. Lil, X. Fu, Langmuir 24 (2008) 3422–3428.
[336] S. Tojo, T. Tachikawa, M. Fujitsuka, T. Majima, Journal of Physical Chemistry C 112 (2008) 14948–14954.
[337] V. Stengl, T.M. Grygar, International Journal of Photoenergy (2012), Article ID 685935.
[338] S. Bagawasi, B. Tian, F. Chen, J. Zhang, Applied Surface Science 258 (2012) 3927–3935.
[339] Z. He, L. Xie, S. Song, C. Wang, J. Tu, F. Hong, Q. Liu, J. Chen, X. Xu, Journal of Molecular Catalysis A: Chemical 319 (2010) 78–84.
[340] Z. He, X. Xu, S. Song, L. Xie, J. Tu, J. Chen, B. Yan, Journal of Physical Chemistry C 112 (2008) 16431–16437.
[341] S. Song, C. Wang, F. Hong, Z. He, Q. Cai, J. Chen, Applied Surface Science 257 (2011) 3427–3432.
[342] T. Okajima, T. Yamamoto, M. Kunisu, S. Yoshioka, I. Tanaka, N. Umesaki, Japanese Journal of Applied Physics 45 (2006) 7028–7031.
[343] V. Lliev, D. Tomova, R. Todorovska, D. Oliver, L. Petrov, D. Todorovsky, M.U. Bujnova, Applied Catalysis A: General 313 (2006) 115–121.
[344] S. Song, F. Hong, Z. He, H. Wang, X. Xu, J. Chen, Applied Surface Science 257 (2011) 10101–10108.
[345] Z. He, L. Xie, J. Tu, S. Song, W. Liu, Z. Liu, J. Fan, Q. Liu, J. Chen, Journal of Physical Chemistry C 114 (2010) 526–532.
[346] D. Wang, X. Li, J. Chen, X. Tao, Industrial & Engineering Chemistry Research 51 (2012) 218–224.
[347] W.Y. Gan, H.J. Zhao, R. Amal, Applied Catalysis A: General 354 (2009) 8–16.
[348] G.S. Wu, J.P. Wang, D.F. Thomas, A.C. Chen, Langmuir 24 (2008) 3503–3509.
[349] P. Xu, J. Lu, T. Xu, S. Gao, B. Haung, Y. Dai, Journal of Physical Chemistry C 114 (2010) 9510–9517.
[350] J. Ding, Y. Yaun, J. Xu, J. Deng, J. Guo, Journal of Biomedical Nanotechnology 5 (2009) 1–7.
[351] Y. Su, X.W. Zhang, S. Han, X. Chen, L. Lie, Electrochemistry Communications 9 (2007) 2291–2298.